

The first Ka-band (26.1–35 GHz) blind line survey towards Orion KL

XUNCHUAN LIU (刘训川),^{1,*} TIE LIU,^{1,†} ZHIQIANG SHEN,^{1,‡} SHENG-LI QIN,² QIUYI LUO,¹ YAN GONG,³ YU CHENG,⁴ CHRISTIAN HENKEL,³ QILAO GU,¹ FENGYAO ZHU,⁵ TIANWEI ZHANG,⁶ RONGBING ZHAO,¹ YAJUN WU,¹ BIN LI,¹ JUAN LI,¹ ZHANG ZHAO,¹ JINQING WANG,¹ WEIYE ZHONG,¹ QINGHUI LIU,¹ BO XIA,¹ LI FU,¹ ZHEN YAN,¹ CHAO ZHANG,¹ LINGLING WANG,¹ QIAN YE,¹ AIYUAN YANG,⁷ FENGWEI XU,⁸ CHAO ZHANG,⁹ SOMNATH DUTTA,¹⁰ SHANGHUO LI,¹¹ MEIZHU LIU,² DONGTING YANG,² CHUANSHOU LI,² AND LI CHEN²

¹Shanghai Astronomical Observatory, Chinese Academy of Sciences, Shanghai 200030, PR China

²School of Physics and Astronomy, Yunnan University, Kunming, 650091, PR China

³Max-Planck-Institut für Radioastronomie, Auf dem Hügel 69, 53125 Bonn, Germany

⁴National Astronomical Observatory of Japan, 2-21-1 Osawa, Mitaka, Tokyo, 181-8588, Japan

⁵Center for Intelligent Computing Platforms, Zhejiang Laboratory, Hangzhou, 311100, PR China

⁶I. Physikalisches Institut, Universität zu Köln, Zülpicher Straße 77, 50937 Köln, Germany

⁷National Astronomical Observatories, Chinese Academy of Sciences, Beijing 100101, PR China

⁸Kavli Institute for Astronomy and Astrophysics, Peking University, 5 Yiheyuan Road, Haidian District, Beijing 100871, PR China

⁹Institute of Astronomy and Astrophysics, School of Mathematics and Physics, Anqing Normal University, Anqing, PR China

¹⁰Institute of Astronomy and Astrophysics, Academia Sinica, Roosevelt Road, Taipei 10617, Taiwan (R.O.C)

¹¹Max Planck Institute for Astronomy, Königstuhl 17, D-69117 Heidelberg, Germany

ABSTRACT

We conducted a Ka-band (26.1–35 GHz) line survey towards Orion KL using the TianMa 65-m Radio Telescope (TMRT). It is the first blind line survey in the Ka band, and achieves a sensitivity of mK level (1–3 mK at a spectral resolution of $\sim 1 \text{ km s}^{-1}$). In total, 592 Gaussian features are extracted. Among them, 257 radio recombination lines (RRLs) are identified. The maximum Δn of RRLs of H, He and C are 20, 15, and 5, respectively. Through stacking, we have detected the β lines of ion RRLs (RRLs of C⁺ with possible contribution of other ions like O⁺) for the first time, and tentative signal of the γ lines of ion RRLs can also be seen on the stacked spectrum. Besides, 318 other line features were assigned to 37 molecular species, and ten of these species were not detected in the Q-band survey of TMRT. The vibrationally excited states of nine species were also detected. Emission of most species can be modeled under LTE. A number of transitions of E-CH₃OH ($J_2 - J_1$) display maser effects, which are confirmed by our modeling, and besides the bumping peak at $J \sim 6$ there is another peak at $J \sim 13$. Methylcyanoacetylene (CH₃C₃N) is detected in Orion KL for the first time. This work emphasizes that the Ka band, which was long-ignored for spectral line surveys, is very useful for surveying RRLs and molecular lines simultaneously.

Keywords: ISM: abundances; ISM: molecules; line: identification; stars: formation

1. INTRODUCTION

The low-frequency (<50 GHz) line surveys have advantages in searching for complex organic molecules (COMs) and radio recombination lines (RRLs), because low-frequency lines tend to be non-seriously blended and more easily excited compared with those in higher frequency ranges. In contrast to the ample surveys at the high-frequency millimeter and submillimeter bands ($\nu > 70 \text{ GHz}$; e.g., Johansson et al. 1984; Turner 1989; Schilke et al. 1997; Schilke

et al. 2001; White et al. 2003; Tercero et al. 2010), there are only a scarcity of line surveys at low-frequency bands towards Orion KL (e.g. Corby et al. 2015; Gong et al. 2015; Rizzo et al. 2017), which is the nearest ($\sim 414 \text{ pc}$; Menten et al. 2007) high-mass star forming region and one of the most representative objects of line surveys. The emission of Orion KL is complex (e.g., Tercero et al. 2010), with contributions from several physical components including the foreground HII region M42 (Wilson et al. 1997), the PDR between M42 and the molecular cloud (e.g., Natta et al. 1994), the externally heated “compact ridge” (e.g., Mangum & Wootten 1993; Wang et al. 2011; Tahani et al. 2016), the hot cores (e.g., Mangum & Wootten 1993; Jacob et al. 2021), the extended ridge and plateau (e.g., Genzel & Stutzki 1989;

* liuxunchuan@shao.ac.cn

† liutie@shao.ac.cn

‡ zshen@shao.ac.cn

Table 1. The line surveys of Orion KL in low frequency range ($\nu < 50$ GHz).

Frequency coverage ⁽¹⁾	Telescope	Spectral resolution	Sensitivity ⁽²⁾	Reference ⁽⁴⁾
17.9–26.2 GHz	Effelsberg 100 m	61 kHz (~ 0.7 km s $^{-1}$)	5–22 mK	Gong et al. (2015)
26.1–35 GHz	TMRT 65 m	92 kHz (~ 0.9 km s $^{-1}$)	1–3 mK	This work
34.8–50 GHz	TMRT 65 m	92 kHz (~ 0.65 km s $^{-1}$)	1.5–5 mK ⁽³⁾	Liu et al. (2022)
41.5–50 GHz	DSS-54 34 m	180 kHz (~ 1.2 km s $^{-1}$)	8–12 mK	Rizzo et al. (2017)

⁽¹⁾ Only wide-band blind line surveys are listed here.

⁽²⁾ The line sensitivity in T_{MB} scale at the corresponding spectral resolution.

⁽³⁾ The line sensitivity at 49–50 GHz is slightly worse with a value of 5–8 mK.

⁽⁴⁾ Little can be known about the line survey of Ohishi et al. (1986) from its relevant published work. From the spectra of all of its covered frequency bands (34.25–50, 83.5–84.5, and 86–91.5 GHz), Ohishi et al. (1986) detected 19 molecular species, much smaller than the values of 39 and 53 detected in Q band alone by Rizzo et al. (2017) and Liu et al. (2022).

Bernal et al. 2021) as well as some other millimeter continuum sources (e.g., Wu et al. 2014). It makes Orion KL rich in spectral lines at different frequency bands (e.g., Blake et al. 1987; Schilke et al. 1997; Tercero et al. 2010; Crockett et al. 2014; Rizzo et al. 2017). This motivated us to conduct a multi-band low-frequency line survey using the Tianma 65-m Radio Telescope (TMRT) towards Orion KL (referred as the TMRT line survey below), aiming to obtain an unprecedented sensitive template for low-frequency spectra (with a line sensitivity of one or several mK), covering the whole working frequency range (1–50 GHz) of the TMRT.

The ongoing TMRT line survey began with the Q-band (35–50 GHz) pioneer survey (Liu et al. 2022), which is so far the most sensitive one compared with previous wide-band Q-band surveys of Orion KL (Ohishi et al. 1986; Rizzo et al. 2017). It reached a sensitivity at a level of 1.5–5 mK (Table 1) and 597 Gaussian features were extracted, proving the capability for the TMRT of conducting deep line surveys. In the Q band, the number of detected molecular lines, 395, is more than twice the number of RRLs, 153. Most of the Q-band molecular lines are emission of complex organic molecules (COMs). In contrast, the K-band (18–26 GHz) spectrum of Orion KL was found to be dominated by RRLs, as revealed by the survey of Gong et al. (2015) that have identified 164 RRLs among the 261 detected lines. It is reasonable to expect that the Ka-band (26–35 GHz) spectrum of Orion KL would have comparable numbers of RRLs and molecular lines, making the Ka band very suitable for observing COMs and RRLs simultaneously.

Despite its promising potential uses, the Ka band was long-ignored for spectral line surveys, and acted as a frequency gap especially for single-dish observations. This frequency range is usually preferred for satellite communication (e.g., Vanelli-Coralli et al. 2015), and was historically avoided for radio astronomy. It makes the Ka band a missing piece for previous line surveys (Table 1). To fill in this blank gap, we conducted a Ka-band (26–35 GHz) survey of Orion KL as a part of the TMRT line survey, following the Q-band one (Liu et al. 2022). Through long-time integrations, a line sensitiv-

ity of 1–3 mK was achieved with a frequency resolution of 91.553 kHz. This is the first blind line survey in the Ka band reaching a line sensitivity of mK level.

In Liu et al. (2023), we have reported the successful detection of the ion RRLs (X^+ RRLs with X^+ referred to C and/or O) in the interstellar medium for the first time, through combining the data of the TMRT surveys in three bands (Ka, Ku, and Q). This Ka-band survey is the most sensitive one, compared with the less sensitive Q-band survey and the partly executed Ku-band survey. It expanded the scope of our understanding of ion RRLs, because prior to that work, only two blended lines (105α and 121α) of He II in planetary nebulae had been reported (Chaisson & Malkan 1976; Terzian 1980; Vallee et al. 1990).

In this work, we present the overall results of the Ka-band (26.1–35 GHz) line survey of Orion KL. The paper is structured as follows: In Section 2 we introduce the observations. In Section 3 we describe the procedures of data reduction, line identification and emission modeling of RRLs and molecular lines. In Sections 4 and 5, we present more detailed results about the RRLs and molecular lines, respectively. We provide a summary in Section 6.

2. OBSERVATIONS

2.1. Ka-band receiving system of TMRT

The observations were carried out using the TMRT, built and operated by the Shanghai Astronomical Observatory¹. The TMRT is located in the western suburb of Shanghai, China. It has an aperture diameter of 65 m, corresponding to a full-width at half-maximum (FWHM) of the primary beam of $\sim 46''$ – $34''$ at 26–35 GHz. Its Ka receiver is a two-beam dual-polarization (LCP and RCP) cryogenic receiver, covering 26–40 GHz, with the 35–40 GHz overlapping with the working frequency range of the Q-band receiver. The beam 2 was employed for our single-pointing observations. The receiver noise temperatures were 10–30 K, and the system temperatures (T_{sys}) ranged from 60 K to 150 K, depending

¹ <http://english.shao.cas.cn/sbysys/>

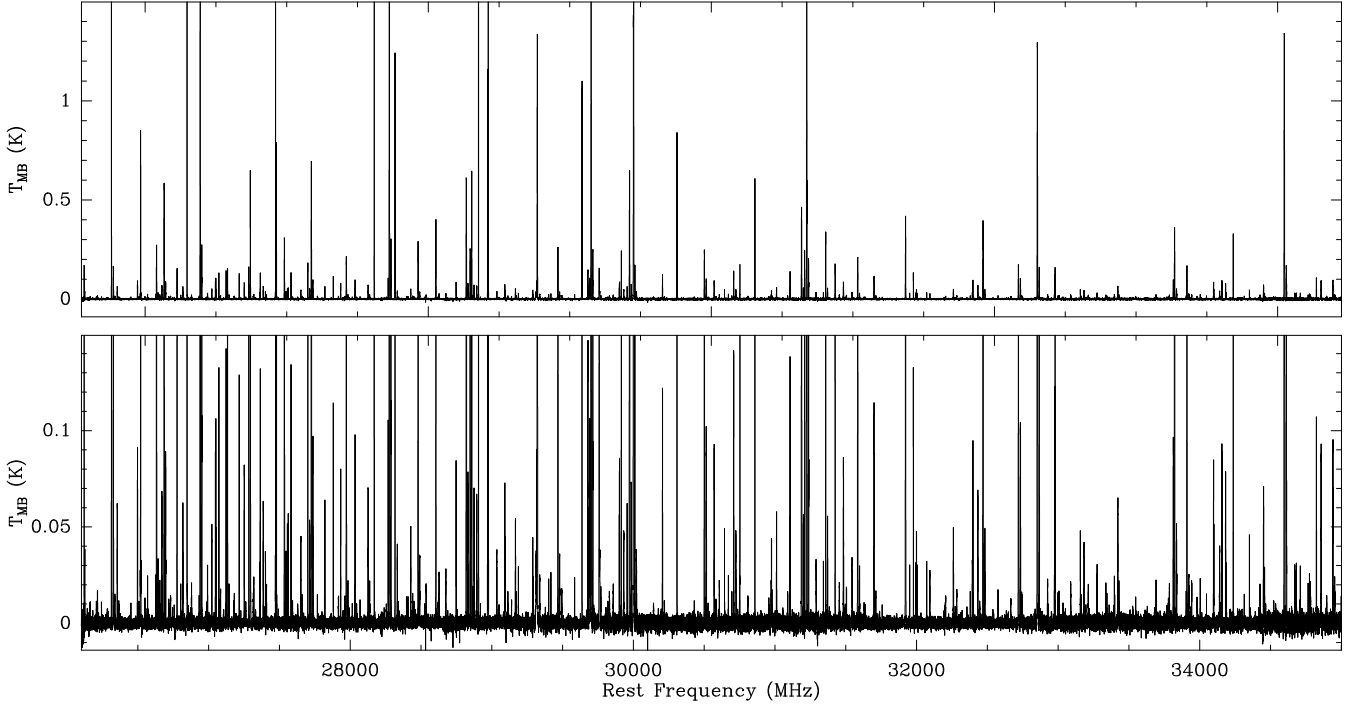


Figure 1. The overview of the Ka-band (26.1–35 GHz) spectrum of Orion KL observed by the TMRT. Lower panel: A zoomed-in view of the same spectrum. (The data used to create this figure are available online.)

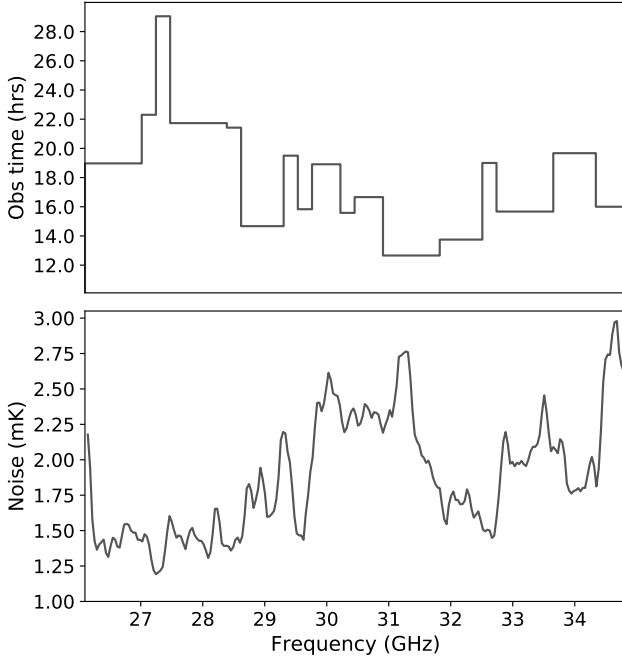


Figure 2. The observation time (upper) and rms noise (lower) of the Ka-band spectrum. Both the on-source and off-source integration time have been included to calculate the observation time.

on the frequency, elevation and especially the weather conditions (Wang et al. 2017b).

During the preparation for this survey, the Ka-band pointing model of the TMRT was updated through tracking strong

continuum sources, including DR21 and 3C84, for one whole day, following the method of Wang et al. (2017a). The pointing accuracy was better than 5 arcsec. The aperture efficiency is nearly constant (0.5 ± 0.1) thanks to the active surface control utilizing actuators which can compensate for the gravity deformation of the main reflector during observations (Dong et al. 2018). For calibration, the signal of noise diodes was injected lasting for one second within each two-second period. In summer, the high water vapour content and deformation by sunlight make TMRT difficult to be used for Ka/Q-band observations. Under typical weather conditions at the TMRT in the winter semester, the zenith atmospheric opacities were 0.1 in the Ka band (Wang et al. 2017b). Calibration uncertainties were estimated to be within 20%.

2.2. The Ka-band survey

This Ka-band line survey of Orion KL covered 26.1–35 GHz. Although the working frequency range of the K-band receiver is 26–40 GHz, the 35–40 GHz was not covered by this survey, because it has been done by our previous Q-band line survey (Liu et al. 2022). The 26–26.1 GHz was not covered because of the limitation of the bandpass filter. The digital backend system (DIBAS) of TMRT is an FPGA-based spectrometer based on the design of the Versatile GBT Astronomical Spectrometer (Bussa & VEGAS Development Team 2012), and it provides 29 observing modes. The setup of the backend for the Ka-band survey is the same as that of the Q-band survey (Liu et al. 2022). Two banks (the third one is not available at present) have a bandwidth of 1.5 GHz each,

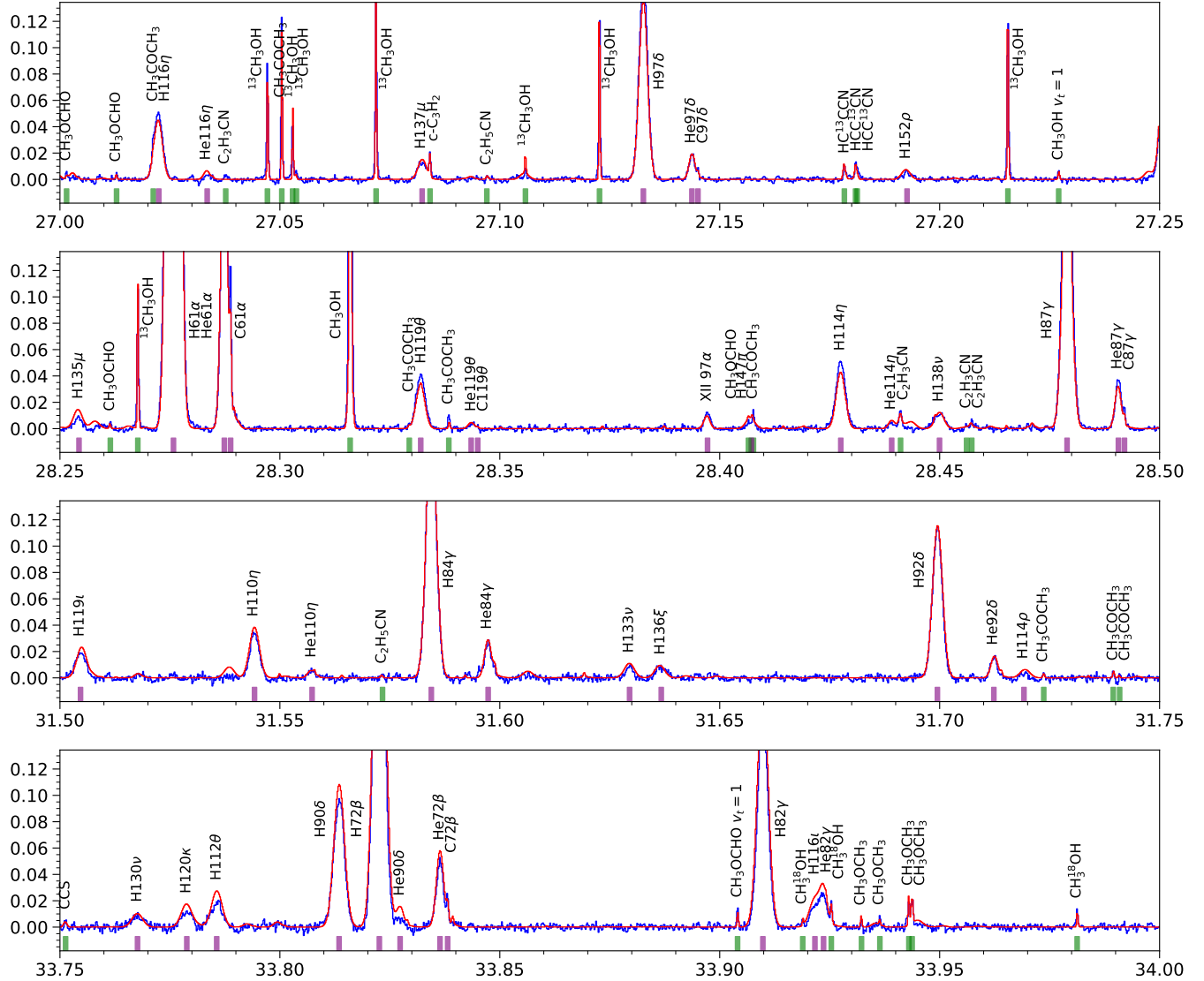


Figure 3. The images of Ka-band spectrum of Orion KL. The x-axis is rest frequency in units of gigahertz (with a Doppler correction applied adopting a V_{LSR} of 6 km s^{-1}). The y-axis is T_{MB} in units of kelvin. The blue line is the Orion KL spectrum observed by the TMRT 65 m, which has been smoothed to have a frequency resolution of 183 kHz ($\sim 1.8 \text{ km s}^{-1}$ at 30 GHz). The red line represents the modeling fitting. The purple strips denote the detected RRLs. The green strips denote the molecular lines. The gray strips mark the U lines. See Figure 16 for all the spectral images.

and they work independently with no limitation on the separation between their central frequencies. Under the mode 2 of DIBAS, each polarization of each bank has 16384 channels, and the channel width is 91.553 kHz, corresponding to a velocity resolution (δV) of $\sim 0.92 \text{ km s}^{-1}$ at 30 GHz.

The observations were conducted from September 28th to October 30th, 2022. The targeting position is RA(J2000)=05:35:14.55, DEC(J2000)=−05:22:31.0. Different physical components of Orion KL (see Section 1) can be covered by a single beam of the TMRT, as depicted in our previous Q-band survey (Liu et al. 2022). Position-switching observation mode was adopted, with the off points 15' away (in azimuth direction) from the target. The offset value is

much larger than 4', the angular size of the brightest region of M42 (Yusef-Zadeh 1990; Wilson et al. 1997). We periodically integrated two minutes in each position (on/off). During observations of this survey, pointing was checked every two hours.

For each frequency bank, its frequency coverage in the sky frequency scale was fixed. The frequency of the local oscillator (LO) did not change during the observation for a single frequency setup. The spectrum of each on-off repeat was corrected from the topocentric frame to the frame of the local standard of rest (LSR) during data processing. The frequencies of the two banks were shifted in different setups to cover 26.1–35 GHz. For most frequency ranges of Ka band, there is

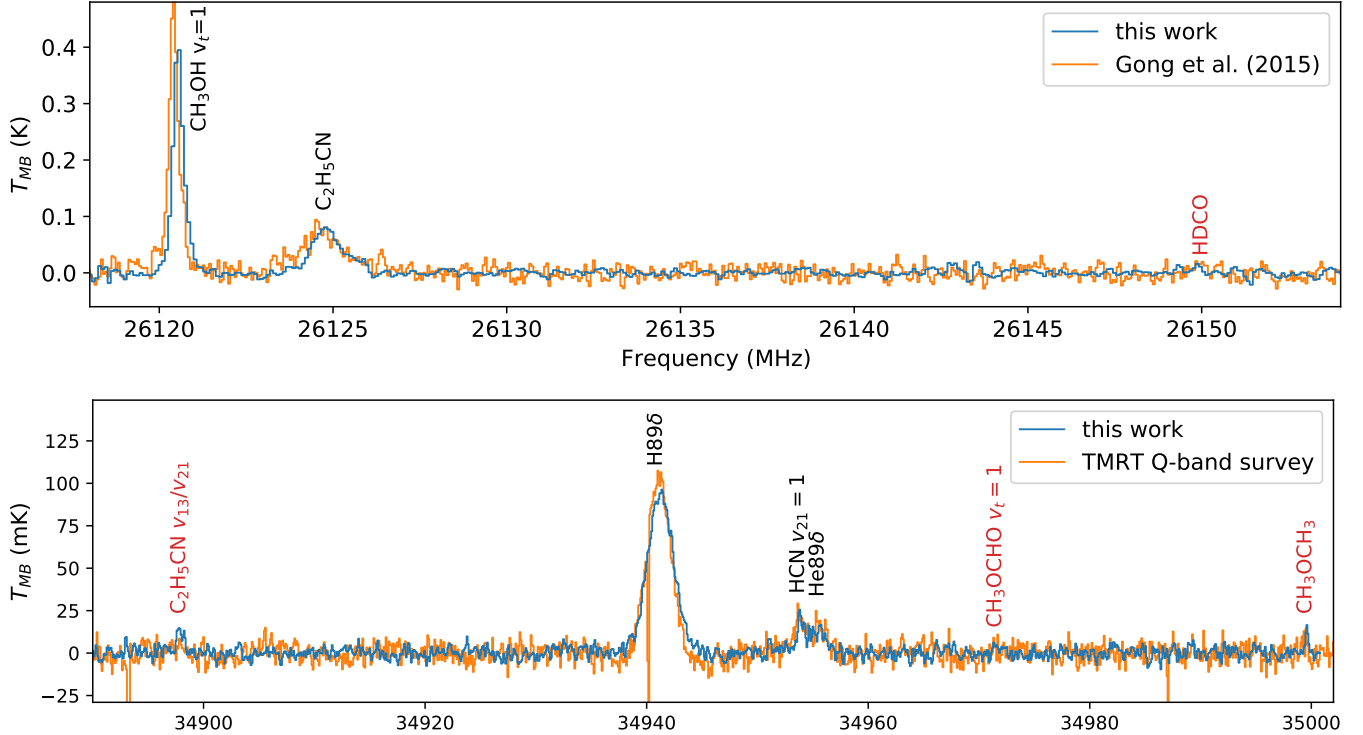


Figure 4. Upper: Comparison between the spectra of this Ka-band (26.1–35 GHz) survey and of the K-band (17.9–26.2 GHz) survey of Effelsberg 100 m by Gong et al. (2015). See Section 3.1 for possible reasons of the slight velocity discrepancy (by about two channels) between the two surveys. Lower: Comparison between the spectra of this Ka-band survey and the TMRT Q-band (34.8–50 GHz) survey (Liu et al. 2022). The overlapping frequency ranges of those surveys are located at the edges of the frequency coverages, and consequently have relatively poor sensitivities. Note that the lower panel has wider frequency range than that of the upper panel.

no noticeable radio frequency interference (RFI) on the spectrum. At some narrow frequency ranges (e.g., $\sim 26.4 - 26.8$ GHz), RFI can be sometimes very strong but it does not last for a long time. Each frequency point was covered by at least two different frequency setups observed on different days. The spectra with obvious RFI were manually dropped. Each of the observed frequency points is covered by a telescope time of 12–25 hours, depending on the weather conditions.

3. OBSERVATIONAL RESULTS

3.1. Data reduction

The spectra of each polarization of each frequency were first averaged weighted by $1/T_{\text{sys}}^2$. The averaged spectrum was then chopped into segments of 100 MHz. For each segment, we manually fit the spectral baseline and get the noise of each segment using the procedure provided by Gildas/CLASS (Guilloteau & Lucas 2000). To conduct this procedure, the frequency intervals that contain visible line features or spectral emission predicted from the Q-band data (Liu et al. 2022) have been masked out. We further converted the frequency of the spectrum from the LSR frame to the rest frame of Orion KL assuming a systematic velocity of Orion KL (V_{LSR}) of 6 km s^{-1} . Finally, we spliced together all the segments weighted by their noise levels to obtain the final

Ka-band spectrum, covering 26.1–35 GHz with a frequency resolution of 91 kHz.

The final spectrum (in T_{MB} scale) is shown in Figure 1. To estimate the rms noise of the spectrum, we first masked out all the extracted emission features and bad channels (Sect. 3.2), and then for each channel we calculated the standard deviation of the intensities of its unmasked neighbour channels within 25 MHz. As expected, the rms noise is roughly inversely proportional to the integration time. The 26.1–26.2 GHz is close to the edge of the working frequency of the TMRT in the Ka band, and can not be placed in the inner region of a frequency bank which has better performance. Thus, the noise level of 26.1–26.2 GHz is slightly higher (Figure 2). The rms noise of the final spectrum ranges from 1 mK to 3 mK, with a mean value of 1.87 mK and a median value of 1.80 mK.

Figure 3 shows examples of the zoom-in Ka-band spectrum. The lower end of the Ka-band spectrum (26.1–26.16 GHz) was also covered by the K-band survey of the Effelsberg 100 m telescope (Gong et al. 2015). The upper end of the Ka-band spectrum (34.88–50 GHz) was also covered by the Q-band survey of the TMRT (Liu et al. 2022). Figure 4 compares the overlapped spectra of the three surveys. Note that the transition of CH_3OH at ~ 26120 MHz on the K-band

Table 2. The number of RRLs and molecular lines detected by different surveys⁽¹⁾.

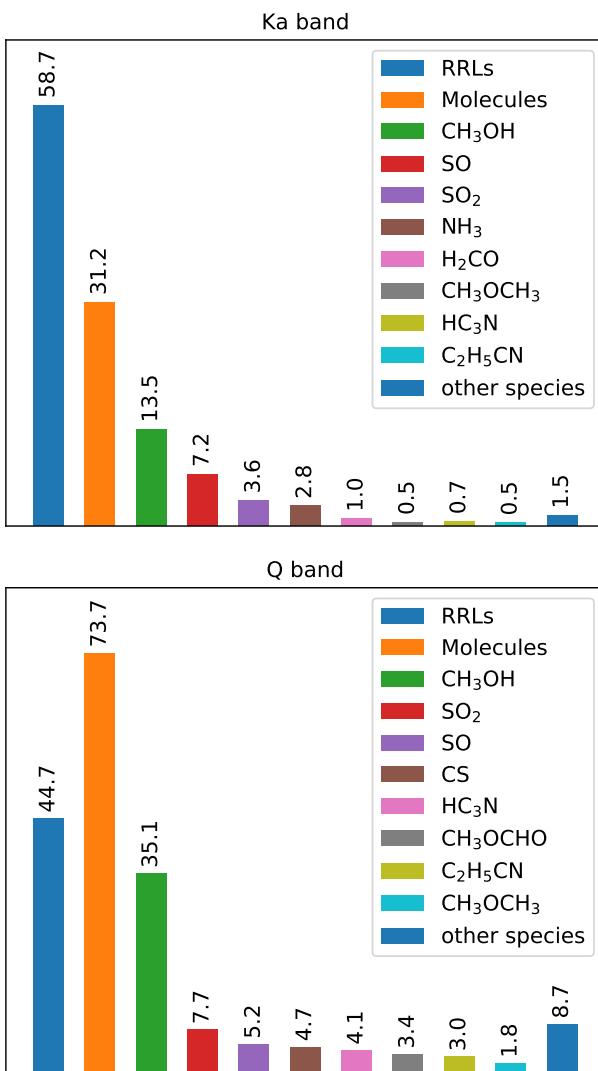
Ref.	N_l	ρ_l	$N_{\text{RRL}}^{(2)}$	$N_{\text{mol}}^{(3)}$	$N_{\text{RRL}}^{\text{mol}}$	N_U	$N_{\text{RRL}}/N_{\text{mol}}^{(4)}$
This work	592	64	257(12)	318(20)	7	10	0.9
Liu et al. (2022)	596	36	153(13)	395(50)	9	39	0.6
Rizzo et al. (2017)	227	26	66	143	—	18	0.5
Gong et al. (2015)	261	32	164	97	—	—	1.7

⁽¹⁾ N_l is the total number of detected line features. ρ_l is the averaged number of detected line features per GHz. N_{RRL} is the number of RRLs, including those blended with other RRLs. N_{mol} is the number of molecular lines, including those blended with other molecular lines. $N_{\text{RRL}}^{\text{mol}}$ is the number of line features blended by both RRLs and molecular emission. N_U is the number of U lines.

⁽²⁾ The values in the brackets represent the number of line features blended by more than one RRL but no molecular transition.

⁽³⁾ The values in the brackets represent the number of repeated molecular line features because of multiple velocity components.

⁽⁴⁾ The ratio between the number of detected transitions of RRLs and molecular transitions.

**Figure 5.** The total Ka-band (upper) and Q-band (lower) emission flux (in units of K MHz) of detected species.

spectrum is slightly redder (by two channels) than that on the Ka-band spectrum. This may be caused by the slightly different targeting centers of the two surveys. The target of the

K-band survey is located at 16'' south-west of the target of this survey, which is smaller than the beam sizes of both the TMRT and the Effelsberg 100 m. The intersection between the fields of view of the two surveys covers more than half the primary beam of the TMRT (see Figure 1 of Liu et al. (2022)). We modeled the K-band spectral emission based on the Ka band spectra, and compared the observed and modeled spectra of RRLs and CH₃OH in the K band. The K-band spectra around 26 GHz are all redshifted by about two channels compared with the model. However, this is not a systematical trend in the whole K band since in some frequency ranges the velocities match each other. The velocities of the Q-band spectra of RRLs and CH₃OH by Liu et al. (2022) and Rizzo et al. (2017) were consistent with each other, as highlighted by the Figure 5 of Liu et al. (2022). The velocities of the Ka-band RRLs are self-consistent and are consistent with the modeled spectrum derived based on Q-band emission parameters (Liu et al. 2022). Therefore there is no systematical frequency bias in the Ka-band survey. The small velocity discrepancy between this survey and the K-band survey (Gong et al. 2015) has no influence on the comparison between the two surveys.

Among the three surveys, the Ka-band survey has the best sensitivity (Table 1), and can detect emission lines that have not been detected by the previous Q-band and K-band surveys, although the overlapped frequency ranges are very narrow. The main-beam temperatures of spectral lines from extended regions (e.g., RRLs) measured by different surveys should be consistent with each other. The aperture of Effelsberg is larger than that of the TMRT. Thus, for spectral lines originate from more compact regions, e.g., the transition of CH₃OH $v_t = 1$ at 26120.6 MHz, their main-beam temperatures measured by the TMRT are slightly lower than that by the Effelsberg as expected due to potentially smaller filling factors (see the upper panel of Figure 4).

3.2. Line identification

We visually searched for line features on the Ka-band spectrum. Then, Gaussian fittings were manually conducted to those possible line features one by one using the fitting pro-

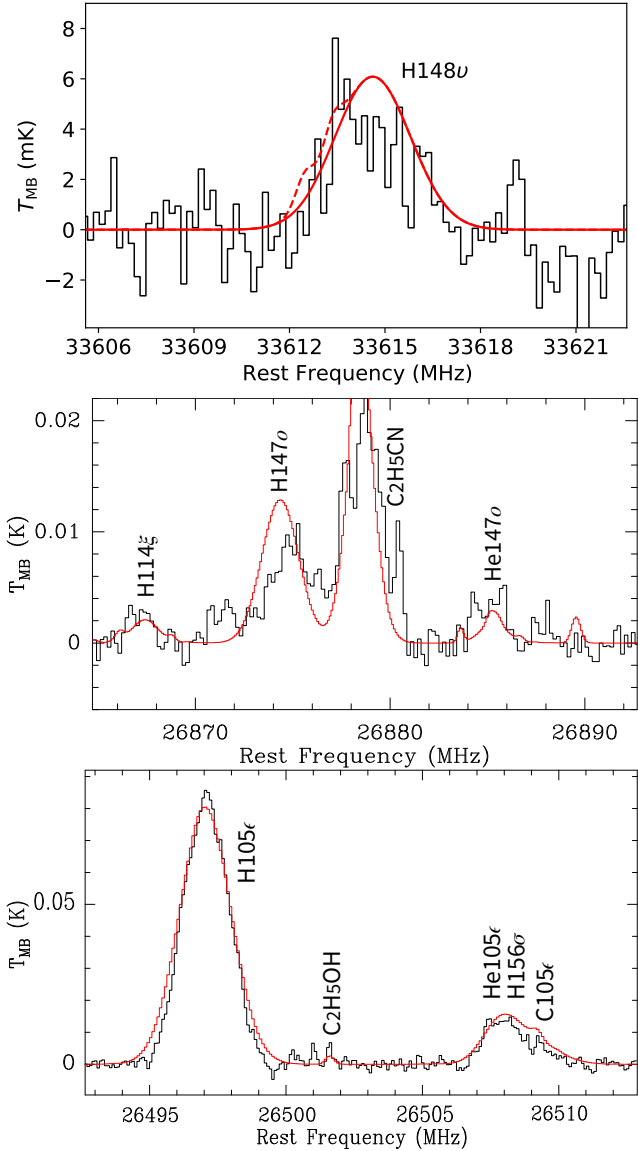


Figure 6. Example of the detected RRLs with large Δn . The red lines represent the result of model fitting of RRLs and molecular lines. The dashed line in the upper panel has taken into account the emission of $\text{C}_2\text{H}_5\text{CN } v_{13}/v_{21}$.

cedure provided by the GILDAS/CLASS. For blended lines or strong lines with obvious non-Gaussian shapes, multiple Gaussian fittings were applied. In total, 592 Gaussian components (referred to line features) were extracted (Tables 2, 6, and 7).

Then, we modeled the Ka-band spectrum based on the physical parameters fitted from the Q-band observations following Liu et al. (2022). Most of the Ka-band line features can be reproduced by the physical parameters of species detected in the Q band. We first coarsely crossmatched those line features with RRLs of H, He and C, and the transitions of molecules detected in the Q-band survey. Further, we tried

to assign the unmatched lines to species undetected in the Q-band survey. A species was marked as detected when more than one of its transitions were detected above 3σ and can be reproduced by the emission model with parameters compatible with values in the literatures (e.g., Tercero et al. 2011; Gong et al. 2015; Rizzo et al. 2017; Liu et al. 2023). The species with only one line feature in the Ka band is also marked as detected if it is detected in the Q band. For vibrationally excited species, it would be marked as detected even if only one of its rotational lines is detected, as long as that transition is consistent with the model prediction based on the physical parameters of its corresponding ground-state species (e.g., E-CH₃OH $v_t = 1$ in Section 5.1). See Sections 4 and 5 for the details about the model fitting process of RRLs and molecular lines, respectively. We iterated the above procedures trying to properly assign as many as possible detected line features. Finally, the still unmatched line features are marked as unidentified lines (marked as ‘U’).

Table 6 lists the molecular lines and unidentified lines, including those blended with RRLs. Table 7 lists the RRLs which are not blended with any molecular emission.

3.3. Overview of the spectral lines

Although the bandwidth of this Ka-band line survey (~9 GHz) is narrower than that of the Q-band survey of the TMRT (15 GHz), the number of line features detected by the two surveys are comparable, partly because the Ka-band survey has a higher sensitivity and the weak line features can be detected (Table 1). The line density (ρ_l), defined as the averaged number of line features detected per GHz, of this survey is nearly twice the ρ_l of previous surveys in the K and Q bands (Table 2). The Q-band spectrum of Orion KL is dominated by molecular transitions (Rizzo et al. 2017; Liu et al. 2022), and the ratio between the numbers of RRLs and molecular transitions, 0.5, is weakly dependent on the sensitivity (Table 2). In contrast, the K-band spectrum is dominated by RRLs (Gong et al. 2015). Among the 592 line features of this survey, the number of transitions of RRLs, 263, and molecular transitions, 305, are comparable with each other. The total emission flux contributed by RRLs, 58.7 K MHz, is also comparable with that by molecular transitions, 35.2 K MHz (Figure 5). Thus, the Ka band, a long-ignored window for spectral line surveys located between the K band and Q band, is very useful for studying RRLs and molecular lines simultaneously.

The U lines are all weak ($T_{\text{peak}} < 10 \text{ mK}$) and some of them are narrow spikes (Table 6 and Figure 3). The Ka-band survey is deeper than the Q-band survey, and we have dropped the data of bad quality during the observations since there were usually several different frequency setups for each frequency range (Section 2.2). This is why the Ka-band survey

Table 3. The maximum Δn of RRLs detected in Orion KL.

Ref.	band	frequency	H	He	C	X ⁺
This work	Ka	26.1–35 GHz	20	15	5	2,3 ⁽¹⁾
Liu et al. (2022)	Q	35–50 GHz	16	7	3	–
Liu et al. (2023)	Ku/Ka/Q	12–18 GHz, 26.1–50 GHz	–	–	–	1
Rizzo et al. (2017)	Q	41.5–50 GHz	11	4	2	–
Gong et al. (2015)	K	17.9–26.2 GHz	11	4	1	–
Bell et al. (2011)	C	5.98–6.05 GHz	21,25 ⁽²⁾	6	–	–

⁽¹⁾ Through stacking (Section 4.3). The signal of the stacked γ ($\Delta n = 3$) is marginal, and the stacked β ($\Delta n = 2$) line is more reliable (Section 4.3).

⁽²⁾ An H RRL with Δn of 25 was reported but only has an intensity of 2σ . Note that the H RRL with $\Delta n = 21$ (H274 ϕ at 6013.5 MHz) detected by Bell et al. (2011) is close to He230 μ (6013.8 MHz). Although, under LTE, the intensity of He230 μ is only one fourth the value of H274 ϕ .

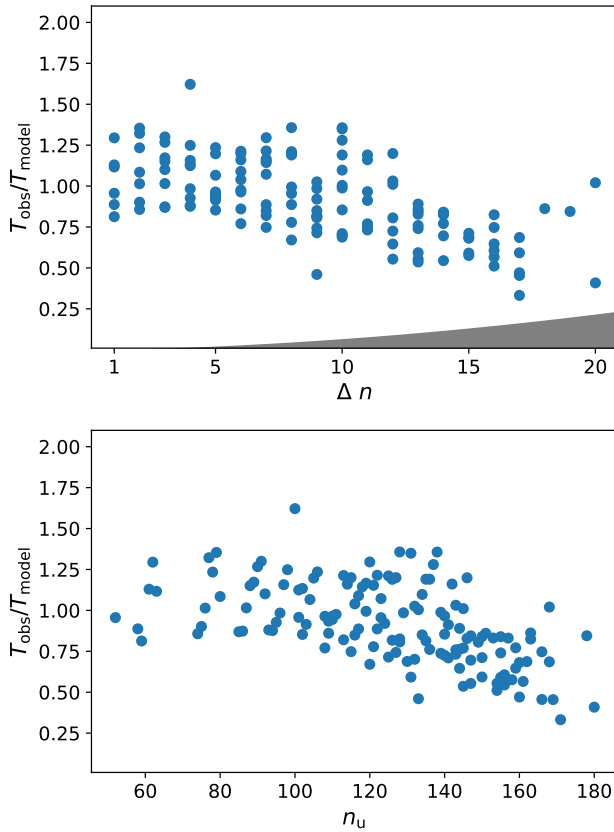


Figure 7. Upper: The correlation between Δn and the intensity ratio between observation and model ($T_{\text{obs}}/T_{\text{model}}$). The gray area represents the $1-\sigma$ uncertainty of $T_{\text{obs}}/T_{\text{model}}$. Only the uncertainty of spectral noise is considered here, and the uncertainty contributed by calibration is not taken into account. Lower: The correlation between upper-level principle quantum number (n_u) and $T_{\text{obs}}/T_{\text{model}}$. The two panels are only for H RRLs.

has much less spikes and bad channels than in the Q band (Table 2).

4. RRLS

The rest frequencies of RRLs can be calculated from the Rydberg formula (e.g., Towle et al. 1996; Gordon &

Sorochenko 2002)

$$\nu_{\text{rest}}^{\text{RRL}}(n + \Delta n, n) = \frac{m'_e}{m_e} R_\infty c Z^2 \left(\frac{1}{n^2} - \frac{1}{(n + \Delta n)^2} \right) \quad (1)$$

with

$$m'_e = \frac{M - Zm_e}{M - (Z - 1)m_e}. \quad (2)$$

Here, M and $Z - 1$ are the total mass and atomic charge of a hydrogenic emitter, respectively, m_e is the electron mass, m'_e is the reduced mass of the electron, and $R_\infty = 109737.31568 \text{ cm}^{-1}$ (Tiesinga et al. 2021). The value of n is large for RRLs and it is thus valid to treat the emitters as hydrogenic. For RRLs of neutral atoms recombined from singly ionized ions (X^+ or X II), Z should be adopted as one. For RRLs of singly ionized ions recombined from doubly ionized ions (X^{2+} or X III), Z should be adopted as two. In this work, the RRLs with $Z = 1$ and $Z > 1$ are referred as neutral RRLs and ion RRLs, respectively.

In total, 257 emission features in this survey are assigned to RRLs, including 245 unblended ones (Tables 2, 6, and 7). The RRLs contribute to 60 percent of the total emission flux of the spectral lines in Ka band (Figure 5). In Liu et al. (2023), we have reported the first detection of the α lines of RRLs of carbon and/or oxygen ions in the interstellar medium. In below sections, we would display all the RRLs detected in the Ka band towards Orion KL (Section 4.1), including the high-order neutral RRLs with the maximum value of Δn reaching 20 (Section 4.2), reported the first detection of ion RRLs with $\Delta n > 1$ (the β and γ lines) through stacking all the unblended transitions (Section 4.3).

4.1. LTE fitting and analysis

We followed the method of Liu et al. (2022) to reproduce the neutral RRLs ($Z = 1$) in the Ka band. Under the typical electron density of Orion KL ($n_e \sim 10^4 \text{ cm}^{-3}$; Gordon & Sorochenko 2002), the departure coefficients (b_n) are close to unity, corresponding to the case of local thermodynamic equilibrium (LTE). The emission measure (EM) of $X^{(n-1)+}$ is defined as $\int n_{X^{n+}} n_e dl$, and $n_{X^{n+}}$ and n_e are the volume densities of X^{n+} and free electron, respectively. For RRLs with

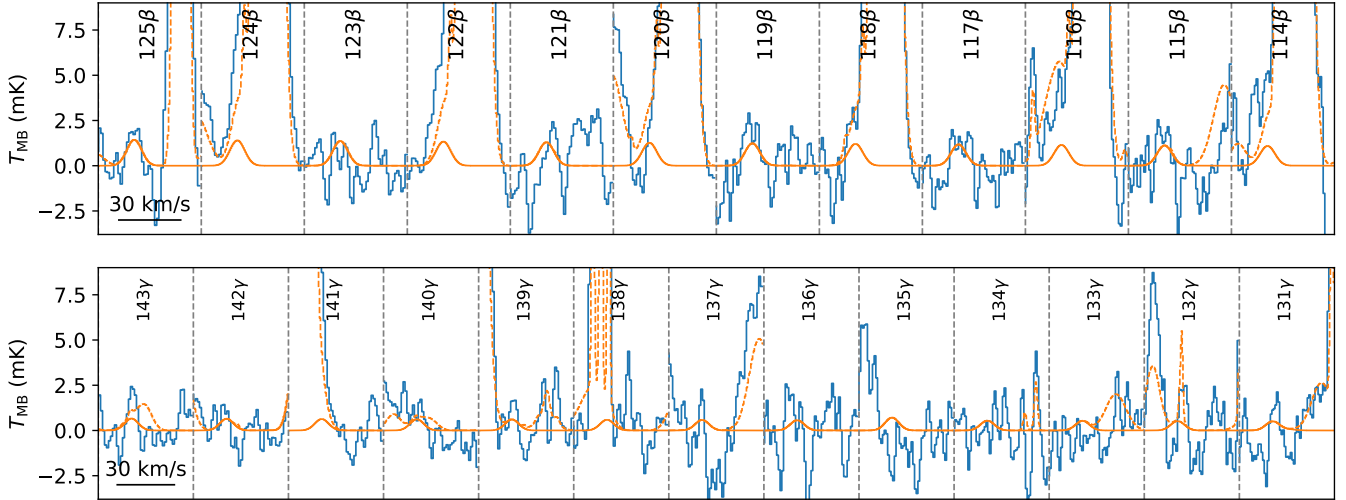


Figure 8. The Ka-band $X^+n\beta$ (upper panel) and X^+ny (lower panel) lines of ion RRLs (blue lines). The orange lines are the modeled spectrum. The orange dashed line takes emission of all species (molecular transitions and RRLs) into account, and the orange solid line only considers the ion RRLs. We note that, these $X^+n\beta$ and X^+ny RRLs were not detected individually, and some of them were at most marginally detected. See Figure 9 for the stacked spectra.

small $\Delta n = n_2 - n_1$, the absorption oscillator strengths (f_{n_1, n_2}) can be well approximated by the formula of Menzel (1968), as what we have adopted for the fitting of Q-band RRLs (Liu et al. 2022). However, in the Ka-band survey, RRLs with Δn as large as 20 were detected (Section 4.2). For such large Δn , the empirical values of f_{n_1, n_2} (Menzel 1968) can deviate from the precise values by more than 50 percent (Appendix A). Thus, in this work, we numerically tabulated the precise values of f_{n_1, n_2} (Appendix A), instead of adopting the values derived from the empirical formula of Menzel (1968). We note that the *EM* will not be changed under the two different set of f_{n_1, n_2} , since it mainly depends on the electron temperature and the intensities of strong lines with small Δn .

The electron temperature (T_e) can be estimated from the intensity ratios between RRLs and continuum (Gordon & Sorochenko 2002), but can not be constrained by RRLs alone. Unfortunately, the continuum intensity was not well calibrated during our observations, and we have to assume a T_e to derive the emission measure. For RRLs from H II regions (neutral RRLs of H and He and ion RRLs), the T_e was fixed to be 8000 K (Wilson & Rood 1994; Lerate et al. 2006). The *EM* of H was then derived to be $1.5 \times 10^6 \text{ cm}^{-6} \text{ pc}$, and the *EM* of He is one tenth the value of H. The neutral RRLs of C mainly originate from the PDRs. Assuming a T_e of 300 K, the Ka-band spectra of the neutral RRLs of C can be reproduced by adopting an emission measure (*EM*) of $1.8 \times 10^2 \text{ cm}^{-2} \text{ pc}$ (Figure 3). Table 2 of Liu et al. (2023) has already listed the fitted *EM*, velocity (V_{LSR}), and line widths (ΔV) of both neutral RRLs and ion RRLs basically based on this Ka-band survey of Orion KL, and thus will not be repeated in this work. In Liu et al. (2023), we briefly compared those parameters to justify the detection of ion RRLs of X^+

with X referred to be C and/or O. Below, we will quote those parameters for more detailed analysis.

Figure 7 shows the intensity ratios between the observation and the model fitting ($T_{\text{obs}}/T_{\text{model}}$) for different transitions of H RRLs. For $\Delta n < 10$, T_{obs} and T_{model} are consistent with each other within 50 percent, mainly contributed by the uncertainties of calibration and the different beam dilution at different frequencies. H96δ is an exception with a $T_{\text{obs}}/T_{\text{model}}$ of ~ 1.6 . For $\Delta n > 10$, the observed intensities tend to be lower than the model fitting. We do not know the specific reason for this discrepancy. One possibility is that the RRLs with large Δn (and thus relatively large n within a given frequency range) may deviate from LTE. Alternatively, RRLs with large Δn tend to be weak, and the procedure of reducing spectral baseline through polynomial fitting may suppress broad and weak line features (Section 3.1). Further observations with higher S/Ns would help to explore this issue.

4.2. High-order neutral RRLs

Among the RRLs detected towards Orion KL in this survey, H148ν has the maximum Δn of 20 (Figures 6 and 7). The line feature associated with H148ν has an intensity of larger than five sigma (Table 7), but it is slightly blended with two transitions of the vibrationally excited C₂H₅CN v_{13}/v_{21} (Figure 6). Through modeling the emission of RRLs (Section 4.1) and C₂H₅CN v_{13}/v_{21} (Section 5.2.2), we found that this line feature should be dominated by H148ν (Figure 6). For each $\Delta n < 20$, there are one or more H RRLs that have been detected by this survey with intensities consistent with the model prediction (Figure 6). Thus, the detection of H148ν should be reliable. The maximum Δn of this survey is the largest compared with previous blind line surveys at

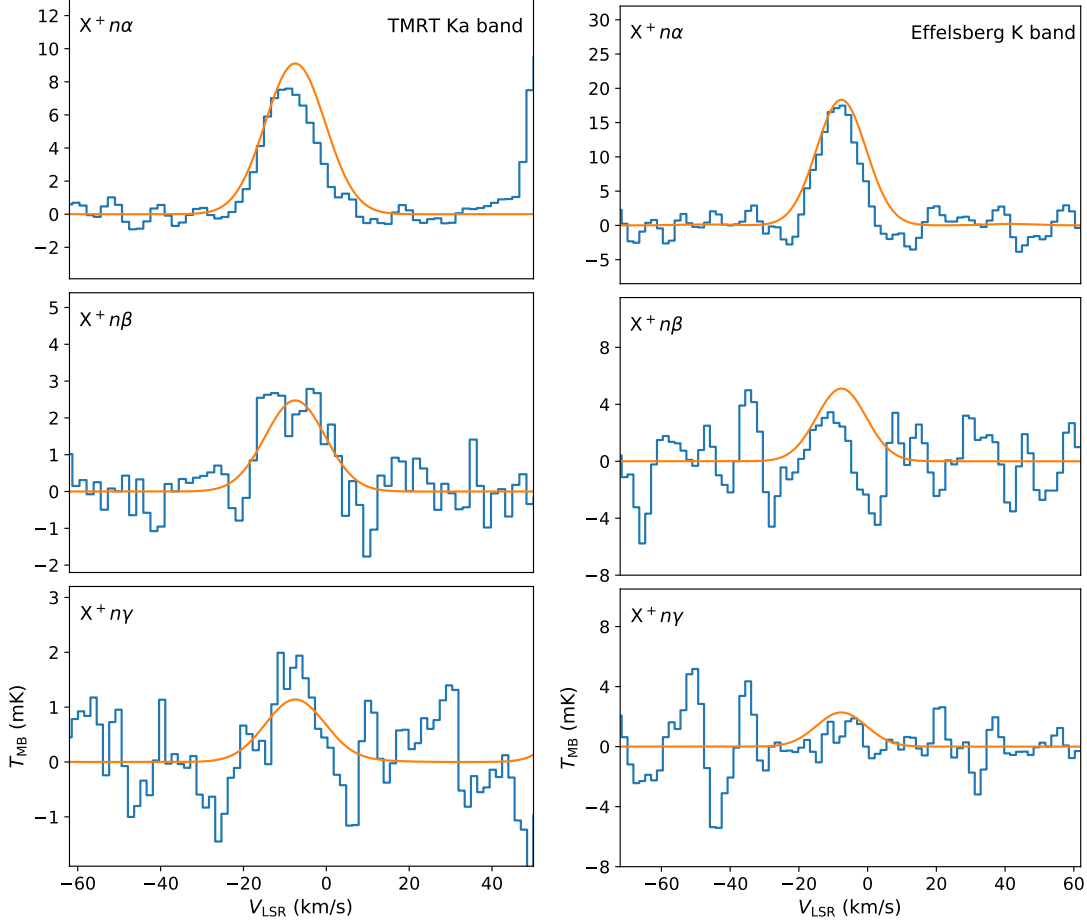


Figure 9. The blue lines are the α (top), β (middle) and γ (bottom) lines of ion RRLs stacked from the spectra of Orion KL measured in Ka band using the TMRT 65 m (left) and in K band using the Effelsberg 100 m by Gong et al. (2015) (right). The orange lines are the modeled spectra of ion RRLs. The orange lines in the right panels have been multiplied by a factor of 0.8. Only the unblended transitions are stacked. Specifically, in Ka band, we stacked $X^+ n\alpha$ ($n = 99, 97, 95, 92, 91$), $X^+ n\beta$ ($n = 123, 121, 119, 117, 115$) and $X^+ n\gamma$ ($n = 142, 137, 136, 134, 131$). In K band, we stacked $X^+ n\alpha$ ($n = 112, 111, 110, 108, 107, 106, 105, 104, 103, 101, 100$), $X^+ n\beta$ ($n = 141, 137, 135, 131, 127$) and $X^+ n\gamma$ ($n = 162, 159, 158, 156, 153, 148, 147, 146, 145, 144$).

frequency bands (Ku, K, and Q) close to this survey (Table 3). Bell et al. (2011) reported the detection of a 2σ signal H RRLs with $\Delta n = 25$ and a 3σ signal of H RRLs with $\Delta n = 21$ (H274 ϕ) from a narrow-band (5.98–6.05 GHz) survey towards Orion KL using the NRAO 140-foot (43 m) telescope. RRLs tend to be weaker in the Ka band than in the C band. The broad bandwidth and much higher angular resolution of this survey enable us to detect spectrally resolved RRLs with a maximum Δn close to that of Bell et al. (2011).

For He and C RRLs of this survey, the He147 α and C105 ϵ reach the maximum Δn of 15 and 5, respectively (Figure 6). Besides He147 α , He114 ξ (with $\Delta n = 14$ and $f_{\text{rest}} = 26866.5$ MHz) was also detected (Figure 3 and Table 7), and their intensities are consistent with those from LTE model. Thus, the line feature of He147 α is considered to be a firm detection under a 4σ significance level (Table 7). The maximum Δn of He and C RRLs of this survey are the largest compared with previous surveys towards Orion KL (Table 3).

4.3. High-order ion RRLs

Because of the blending with helium RRLs, the wide component ($\Delta V \sim 20 \text{ km s}^{-1}$) of carbon RRLs originating from the ionized regions are difficult to be detected. The narrow component ($\Delta V \sim 5 \text{ km s}^{-1}$; Table 2 of Liu et al. (2023)) of carbon RRLs can be spectrally resolved, but it traces the PDRs instead of the ionized regions. The PDRs traced by narrow C RRLs have a V_{LSR} of $\sim 8 \text{ km s}^{-1}$, which is more than 10 km s^{-1} redder than that of the ionized gas of M42 traced by H/He RRLs ($V_{\text{LSR}} \sim -4 \text{ km s}^{-1}$; Rizzo et al. 2017; Liu et al. 2023). The interaction between M42 and the molecular cloud may be responsible for the discrepancy of the V_{LSR} of PDRs located at the interface between them (Cuadrado et al. 2015; Rizzo et al. 2017). The ion RRLs provide us an opportunity to trace the doubly ionized element heavier than helium in the ionized regions. In Liu et al. (2023), only the α lines of RRLs of C $^+$ and/or O $^+$ were reported. There was no

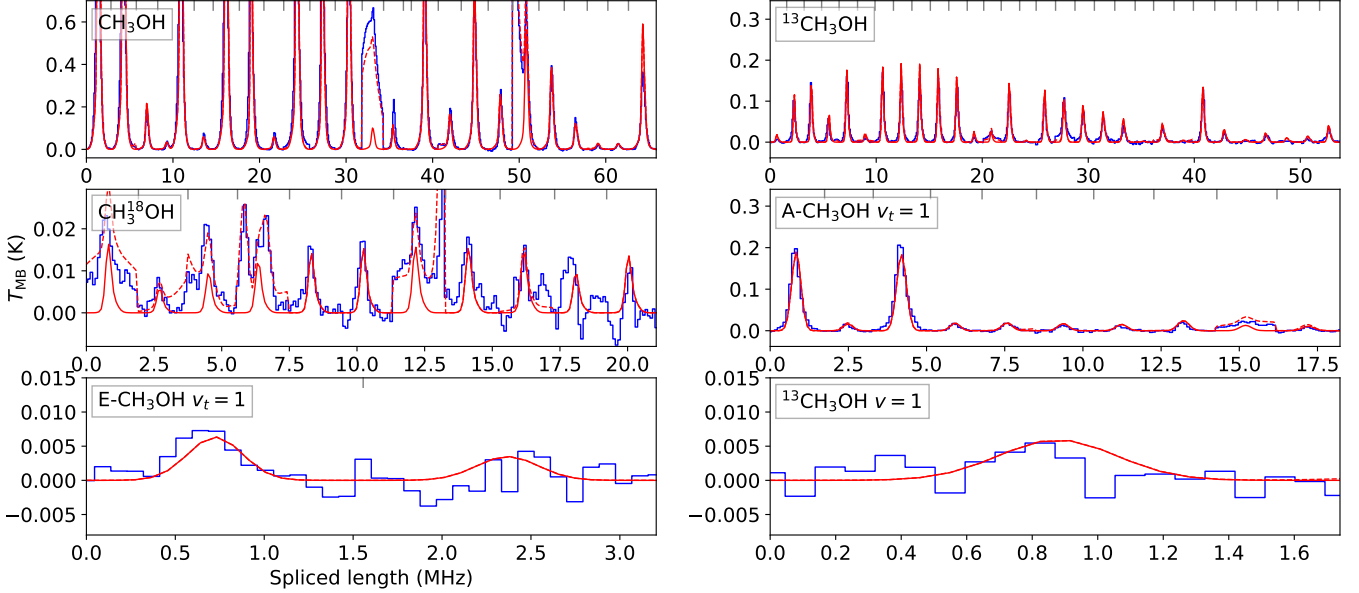


Figure 10. The blue lines are the spliced spectra of CH_3OH and its isotopologues as well as these species in vibrationally excited states. The spectrum between two neighbouring upper ticks are independent frequency segment. The red solid lines show the result of the model fitting of the corresponding species. The red dashed lines include the modeled emission of all species and RRLs. See Fig. 17 for other molecular species detected in the Ka-band survey.

report of high-order ion RRLs (even for He^+) with $\Delta n > 1$ in the literature. The ionization energy of C II, 24.383 eV, is close to the value of He I, 24.587 eV, and thus the C III region should be comparable with the He II region in size. Thus, these α lines were assigned to C^+ RRLs (Liu et al. 2023). However, the contribution of oxygen can not be excluded, because oxygen is as abundant as carbon, and the rest frequency shift between C^+ and O^+ RRLs is small ($\sim 3.5 \text{ km s}^{-1}$). Interferometers may help to break the coupling between RRLs of C^+ and O^+ since they have different ionization energies (**and therefore are presumably at different location**), while single dish is difficult to distinguish them. Below, we tried to improve the S/Ns of ion RRLs through stacking, aiming to search for ion RRLs with $\Delta n > 1$ from this Ka-band survey of the TMRT (Section 4.3.1) and to find signals of ion RRLs from independent telescopes beyond the TMRT (Section 4.3.2).

4.3.1. Stacking of the Ka-band data of TMRT

For $X^+n\beta$ with an even $n = 2m$, Equation 1 leads to

$$\begin{aligned} v_{\text{rest}}^{\text{RRL}}(2m+2, 2m) &= \frac{m'_e(X)}{m_e} R_\infty c 2^2 \left(\frac{1}{(2m)^2} - \frac{1}{(2m+2)^2} \right) \\ &\sim \frac{m'_e(\text{He})}{m_e} R_\infty c \left(\frac{1}{(m)^2} - \frac{1}{(m+1)^2} \right), \end{aligned} \quad (3)$$

and thus they should be blended with the α lines of neutral RRLs of helium (upper panel of Figure 8). For odd n , four β lines of ion RRLs ($n = 125, 129, 117$, and 115) show tentative line features. The 121β and 123β can not be recognized

because of limited S/Ns, but do not contradict the model (Figure 8). Thus, it is very likely that we have detected the β lines of ion RRLs.

To confirm the detection of β lines and to search for higher-order ion RRLs, we stacked the spectra of different transitions to improve the S/N. We first check the Ka-band data, including both the observed and the modeled spectrum (Section 3.2), to select the spectral segments around the frequencies of ion RRLs (Equation 1) that are not blended by any other transitions within 20 km s^{-1} (Figure 8). For a given Δn , we stacked all the corresponding unblended segments (with different n) aligned by velocity. The stacking was conducted with equal weights for different segments. The left panels of Figure 9 show the stacked Ka-band spectra of the α, β and γ lines of ion RRLs.

It's natural to see the high-S/N signal of the stacked α line since each unblended α line of ion RRLs can be clearly recognized (Liu et al. 2023). Besides the α lines, the stacked β line shows clear detection (6σ ; Figure 9), and the stacked γ line shows very marginal signal. This is the first firm detection of ion RRLs with $\Delta n > 1$ originated from the interstellar medium. We stacked the modeled data with the same procedure to obtain the stacked spectra (shown as the orange lines in Figure 9). In Liu et al. (2023), the fitting of ion RRLs was conducted based on α lines in three bands (Ku, Ka and Q). Here, we fitted them based on the Ka-band data only, but taking into account all the α, β , and γ lines. The fitted values of EM ($1.3 \times 10^3 \text{ cm}^{-6} \text{ pc}$), the abundance of X^{2+} (8.8×10^{-3}) and the line width (17 km s^{-1}) are not altered compared with

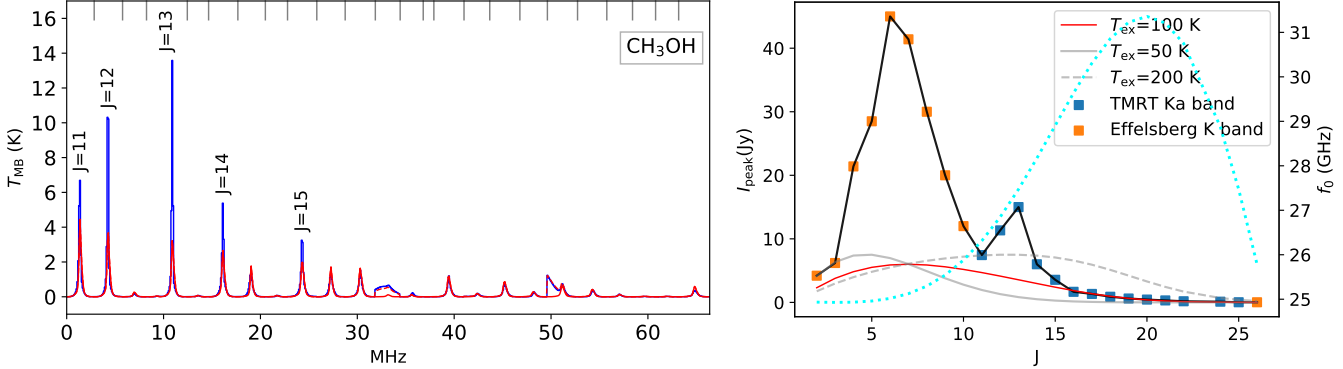


Figure 11. Left: The spliced spectrum of CH_3OH , same as the upper left panel of Figure 10, but with a different y-axis scale. The labeled transitions are $J_{K_a, K_c} = J_{2,J-1} - J_{1,J-1}$. Right: The peak intensities (I_{peak}) of CH_3OH $J_{2,J-1} - J_{1,J-1}$ detected in this survey (blue squares) and in the K-band survey of Gong et al. (2015) (orange squares). The red solid, gray dashed, and gray solid lines show the predicted peak intensity distribution along J under LTE with a T_{ex} of 100 K, 200 K, and 50 K, respectively. The cyan line shows the rest frequency (f_0) of the transitions with different J .

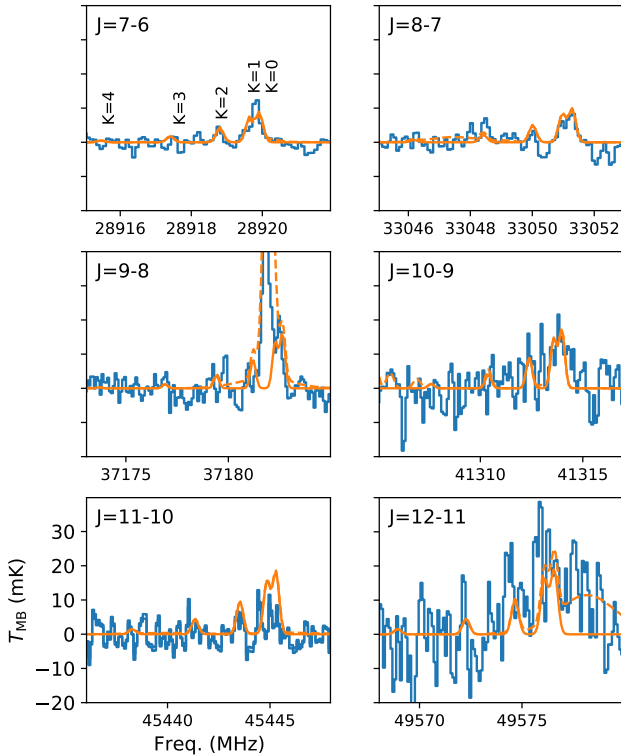


Figure 12. The spectra of $\text{CH}_3\text{C}_3\text{N}$ (blue) in the Ka and Q bands. The y-axis in all panels have the same scale. Each rotational line is split into several transitions by the value of K , as marked in the upper-left panel. The orange solid lines are the model fitting of $\text{CH}_3\text{C}_3\text{N}$, and the orange dashed lines have taken all species into account. All transitions of $\text{CH}_3\text{C}_3\text{N}$ expected to be stronger than 5 mK have been shown here.

the values reported in Liu et al. (2023). The V_{LSR} fitted from the stacked spectra is -6.5 km s^{-1} (with respect to the rest frequencies of C^+ RRLs), slightly bluer than the value (-5.5 km s^{-1}) in Liu et al. (2023).

Comparing the relative intensities between the observation and model can provide an empirical test of the departures from LTE. The stacked γ line seems to be slightly stronger than the modeled spectrum (bottom left panel of Figure 9), hinting at the deviation from LTE. However, the S/Ns of the stacked β and γ lines are not high enough to dig into this issue, and further observations with deeper sensitivities are needed to confirm it.

4.3.2. Comparison with the archived data of Effelsberg

We also checked the archive data of the K-band survey of Orion KL observed by Gong et al. (2015) using the Effelsberg 100 m telescope to search for the signals of ion RRLs. All α lines of ion RRLs in the K band can be recognized marginally or with moderate S/Ns, except for the blended $\text{X}^+109\alpha$ and the $\text{X}^+102\alpha$ which is located at the frequency gap of the K-band survey (see Appendix B and Figure 15). The intensities and velocities of the α lines of ion RRLs in the K band are consistent with the model prediction based on the Ka-band data. Using the same procedure in Section 4.3.1, we stacked the unblended ion RRLs in the K band. No clear signals of β and γ lines can be seen on the stacked spectra of the Effelsberg K-band survey because of the limited sensitivity. The signal of the α line can be clearly seen on the stacked spectrum (see the top right panel of Figure 9). This provides a very important cross check of ion RRLs from an independent facility.

5. MOLECULAR LINES

In total, 318 molecular lines were identified (Table 2), and they can be assigned to 37 species. Among them, 10 species (marked by (\dagger) in Table 4) have no transitions being detected by the Q-band survey of the TMRT, because of the limited S/Ns or the lacking of transitions in the Q band. The vibrationally excited states ($v_t > 0$) of nine species were detected, including the eight ones listed in Table 4 and $\text{C}_2\text{H}_5\text{CN}$ v_{13}/v_{21}

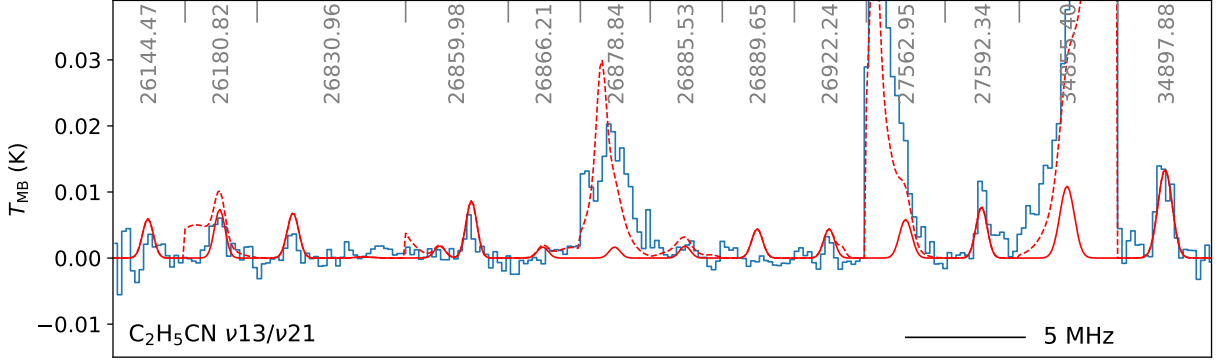


Figure 13. The spliced spectrum of $\text{C}_2\text{H}_5\text{CN}$ ν_{13}/ν_{21} . The meaning of solid and dashed red lines are same as that of the upper left panel of Figure 10. The center frequencies of each segment are marked by the gray text labels.

(Section 5.2.2). For each detected transition, some transition parameters were quoted from the CDMS (Müller et al. 2001) and JPL (Pickett et al. 1998) through the Splatalogue². These parameters are the rest frequency (f_0), upper-level energy (E_u), Einstein coefficients (A_{ij}), upper-level degeneracy (g_u), and partial function (Q). The f_0 and A_{ij} for transitions of $\text{C}_2\text{H}_5\text{CN}$ ν_{13}/ν_{21} were obtained from Endres et al. (2021). Through Equations 9, 10 and 11 of Liu et al. (2022), we modeled the emission of molecules. For most species, constraining T_{ex} is challenging due to the similar upper level energies of their different transitions. Therefore, T_{ex} is manually set to 50 K, 100 K, 150 K, 200 K, or, 300 K. We have also referred to the literature (Tercero et al. 2010; Gong et al. 2015; Rizzo et al. 2017; Liu et al. 2023) to choose proper T_{ex} . To reproduce the emission of isotopologues or species with similar chemical characteristics, we tend to adopt the same fixed values of T_{ex} , and use a similar initial guesses for their fitted parameters, including the column density (N), line width (ΔV) and velocity (V_{LSR}). We try to model the spectrum with as few velocity components as possible. The velocity resolution of the Ka-band survey is worse than that of the Q band, and species showing multiple velocity components may only show a single velocity component in the Ka band. For species detected in the Q band, if the modeled spectrum does not deviate much (less than 20 percent) from the observed spectrum in the Ka band, the number of the velocity components and the physical parameters fitted from the Q-band data will be directly used with no modification. The fitted parameters of molecular species are shown in Table 4.

5.1. Methanol emission

In total, 67 line features are assigned to methanol and its isotopologues, CH_3OH , $^{13}\text{CH}_3\text{OH}$, $\text{CH}_3^{18}\text{OH}$, A- CH_3OH $v_t = 1$, E- CH_3OH $v_t = 1$, and $^{13}\text{CH}_3\text{OH}$ $v_t = 1$ (Figure

10). Among them, $\text{CH}_3^{18}\text{OH}$ and $^{13}\text{CH}_3\text{OH}$ $v_t = 1$ were not detected in the Q-band survey (Liu et al. 2022). Methanol contributes more about half the Ka-band molecular emission of Orion KL (Figure 5). Besides thermal components (Section 5.1.1), the maser emission of methanol is also evident, as we discuss in Section 5.1.2.

5.1.1. Methanol thermal emission

We adopted three velocity components to fit the Ka-band spectra of CH_3OH under the assumption of LTE as in the Q band (Liu et al. 2022). The Ka-band emission of CH_3OH are dominated by strong lines ($T_{\text{peak}} > 1$ K), with sharp peaks that are not fully resolved under the current spectral resolution (the left panel of Figure 11). Thus, the emission of CH_3OH were reproduced with the narrow ($\Delta V = 2 \text{ km s}^{-1}$), moderate ($\Delta V = 4 \text{ km s}^{-1}$), and broad velocity components ($\Delta V = 10 \text{ km s}^{-1}$). Under the assumption of LTE, T_{ex} of the moderate component (150 K) is larger than that of the narrow component (100 K; Table 4). The column density ratio of $\text{CH}_3\text{OH}/^{13}\text{CH}_3\text{OH}$ and $^{13}\text{CH}_3\text{OH}/\text{CH}_3^{18}\text{OH}$ are 20 and 3.6, respectively. The $\text{CH}_3\text{OH}/^{13}\text{CH}_3\text{OH}$ is slightly larger than the values (5–15) of Rizzo et al. (2017), and smaller than the typical abundance ratio of Galactic ^{12}C and ^{13}C (several tens; Williams et al. 1994). This maser effects may influence this abundance ratio (Section 5.1.2). The $^{13}\text{CH}_3\text{OH}/\text{CH}_3^{18}\text{OH}$ is slightly lower than the abundance ratio of $^{13}\text{CO}/\text{C}^{18}\text{O}$ ($X^{13/18}$) in local ISM (Wilson 1999; Shimajiri et al. 2014).

The spectral lines of CH_3OH $v_t = 1$ (in both A and E asymmetry) have line widths of $\sim 4 \text{ km s}^{-1}$. Adopting the excitation temperature ($T_{\text{ex}} = 150 \text{ K}$) and the column density of the moderate component fitted from the emission of $^{13}\text{CH}_3\text{OH}$ (Table 4), all line features of CH_3OH $v_t = 1$ can be reproduced with a deviation no more than 10 percent (Figure 10). It implies that the vibrationally excited CH_3OH is mainly associated with the moderate component (instead of the narrow component). The narrow, moderate, and broad velocity components may originate from the compact ridge, hot core, and plateau, respectively (Rizzo et al. 2017).

² <https://splatalogue.online/>

Table 4. Model parameters of molecules ⁽¹⁾

Species	size ⁽²⁾ ('')	T_{ex} (K)	$N_{\text{tot}}^{(3)}$ (cm $^{-2}$)	ΔV (km s $^{-1}$)	V_{lsr} (km s $^{-1}$)
H ₂ CS	20	100	1.8e+15	4.0	8.0
CCS	30	100	1.2e+13	8.0	7.5
SO	15	100	1.2e+17	15.0	6.0
	15	100	2.2e+17	25.0	9.0
³⁴ SO	15	100	4.8e+15	15.0	6.0
	15	100	9.6e+15	25.0	9.0
SO ₂	40	50	5.0e+15	4.0	7.0
	40	200	6.0e+15	10.0	7.0
	40	100	1.9e+16	25.0	7.5
³⁴ SO ₂	40	50	1.0e+14	4.0	7.0
	40	200	6.0e+14	10.0	7.0
	40	100	6.0e+14	25.0	7.5
HCN $v_2 = 1$	15	200	1.8e+17	4.0	5.0
HC ₃ N	15	100	3.0e+14	3.0	9.0
	15	100	4.0e+14	7.0	5.5
	15	100	6.0e+14	15.0	5.5
	30	100	1.2e+14	25.0	6.0
H ¹³ CCCN	20	100	1.4e+13	4.0	9.0
	15	100	2.4e+13	7.0	5.5
HC ¹³ CCN	20	100	1.4e+13	4.0	9.0
	15	100	2.4e+13	7.0	5.5
HCC ¹³ CN	20	100	1.4e+13	4.0	9.0
	15	100	2.4e+13	7.0	5.5
HC ₃ N $v_6 = 1$	15	150	3.0e+15	7.0	5.5
HC ₃ N $v_7 = 1$	10	150	5.0e+15	7.0	4.5
	10	100	4.0e+15	25.0	6.0
HC ₃ N $v_7 = 2$	10	150	3.0e+15	7.0	4.5
HC ₅ N	15	100	4.0e+13	4.0	8.5

⁽¹⁾ Take caution if the modeled parameters (e.g. N_{tot}) are compared with other work because of the uncertainties of size and T_{ex} and source size.

⁽²⁾ The size of emission region can not be constrained by single-dish observation. The size of 40 '' is corresponding to the extended case. If another emission source size is adopted, the column densities could be recalculated through multiplying the values listed here by a factor of (size/size^{new})².

⁽³⁾ For species in vibrational state, the column density (N_{tot}) has taken into account the ground-state molecule.

^(†) dnotes the species that have not been detected in the TMRT Q-band line survey.

5.1.2. Methanol masers

Several strong lines of CH₃OH ($T_{\text{peak}} > 3$ K) can not be successfully reproduced properly with any T_{ex} (Figure 11). Those lines belong to the same group of the transitions of E-type methanol (E-CH₃OH $J_{K_a, K_c} = J_{2,J-1} - J_{1,J-1}$) with $11 \leq J \leq 15$, and their rest frequencies are located within

Table 4 (continued)

Species	size ('')	T_{ex} (K)	N_{tot} (cm $^{-2}$)	ΔV (km s $^{-1}$)	V_{lsr} (km s $^{-1}$)
C ₂ H ₃ CN	8	320	3.6e+14	6.0	5.0
	15	100	1.2e+14	6.0	5.0
	8	200	1.1e+14	20.0	3.0
	15	90	1.6e+14	20.0	3.0
C ₂ H ₅ CN	8	275	1.9e+16	5.0	5.5
	15	110	1.4e+15	13.0	4.0
	30	65	3.0e+14	20.0	4.0
CH ₃ NH ₂	20	100	2.4e+14	4.0	5.0
CH ₃ OH	40	100	1.2e+16	2.0	7.0
	40	150	2.0e+16	4.0	6.0
	40	150	1.0e+16	10.0	7.0
¹³ CH ₃ OH	40	100	8.0e+14	2.0	7.0
	40	150	8.0e+14	4.0	6.0
A-CH ₃ OH $v_t = 1$	40	150	2.0e+16	4.0	6.0
E-CH ₃ OH $v_t = 1$	40	150	2.0e+16	4.0	6.0
C ₂ H ₅ OH	20	60	7.2e+14	4.0	7.0
H ₂ CO	40	50	6.0e+14	25.0	5.0
	20	50	6.0e+15	3.0	7.0
	15	150	1.0e+16	10.0	4.5
H ₂ ¹³ CO	20	50	2.0e+14	3.5	7.0
H ₂ CCO	15	100	1.8e+15	3.0	7.0
CH ₃ CHO	15	50	2.4e+14	3.0	8.0
	30	150	2.4e+14	25.0	9.0
CH ₃ OCHO	40	60	4.8e+14	4.0	8.0
	40	150	1.9e+15	25.0	9.0
	20	110	1.7e+16	4.0	7.5
	15	300	2.4e+16	4.0	7.5
	15	250	7.7e+15	10.0	5.5
CH ₃ OCHO $v_t = 1$	20	100	1.1e+16	3.0	7.0
c-CH ₂ OCH ₂	20	50	8.0e+13	3.0	6.5
	20	50	2.0e+13	1.5	6.5
CH ₃ OCH ₃	20	100	2.0e+16	3.0	7.5
CH ₃ COCH ₃	10	100	1.8e+15	4.0	5.5
NH ₃	10	300	1.2e+16	20.0	8.0
	20	250	2.4e+16	8.0	6.0
NH ₂ D	20	300	4.0e+14	5.0	6.0
¹⁵ NH ₃ ^(†)	20	300	1.0e+14	8.0	6.0
¹³ CH ₃ OH $v_t = 1^{(\dagger)}$	40	150	1.0e+15	4.0	6.0
CH ₃ C ₃ N ^(†)	40	50	2.0e+12	2.5	9.0
CH ₃ CCH ^(†)	8	50	1.5e+16	3.0	9.0
CH ₃ ¹⁸ OH ^(†)	40	100	2.2e+14	2.0	7.0
	40	150	2.2e+14	4.0	6.0
HC ₇ N ^(†)	15	100	6.0e+12	4.0	8.5
HDCO ^(†)	20	50	2.0e+14	4.0	8.5
¹⁸ OCS ^(†)	40	100	3.0e+13	3.0	7.0
³³ SO ^(†)	15	100	3.0e+15	15.0	6.0
c-C ₃ H ₂ ^(†)	15	150	2.0e+14	4.0	8.5

Table 5. The species detected in the Ka-band survey

H ^{+(†)}	³⁴ SO	HCC ¹³ CN	CH ₃ NH ₂ ^(*)	H ₂ ¹³ CO	CH ₃ COCH ₃	CH ₃ ¹⁸ OH ^(‡)
He ^{+(†)}	SO ₂	HC ₃ N $v_6 = 1$	CH ₃ OH	H ₂ CCO	NH ₃	HC ₇ N ^(‡)
C ^{+(†)}	³⁴ SO ₂	HC ₃ N $v_7 = 1$	¹³ CH ₃ OH	CH ₃ CHO	NH ₂ D	HDCO ^(‡)
X ^{2+(†)}	HCN $v_2 = 1$	HC ₃ N $v_7 = 2$	A-CH ₃ OH $v_t = 1$	CH ₃ OCHO	¹⁵ NH ₃ ^(‡)	¹⁸ OCS ^(‡)
H ₂ CS	HC ₃ N	HC ₅ N	E-CH ₃ OH $v_t = 1$	CH ₃ OCHO $v_t = 1$	¹³ CH ₃ OH $v = 1$ ^(‡)	³³ SO ^(‡)
CCS	H ¹³ CCCN	C ₂ H ₃ CN	C ₂ H ₅ OH	c-CH ₂ OCH ₂	CH ₃ C ₃ N ^(‡)	c-C ₃ H ₂ ^(‡)
SO	HC ¹³ CCN	C ₂ H ₅ CN	H ₂ CO	CH ₃ OCH ₃	CH ₃ CCH ^(‡)	C ₂ H ₅ CN v_{13}/v_{21}

Note: The species marked by ^(†) ions are traced by RRLs, e.g., X²⁺ was traced by X⁺ RRLs. The species marked by ^(‡) are detected in this Ka-band survey but not in the Q-band survey of TMRT. The species marked by ^(*) are only tentatively detected.

26–29 GHz. It is consistent with the observations of Wilson et al. (1996), which detected narrow line components with $\Delta V \sim 0.8 \text{ km s}^{-1}$ for $12 \leq J \leq 17^3$ in the Ka band and assigned them to low gain maser regions. In Wilson et al. (1996), the peak intensity of the maser component is comparable with that of the thermal component. The observed intensity of the transition with $J = 13$ by TMRT is four times stronger than the value of LTE prediction, showing the most significant deviation (Figure 11).

The transitions of E-CH₃OH in this group with $2 \leq J \leq 9$ are well-known Class I maser transitions⁴ with rest frequencies located in the K band (Menten et al. 1986; Gong et al. 2015; Ladeyschikov et al. 2019). Combining the data of this work and Gong et al. (2015), we plotted the profile of the peak intensities (I_p) along J with $2 \leq J \leq 16$ in the right panel of Figure 11. Under the assumption of LTE, for compact source with an angular size smaller than the beam size, the profile of I_{peak} along J can be calculated through

$$I_p \propto A_{ij} g_u \exp(-E_u/T_{\text{ex}}). \quad (4)$$

Here, E_u is in units of K. Three different values of T_{ex} (50, 100, and 200 K) were adopted, and all three profiles of I_p can not fit all the Ka-band data points simultaneously (Figure 11). The data points with $J > 15$ could be fitted adopting a T_{ex} of 100 K, and thus should be dominated by thermal emission. Note that the rest frequencies increase with J for $J < 20$, but decrease with J for $J > 20$ (see the cyan line in Figure 11). The rest frequency of the transition with a J of 26 falls back to the K band, and its peak intensity is consistent with value extrapolated from the Ka-band data (Figure 11). Thus, the line of $J = 26$ can be explained by the LTE fitting, consistent with the interpretation of Gong et al. (2015).

Previously, it is known that the maser effect would increase with J from 2 to 6 and decrease with J from 6 to 10 (Menten et al. 1986; Gong et al. 2015). The Ka-band data of this survey shows that the maser effect may increase with J again from 11 to 13, and then decrease with J from 13 to 15. These

masers are likely class I methanol masers as well (Johnston et al. 1992; Wilson et al. 1996). The second peak can not simply be explained by the uncertainty of intensity calibration. The thermal lines of CH₃OH and other species in Ka band can all be well reproduced by the LTE model (Figures 3 and 10). Especially, the intensities of all the transitions of ¹³CH₃OH (upper right panel of Figure 10) are consistent with the LTE model within 20 percent (the calibration uncertainty; Section 2). To model the emission of ¹³CH₃OH, we adopted the same physical parameters as those for CH₃OH, except for the column densities, which have been scaled down (Table 4). The reason of the existence of two bumping peaks for E-CH₃OH $J_{K_a, K_c} = J_{2,J-1} - J_{1,J-1}$, at $J \sim 6$ and $J \sim 13$, is still unknown. Interferometer observations are needed to confirm this issue through spatially resolving their different emission components.

5.2. N-bearing species

5.2.1. Methylcyanoacetylene (CH₃C₃N)

Methylcyanoacetylene (CH₃C₃N) was first detected in TMC-1 by Broten et al. (1984), with a column density of $4.5 \times 10^{11} \text{ cm}^{-1}$ under a T_{ex} of 4 K (Lovas et al. 2006). It has also been detected in high-mass protostellar molecular clumps (Guzmán et al. 2018) and the Titan's atmosphere (Thelen et al. 2020). However, CH₃C₃N has not been detected in Orion KL, even by the ALMA interferometer (Paganini et al. 2017).

In this Ka-band survey, we matched two groups of the emission lines of CH₃C₃N ($J = 7 - 6$ and $J = 8 - 7$; see Figure 17 and the upper two panels of Figure 12). The transitions of $K = 0$ (blended with $K = 1$) were detected for both groups. The transitions of $K=2$ ($E_u \sim 35 \text{ K}$) and $K=3$ ($E_u \sim 75 \text{ K}$) were tentatively detected. Thus, a T_{ex} of 50 K was adopted to fit the emission of CH₃C₃N, yielding a column density of $2 \times 10^{12} \text{ cm}^{-2}$. Here, we assumed that the emission of CH₃C₃N is extended with a beam filling factor of unity. Further, we compared the modeled and observed spectra in the Q band, and found that they are also consistent with each other (Figure 12).

The fitted velocity (V_{LSR}) is 9 km s^{-1} , slightly redder than the systematic velocity (6 km s^{-1}) but consistent with that of

³ E-CH₃OH $J_{K_a, K_c} = J_{2,J-1} - J_{1,J-1}$ were denoted as E-CH₃OH $J_K = J_2 - J_1$ with K_c being omitted in Wilson et al. (1996).

⁴ <https://maserdb.net/transitions.pl?molecule=MET1&>

CH_3CCH (Table 4), C RRLs (Section of 4.1), and the ambient gas of Orion KL (the extended ridge; Blake et al. 1986; Schilke et al. 1997). It implies that the $\text{CH}_3\text{C}_3\text{N}$ emission of Orion KL may be associated with the PDRs or ambiment gas of Orion KL. This is reasonable since $\text{CH}_3\text{C}_3\text{N}$ should be chemically young, given that it is an unsaturated species with its transitions mainly detected in chemically young environments, e.g., the starless core TMC-1 (Broten et al. 1984; Lovas et al. 2006).

5.2.2. Ethyl cyanide ($\text{C}_2\text{H}_5\text{CN}$)

Ethyl cyanide ($\text{C}_2\text{H}_5\text{CN}$) is a common tracer of hot molecular gas (e.g., Cazaux et al. 2003; Qin et al. 2022), and its vibrational satellites can be intense in sub-millimeter bands (Endres et al. 2021). In this survey, besides $\text{C}_2\text{H}_5\text{CN} \nu = 0$, rotational transitions of $\text{C}_2\text{H}_5\text{CN} \nu_{13}/\nu_{21}$ (excited in bending or torsion modes; Daly et al. 2013) can also be detected (Figure 13). In total, four lines of $\text{C}_2\text{H}_5\text{CN} \nu_{13}/\nu_{21}$ were detected, less than the number of lines of $\text{C}_2\text{H}_5\text{CN} \nu_{13}/\nu_{21}$ detected in the Q band (Liu et al. 2022). Due to the higher spectral sensitivity of the Ka-band survey, the transition of $\text{C}_2\text{H}_5\text{CN} \nu_{13}/\nu_{21}$ at 34897.89 MHz, which was not detected in the Q band, can be clearly seen on the Ka-band spectrum (Figure 13). The other three transitions are located within 26–28 GHz. This marks the first detection of $\text{C}_2\text{H}_5\text{CN} \nu_{13}/\nu_{21}$ in the centimeter band.

To fit the emission of $\text{C}_2\text{H}_5\text{CN} \nu_{13}/\nu_{21}$, we adopted the transition parameters of $\text{C}_2\text{H}_5\text{CN} \nu_{13}/\nu_{21}$ from Endres et al. (2021) and assumed a T_{ex} of 50 K as in (Liu et al. 2022). Since we do not know the partition function, the column density can not be derived and the fitted parameters are thus not listed in Table 4. Here, we adopt the partition function of $\text{C}_2\text{H}_5\text{CN}$ quoted from the CDMS. The velocity and line width are fitted to be 5 km s⁻¹ and 6 km s⁻¹, respectively, consistent with the result fitted from the Q-band data (Liu et al. 2022). The fitted column density of $\text{C}_2\text{H}_5\text{CN}$ is 2×10^{15} cm⁻². All transitions can be well fitted except for that in 26889 MHz. We note that this is not influenced by the T_{ex} , because this transition and the strong line at 27592 MHz have similar E_u (~ 300 K).

5.2.3. Cyanopolyyynes (HC_{2n+1}N)

Cyanopolyyynes (HC_{2n+1}N) are abundant in kinds of environments, especially the cold cores (Herbst & Leung 1989; Wu et al. 2019) and the envelopes of late-type carbon stars (Pardo et al. 2020), but not prominent in Orion KL. HC_7N was not detected by the Q-band (Liu et al. 2022) and K-band (Gong et al. 2015) line surveys of Orion KL. In this survey, spectral lines of HC_7N were detected with a peak intensity of ~ 5 mK (Figure 17). The LTE fitting with a T_{ex} of 100 K yields a column density of 6×10^{12} cm⁻² and a V_{LSR} of 8.5 km s⁻¹. The V_{LSR} of HC_{2n+1}N is consistent with that of HC_5N (8.5 km s⁻¹), and the V_{LSR} of the reddest velocity

component of HC_3N (9 km s⁻¹). The column density ratio of $N(\text{HC}_3\text{N})/N(\text{HC}_5\text{N})$ is 35 (Table 4), close to the value derived by Gong et al. (2015), but much smaller than the column density ratio of $N(\text{HC}_5\text{N})/N(\text{HC}_7\text{N})$, 6.6. However, if we only take the reddest velocity component of HC_3N into account, the abundance ratio of $N(\text{HC}_3\text{N})/N(\text{HC}_5\text{N})$ would be 7.5, close to the value of $N(\text{HC}_5\text{N})/N(\text{HC}_7\text{N})$. Thus, it is likely that the emission of HC_5N , HC_7N , and the reddest velocity component of HC_3N originates from the same region, probably the extended ridge of Orion KL.

5.2.4. Ammonia (NH_3 and NH_2D)

In total, 19 lines of ammonia were detected in this survey, including two lines of deuterated ammonia (NH_2D). Among them, NH_3 inversion line of $J_K = 14_{13}$ (27772 MHz) has the highest E_u of 2090 K. The emission lines of NH_3 should be optically thick and we did not try to precisely fit them. To explain the high- E_u lines, a component with a T_{ex} of 300 K was adopted. Among the two lines of NH_2D , one is for the *para*- NH_2D (30979 MHz), and the other one for the *ortho*- NH_2D (29188 MHz). Under the equilibrium state, the abundance ratio of *ortho*- NH_2D /*para*- NH_2D (*o/p*) should be 3, the ratio of their statistical weights. When we fitted the NH_2D emission, the T_{ex} was fixed to be 300 K and the *o/p* was fixed to be 3 since we did not distinguish the two types of NH_2D . Hence, the free parameters are only the column density (N), line width (ΔV) and velocity (V_{LSR}). The two lines can be fitted simultaneously (Figure 17), and thus the assumption of LTE should be acceptable. Only one line of $^{15}\text{NH}_3$ is detected, and the column density of $^{15}\text{NH}_3$ is calculated by adopting a T_{ex} of 300 K. The abundance ratio of $\text{NH}_2\text{D}/^{15}\text{NH}_3$ is derived to be 4, but it highly depends on the T_{ex} and the assumption of LTE for $^{15}\text{NH}_3$.

5.3. Other species

For S-bearing species, ^{33}SO and ^{18}OCS , which have not been detected in the Q-band survey of TMRT, were detected in the Ka band (Table 4). The abundance ratio of $^{34}\text{SO}/^{33}\text{SO}$ is derived to be 4.8, which does not deviate much from the value of Esplugues et al. (2013), ~6.

All O-bearing complex organic molecules detected in this survey (Table 5), except for the isotopologues of CH_3OH (Section 5.1), have been detected by the Q-band survey of the TMRT (Liu et al. 2022). HDCO was not detected in the Q-band survey. For HDCO and H_2^{13}CO , only one transition was detected for each in this survey. Adopting the same value of T_{ex} of 50 K, the abundance ratio of $\text{H}_2^{13}\text{CO}/\text{HDCO}$ is ~ 1 . Forty lines of CH_3OCH_3 were detected in this survey. In the Ka band, the total emission flux of CH_3OCH_3 is comparable with that of $\text{C}_2\text{H}_5\text{CN}$ (Figure 5). In contrast, in the Q band, the total emission flux of CH_3OCH_3 is only 60 percent of that of $\text{C}_2\text{H}_5\text{CN}$. In the K band, only two lines of CH_3OCH_3 were detected by Gong et al. (2015). It implies that the Ka

band has superiorities in detecting some species of complex organic molecules compared to the K and Q bands.

6. SUMMARY

We have conducted a Ka-band line survey (26.1–35 GHz) towards Orion KL using the TMRT, following the Q-band survey with the same instrument (Liu et al. 2022). This survey achieved a line sensitivity of mK level (1–3 mK) at a spectral resolution of $\sim 1 \text{ km s}^{-1}$. This is the first blind line survey in the Ka band, and many transitions were detected for the first time. Further, we explore the Ka-band spectrum of Orion KL and present the overall preliminary results of the survey. The main results include:

- 1 We have obtained and release the Ka-band spectrum of Orion KL by the TMRT. In the spectrum, 592 Gaussian features are detected in total, including 257 unblended RRLs and 318 unblended molecular lines. The maximum Δn of RRLs of H, He, and C reach 20, 15, and 5, respectively. In total, 37 molecular species were detected, and the vibrationally excited states ($v_t > 0$) of nine of these species were detected. Ten of these species have not been detected in the Q-band survey of TMRT, including CH₃C₃N which was not detected in Orion KL previously even by ALMA. A catalog of these lines is presented.
- 2 Through stacking, we have detected the β lines of ion RRLs (RRLs of C⁺ and/or O⁺) for the first time, following our previous report of the α lines of ion RRLs. Tentative signal of the γ lines of ion RRLs can be seen on the stacked spectrum. We also successfully matched the α lines of ion RRLs from the archive data of the K-band survey of Orion KL by the Effelsberg 100 m (Gong et al. 2015), providing a very important cross check of ion RRLs from an independent facility besides the TMRT.

3 We modeled the spectral emission under the assumption of LTE. Parameters including the column densities (N) of molecular species and the emission measures (EM) of RRLs were derived. Adopting the precise values of the absorption oscillator strength of RRLs ($f_{n1,n2}$), the intensities of nearly all RRLs can be reproduced within a deviation of 50 percent. For $\Delta n > 10$, the observed intensities tend to be slightly lower than model fitting.

4 Most species can be well fitted under the assumption of LTE except for CH₃OH. The intensities of some transitions of E-CH₃OH $J_2 - J_1$ can be at most four times the values of LTE prediction. The maser effect may explain this deviation (Wilson et al. 1996). Combining the data in Ka (this survey) and K band (Gong et al. 2015), we found that besides the bumping peak at $J \sim 6$, there is another one at $J \sim 13$.

Overall, this work emphasizes that the TMRT is able to conduct deep line surveys in the Ka band, and this band is very useful for surveying RRLs and molecular lines simultaneously.

¹ We wish to thank the staff of the TMRT 65 m for their help during the observations. This work has been supported by the National Key R&D Program of China (No. 2022YFA1603100).
² X.L. acknowledges the supports by NSFC No. 12203086 and No. 12033005 and CPSF No. 2022M723278. T.L. acknowledges the supports by National Natural Science Foundation of China (NSFC) through grants No.12073061 and No.12122307, the international partnership program of Chinese Academy of Sciences through grant No.114231KYSB20200009, Shanghai Pujiang Program 20PJ1415500 and the science research grants from the China Manned Space Project with no. CMS-CSST-2021-B06. D.S. acknowledges the support from Ramanujan Fellowship (SERB) and PRL, India. We show warm thanks to the anonymous referee for providing many deep-insight comments for improving the paper.

Facilities: Tianma 65 m (TMRT)

Software: GILDAS/CLASS (Guilloteau & Lucas 2000), astropy (Astropy Collaboration et al. 2013)

REFERENCES

- Astropy Collaboration, Robitaille, T. P., Tollerud, E. J., et al. 2013, *A&A*, 558, A33, doi: [10.1051/0004-6361/201322068](https://doi.org/10.1051/0004-6361/201322068)
- Bell, M. B., Avery, L. W., MacLeod, J. M., & Vallée, J. P. 2011, *Ap&SS*, 333, 377, doi: [10.1007/s10509-011-0662-5](https://doi.org/10.1007/s10509-011-0662-5)
- Bernal, J. J., Koelemay, L. A., & Ziurys, L. M. 2021, *ApJ*, 906, 55, doi: [10.3847/1538-4357/abc87b](https://doi.org/10.3847/1538-4357/abc87b)
- Blake, G. A., Sutton, E. C., Masson, C. R., & Phillips, T. G. 1986, *ApJS*, 60, 357, doi: [10.1086/191090](https://doi.org/10.1086/191090)
—. 1987, *ApJ*, 315, 621, doi: [10.1086/165165](https://doi.org/10.1086/165165)
- Brocklehurst, M. 1971, *MNRAS*, 153, 471, doi: [10.1093/mnras/153.4.471](https://doi.org/10.1093/mnras/153.4.471)
- Broten, N. W., MacLeod, J. M., Avery, L. W., et al. 1984, *ApJL*, 276, L25, doi: [10.1086/184181](https://doi.org/10.1086/184181)
- Bussa, S., & VEGAS Development Team. 2012, in American Astronomical Society Meeting Abstracts, Vol. 219, American Astronomical Society Meeting Abstracts #219, 446.10
- Cazaux, S., Tielens, A. G. G. M., Ceccarelli, C., et al. 2003, *ApJL*, 593, L51, doi: [10.1086/378038](https://doi.org/10.1086/378038)

- Chaisson, E. J., & Malkan, M. A. 1976, ApJ, 210, 108, doi: [10.1086/154807](https://doi.org/10.1086/154807)
- Corby, J. F., Jones, P. A., Cunningham, M. R., et al. 2015, MNRAS, 452, 3969, doi: [10.1093/mnras/stv1494](https://doi.org/10.1093/mnras/stv1494)
- Crockett, N. R., Bergin, E. A., Neill, J. L., et al. 2014, ApJ, 787, 112, doi: [10.1088/0004-637X/787/2/112](https://doi.org/10.1088/0004-637X/787/2/112)
- Cuadrado, S., Goicoechea, J. R., Pilleri, P., et al. 2015, A&A, 575, A82, doi: [10.1051/0004-6361/201424568](https://doi.org/10.1051/0004-6361/201424568)
- Daly, A. M., Bermúdez, C., López, A., et al. 2013, ApJ, 768, 81, doi: [10.1088/0004-637X/768/1/81](https://doi.org/10.1088/0004-637X/768/1/81)
- Dong, J., Zhong, W., Wang, J., Liu, Q., & Shen, Z. 2018, IEEE Transactions on Antennas and Propagation, 66, 2044, doi: [10.1109/TAP.2018.2796378](https://doi.org/10.1109/TAP.2018.2796378)
- Endres, C. P., Martin-Drumel, M.-A., Zingsheim, O., et al. 2021, Journal of Molecular Spectroscopy, 375, 111392, doi: [10.1016/j.jms.2020.111392](https://doi.org/10.1016/j.jms.2020.111392)
- Esplugaes, G. B., Tercero, B., Cernicharo, J., et al. 2013, A&A, 556, A143, doi: [10.1051/0004-6361/201321285](https://doi.org/10.1051/0004-6361/201321285)
- Genzel, R., & Stutzki, J. 1989, ARA&A, 27, 41, doi: [10.1146/annurev.aa.27.090189.000353](https://doi.org/10.1146/annurev.aa.27.090189.000353)
- Goldwire, H. C., Jr., & Goss, W. M. 1967, ApJ, 149, 15, doi: [10.1086/149225](https://doi.org/10.1086/149225)
- Gong, Y., Henkel, C., Thorwirth, S., et al. 2015, A&A, 581, A48, doi: [10.1051/0004-6361/201526275](https://doi.org/10.1051/0004-6361/201526275)
- Gordon, M. A., & Sorochenko, R. L. 2002, Radio Recombination Lines. Their Physics and Astronomical Applications, Vol. 282 (Berlin: Springer), doi: [10.1007/978-0-387-09604-9](https://doi.org/10.1007/978-0-387-09604-9)
- Gordon, W. 1929, Annalen der Physik, 394, 1031, doi: [10.1002/andp.19293940807](https://doi.org/10.1002/andp.19293940807)
- Guilloteau, S., & Lucas, R. 2000, in Astronomical Society of the Pacific Conference Series, Vol. 217, Imaging at Radio through Submillimeter Wavelengths, ed. J. G. Mangum & S. J. E. Radford, 299
- Guzmán, A. E., Guzmán, V. V., Garay, G., Bronfman, L., & Hechenleitner, F. 2018, ApJS, 236, 45, doi: [10.3847/1538-4365/aac01d](https://doi.org/10.3847/1538-4365/aac01d)
- Herbst, E., & Leung, C. M. 1989, ApJS, 69, 271, doi: [10.1086/191314](https://doi.org/10.1086/191314)
- Jacob, A. M., Menten, K. M., Gong, Y., et al. 2021, A&A, 647, A42, doi: [10.1051/0004-6361/202039906](https://doi.org/10.1051/0004-6361/202039906)
- Johansson, L. E. B., Andersson, C., Ellder, J., et al. 1984, A&A, 130, 227
- Johnston, K. J., Gaume, R., Stolovy, S., et al. 1992, ApJ, 385, 232, doi: [10.1086/170930](https://doi.org/10.1086/170930)
- Kardashev, N. S. 1959, Soviet Ast., 3, 813
- Ladeyschikov, D. A., Bayandina, O. S., & Sobolev, A. M. 2019, AJ, 158, 233, doi: [10.3847/1538-3881/ab4b4c](https://doi.org/10.3847/1538-3881/ab4b4c)
- Lerate, M. R., Barlow, M. J., Swinyard, B. M., et al. 2006, MNRAS, 370, 597, doi: [10.1111/j.1365-2966.2006.10518.x](https://doi.org/10.1111/j.1365-2966.2006.10518.x)
- Liu, X., Liu, T., Shen, Z., et al. 2022, ApJS, 263, 13, doi: [10.3847/1538-4365/ac9127](https://doi.org/10.3847/1538-4365/ac9127)
- . 2023, A&A, 671, L1, doi: [10.1051/0004-6361/202345904](https://doi.org/10.1051/0004-6361/202345904)
- Lovas, F. J., Remijan, A. J., Hollis, J. M., Jewell, P. R., & Snyder, L. E. 2006, ApJL, 637, L37, doi: [10.1086/500431](https://doi.org/10.1086/500431)
- Mangum, J. G., & Wootten, A. 1993, ApJS, 89, 123, doi: [10.1086/191841](https://doi.org/10.1086/191841)
- Menten, K. M., Reid, M. J., Forbrich, J., & Brunthaler, A. 2007, A&A, 474, 515, doi: [10.1051/0004-6361:20078247](https://doi.org/10.1051/0004-6361:20078247)
- Menten, K. M., Walmsley, C. M., Henkel, C., & Wilson, T. L. 1986, A&A, 157, 318
- Menzel, D. H. 1968, Nature, 218, 756, doi: [10.1038/218756a0](https://doi.org/10.1038/218756a0)
- Müller, H. S. P., Thorwirth, S., Roth, D. A., & Winnewisser, G. 2001, A&A, 370, L49, doi: [10.1051/0004-6361:20010367](https://doi.org/10.1051/0004-6361:20010367)
- Natta, A., Walmsley, C. M., & Tielens, A. G. G. M. 1994, ApJ, 428, 209, doi: [10.1086/174232](https://doi.org/10.1086/174232)
- Ohishi, M., Kaifu, N., Suzuki, H., & Morimoto, M. 1986, Ap&SS, 118, 405, doi: [10.1007/BF00651157](https://doi.org/10.1007/BF00651157)
- Pagani, L., Favre, C., Goldsmith, P. F., et al. 2017, A&A, 604, A32, doi: [10.1051/0004-6361/201730466](https://doi.org/10.1051/0004-6361/201730466)
- Pardo, J. R., Bermúdez, C., Cabezas, C., et al. 2020, A&A, 640, L13, doi: [10.1051/0004-6361/202038571](https://doi.org/10.1051/0004-6361/202038571)
- Pickett, H. M., Poynter, R. L., Cohen, E. A., et al. 1998, JQSRT, 60, 883, doi: [10.1016/S0022-4073\(98\)00091-0](https://doi.org/10.1016/S0022-4073(98)00091-0)
- Qin, S.-L., Liu, T., Liu, X., et al. 2022, MNRAS, 511, 3463, doi: [10.1093/mnras/stac219](https://doi.org/10.1093/mnras/stac219)
- Rizzo, J. R., Tercero, B., & Cernicharo, J. 2017, A&A, 605, A76, doi: [10.1051/0004-6361/201629936](https://doi.org/10.1051/0004-6361/201629936)
- Schilke, P., Benford, D. J., Hunter, T. R., Lis, D. C., & Phillips, T. G. 2001, The Astrophysical Journal Supplement Series, 132, 281, doi: [10.1086/318951](https://doi.org/10.1086/318951)
- Schilke, P., Groesbeck, T. D., Blake, G. A., Phillips, & T. G. 1997, ApJS, 108, 301, doi: [10.1086/312948](https://doi.org/10.1086/312948)
- Shimajiri, Y., Kitamura, Y., Saito, M., et al. 2014, A&A, 564, A68, doi: [10.1051/0004-6361/201322912](https://doi.org/10.1051/0004-6361/201322912)
- Tahani, K., Plume, R., Bergin, E. A., et al. 2016, ApJ, 832, 12, doi: [10.3847/0004-637X/832/1/12](https://doi.org/10.3847/0004-637X/832/1/12)
- Tercero, B., Cernicharo, J., Pardo, J. R., & Goicoechea, J. R. 2010, A&A, 517, A96, doi: [10.1051/0004-6361/200913501](https://doi.org/10.1051/0004-6361/200913501)
- Tercero, B., Vincent, L., Cernicharo, J., Viti, S., & Marcelino, N. 2011, A&A, 528, A26, doi: [10.1051/0004-6361/201015837](https://doi.org/10.1051/0004-6361/201015837)
- Terzian, Y. 1980, in Astrophysics and Space Science Library, Vol. 80, Radio Recombination Lines, ed. P. A. Shaver, 75–80, doi: [10.1007/978-94-009-9024-1_7](https://doi.org/10.1007/978-94-009-9024-1_7)
- Thelen, A. E., Cordner, M., Nixon, C., et al. 2020, in AAS/Division for Planetary Sciences Meeting Abstracts, Vol. 52, AAS/Division for Planetary Sciences Meeting Abstracts, 414.02

- Tiesinga, E., Mohr, P. J., Newell, D. B., & Taylor, B. N. 2021, *Reviews of Modern Physics*, 93, 025010, doi: [10.1103/RevModPhys.93.025010](https://doi.org/10.1103/RevModPhys.93.025010)
- Towle, J. P., Feldman, P. A., & Watson, J. K. G. 1996, *ApJS*, 107, 747, doi: [10.1086/192380](https://doi.org/10.1086/192380)
- Turner, B. E. 1989, *ApJS*, 70, 539, doi: [10.1086/191348](https://doi.org/10.1086/191348)
- Vallee, J. P., Guilloteau, S., Forveille, T., & Omont, A. 1990, *A&A*, 230, 457
- Vanelli-Coralli, A., Guidotti, A., Tarchi, D., et al. 2015, in *Cooperative and Cognitive Satellite Systems*, ed. S. Chatzinotas, B. Ottersten, & R. De Gaudenzi (Academic Press), 303–336, doi: <https://doi.org/10.1016/B978-0-12-799948-7.00010-4>
- Wang, J., Yu, L., Zhao, R., et al. 2017a, *Scientia Sinica Physica, Mechanica & Astronomica*, 47, 129504, doi: [10.1360/SSPMA2017-00077](https://doi.org/10.1360/SSPMA2017-00077)
- Wang, J. Q., Yu, L. F., Jiang, Y. B., et al. 2017b, *Acta Astronomica Sinica*, 58, 37
- Wang, S., Bergin, E. A., Crockett, N. R., et al. 2011, *A&A*, 527, A95, doi: [10.1051/0004-6361/201015079](https://doi.org/10.1051/0004-6361/201015079)
- White, G. J., Araki, M., Greaves, J. S., Ohishi, M., & Higginbottom, N. S. 2003, *A&A*, 407, 589, doi: [10.1051/0004-6361:20030841](https://doi.org/10.1051/0004-6361:20030841)
- Williams, J. P., de Geus, E. J., & Blitz, L. 1994, *ApJ*, 428, 693, doi: [10.1086/174279](https://doi.org/10.1086/174279)
- Wilson, T. L. 1999, *Reports on Progress in Physics*, 62, 143, doi: [10.1088/0034-4885/62/2/002](https://doi.org/10.1088/0034-4885/62/2/002)
- Wilson, T. L., Filges, L., Codella, C., Reich, W., & Reich, P. 1997, *A&A*, 327, 1177
- Wilson, T. L., & Rood, R. 1994, *ARA&A*, 32, 191, doi: [10.1146/annurev.aa.32.090194.001203](https://doi.org/10.1146/annurev.aa.32.090194.001203)
- Wilson, T. L., Zeng, Q., Huettemeister, S., & Dahmen, G. 1996, *A&A*, 307, 209
- Wu, Y., Liu, T., & Qin, S.-L. 2014, *ApJ*, 791, 123, doi: [10.1088/0004-637X/791/2/123](https://doi.org/10.1088/0004-637X/791/2/123)
- Wu, Y., Liu, X., Chen, X., et al. 2019, *MNRAS*, 488, 495, doi: [10.1093/mnras/stz1498](https://doi.org/10.1093/mnras/stz1498)
- Yusef-Zadeh, F. 1990, *ApJL*, 361, L19, doi: [10.1086/185817](https://doi.org/10.1086/185817)

APPENDIX

A. THE ABSORPTION OSCILLATOR STRENGTH OF RRLS

For hydrogenic RRL emitters, the absorption oscillator strength, f_{n_1,n_2} , is independent of Z ignoring the effect of the slightly different reduced mass of electron (Kardashev 1959; Goldwire & Goss 1967). Menzel (1968) gave a useful approximation for the oscillator strength f_{n_1,n_2}^* for RRLs:

$$f_{n_1,n_2}^* \sim n_1 M_{\Delta n} \left(1 + 1.5 \frac{\Delta n}{n_1} \right) \quad (\text{A1})$$

In Liu et al. (2022), we empirically fitted the values of $M_{\Delta n}$ tabulated in Menzel (1968) as

$$M_{\Delta n} \sim 0.1905 (1/\Delta n)^{2.887} \quad (\text{A2})$$

Actually, the oscillator strength can be accurately calculated through the Gordon formula (Gordon 1929). Following the Eqs. (3.1)–(3.7) of Brocklehurst (1971), we numerically tabulated the precise oscillator strength (denoted as f_{n_1,n_2}^\dagger)⁵. The $\log_{10}(f_{n_1,n_2}^\dagger)$ and $f_{n_1,n_2}^\dagger / f_{n_1,n_2}^*$ are shown in Figure 14. The f_{n_1,n_2}^* deviates from f_{n_1,n_2}^\dagger by less than 20 percent when $\Delta n < 5$.

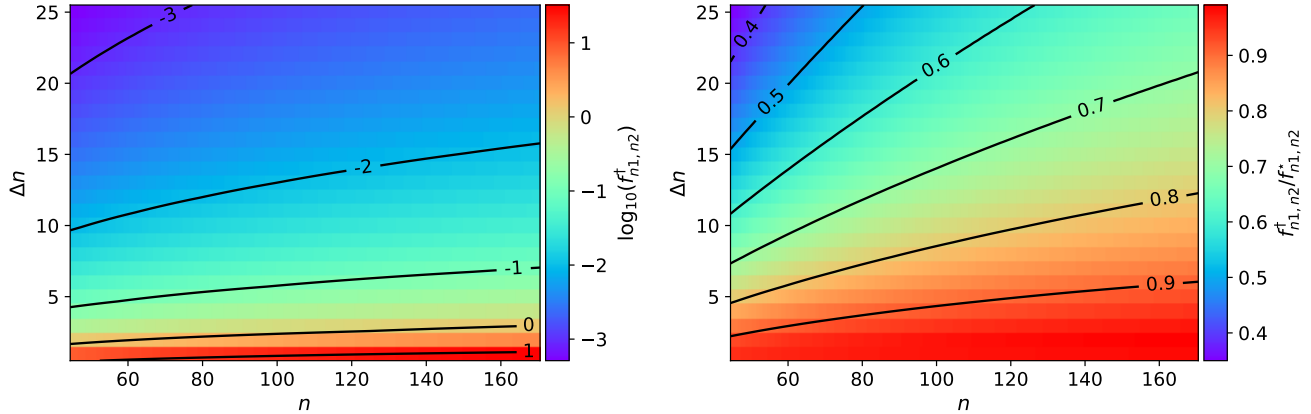


Figure 14. The $\log_{10}(f_{n_1,n_2}^\dagger)$ (left) and $f_{n_1,n_2}^\dagger / f_{n_1,n_2}^*$ (right) for RRLs with different n and Δn .

⁵ <https://gitee.com/liuxunchuan/tmrtsurvey/blob/master/fnlIn2.py>

B. THE α LINES OF X^+ RRLS IN K BAND BY EFFELSBERG

Figure 15 shows the α lines of ion RRLs from the archive data of the K-band survey of Orion KL by the Effelsberg 100 telescope (Gong et al. 2015). To exclude blending, we first modeled the K-band spectrum of Orion-KL. The RRLs are modeled using the parameters (EM , ΔV , and V_{LSR}) of this work. All molecular species detected in K band (Gong et al. 2015) can be detected in Q band (Liu et al. 2022) and Ka band (this work). Thus, to model the emission of molecular species, the parameters (N , ΔV , V_{LSR} and T_{ex}) obtained based on the Q-band and Ka-band data are used with no modification. Fortunately, most of the K-band α lines of ion RRLs are not blended (Figure 15).

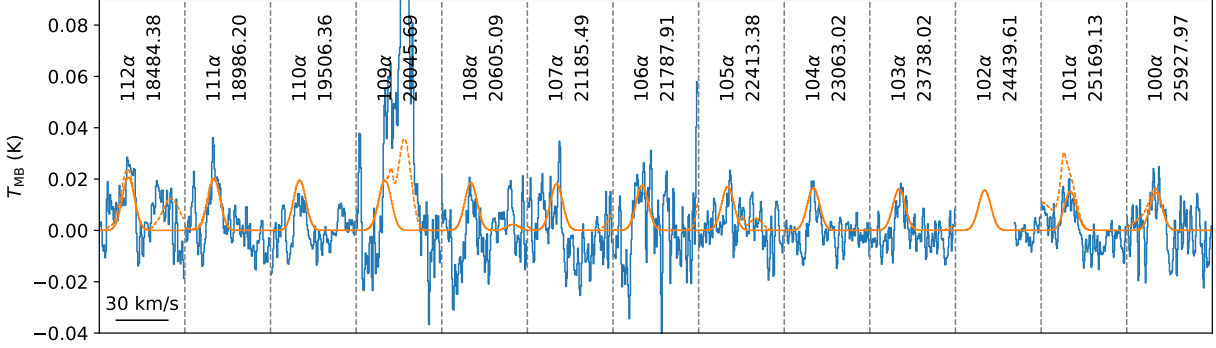
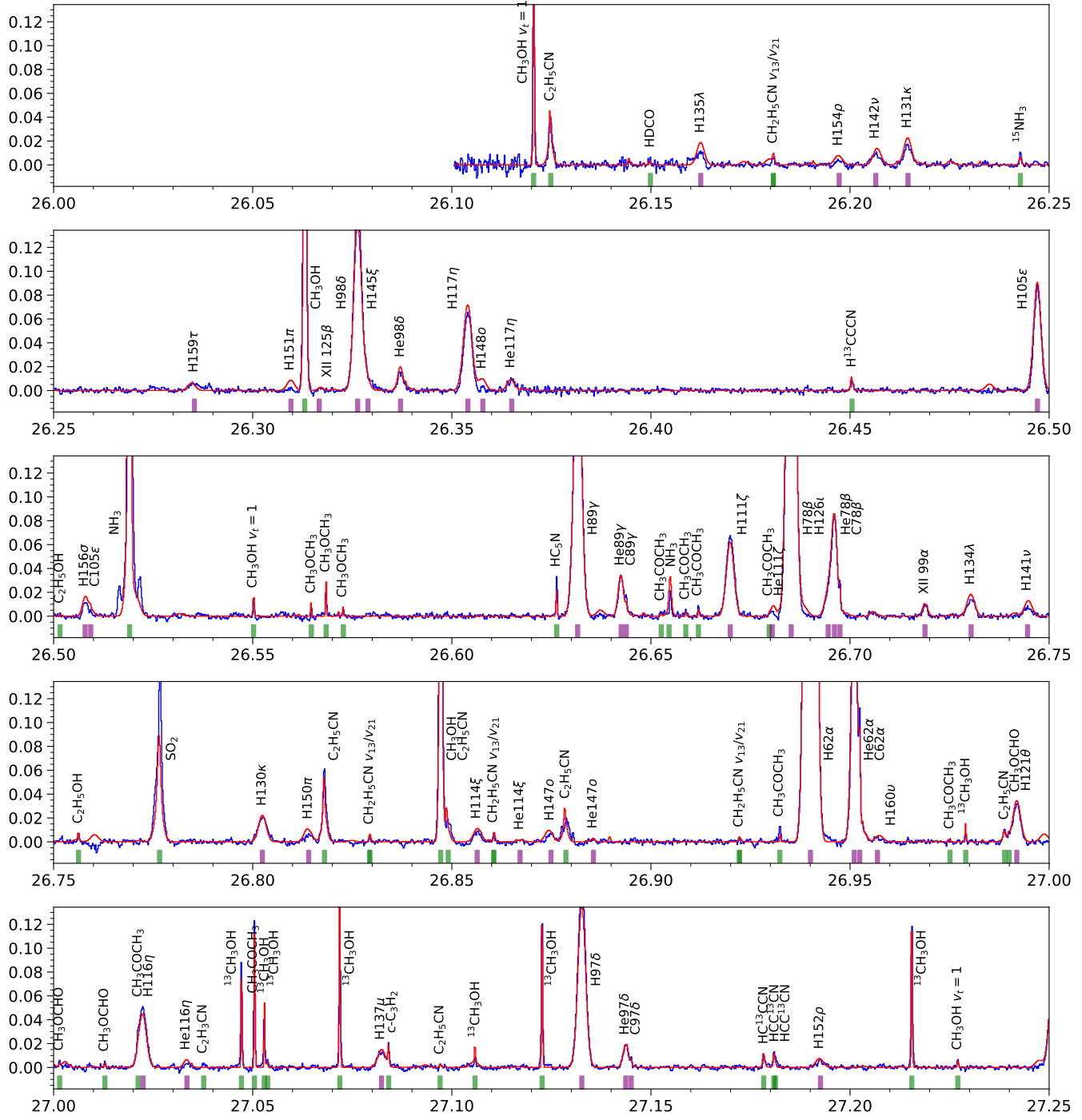
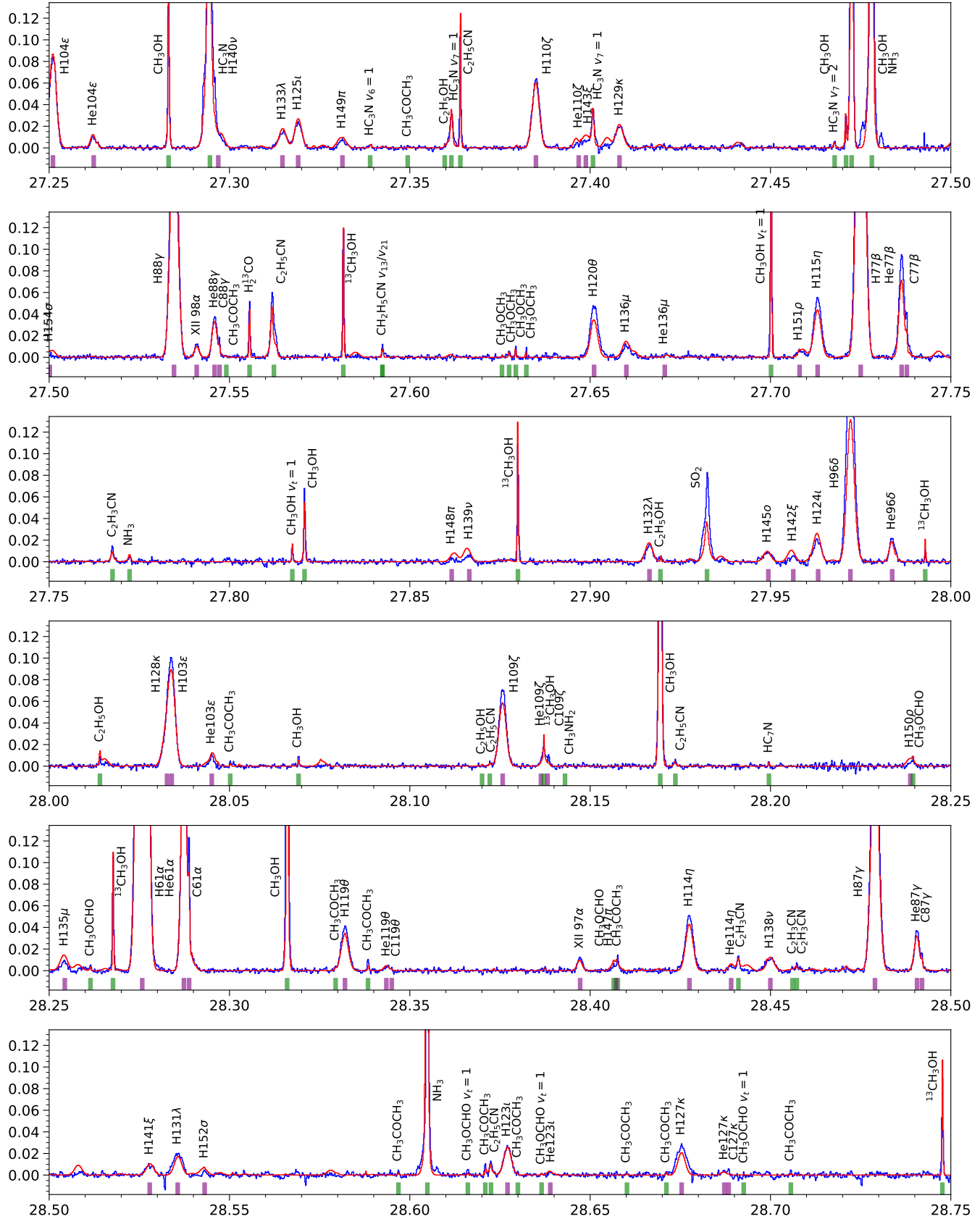


Figure 15. The K-band α lines of ion RRLs (blue) from the archive data of Effelsberg (Gong et al. 2015). The orange lines are the modeled spectrum. The orange dashed line takes all species into account, and the orange solid line only considers the ion RRLs.

Figure 16. The Orion KL spectrum

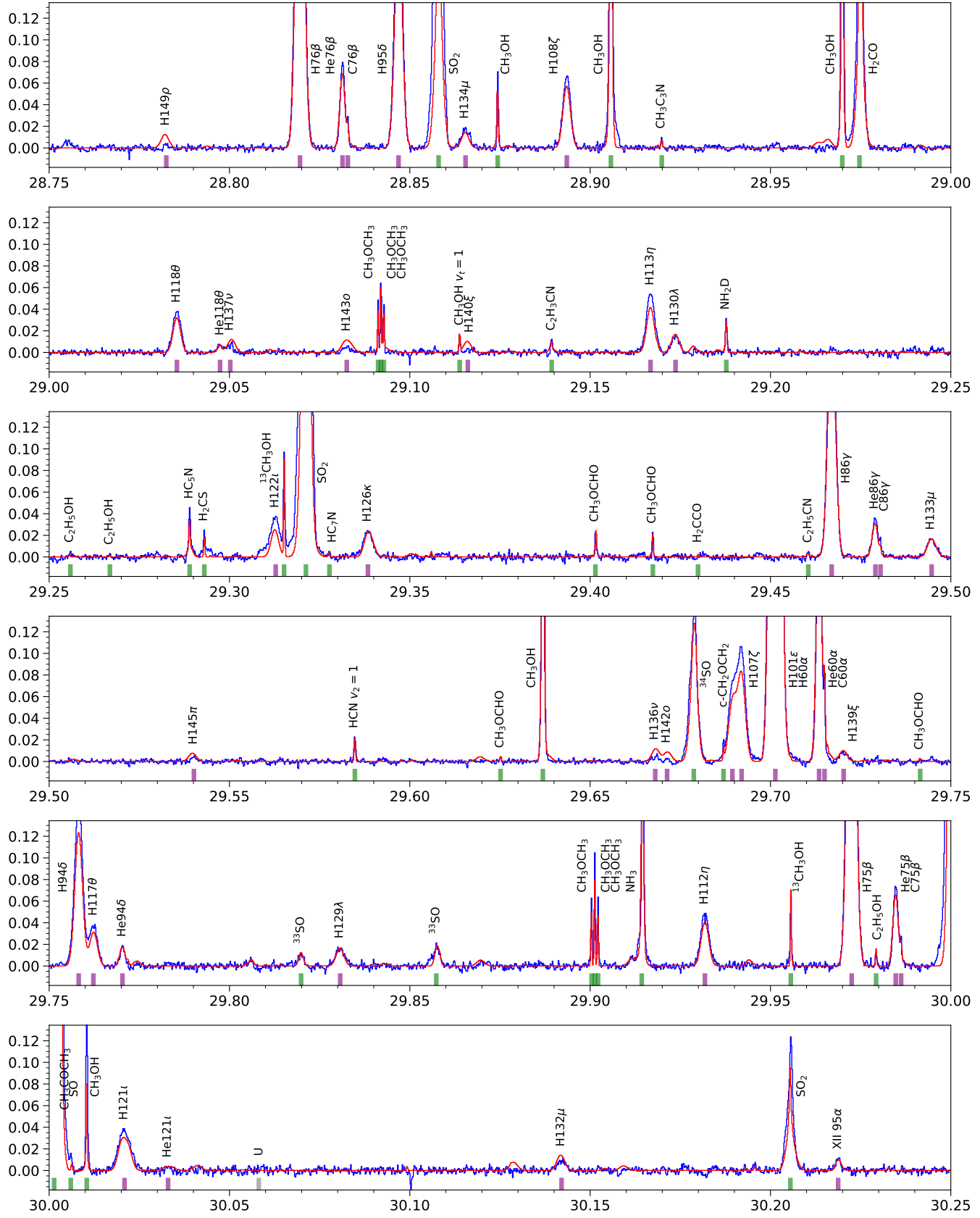
Note: The blue line is the Orion KL spectrum observed by the TMRT 65 m, which has been smoothed to have a frequency resolution of 183 kHz ($\sim 1.8 \text{ km s}^{-1}$ at 30 GHz). The red line represents the modeling fitting. The purple strips denote the detected RRLs. The green strips denote the molecular lines. The gray strips mark the U lines.

Figure 16 (continued)



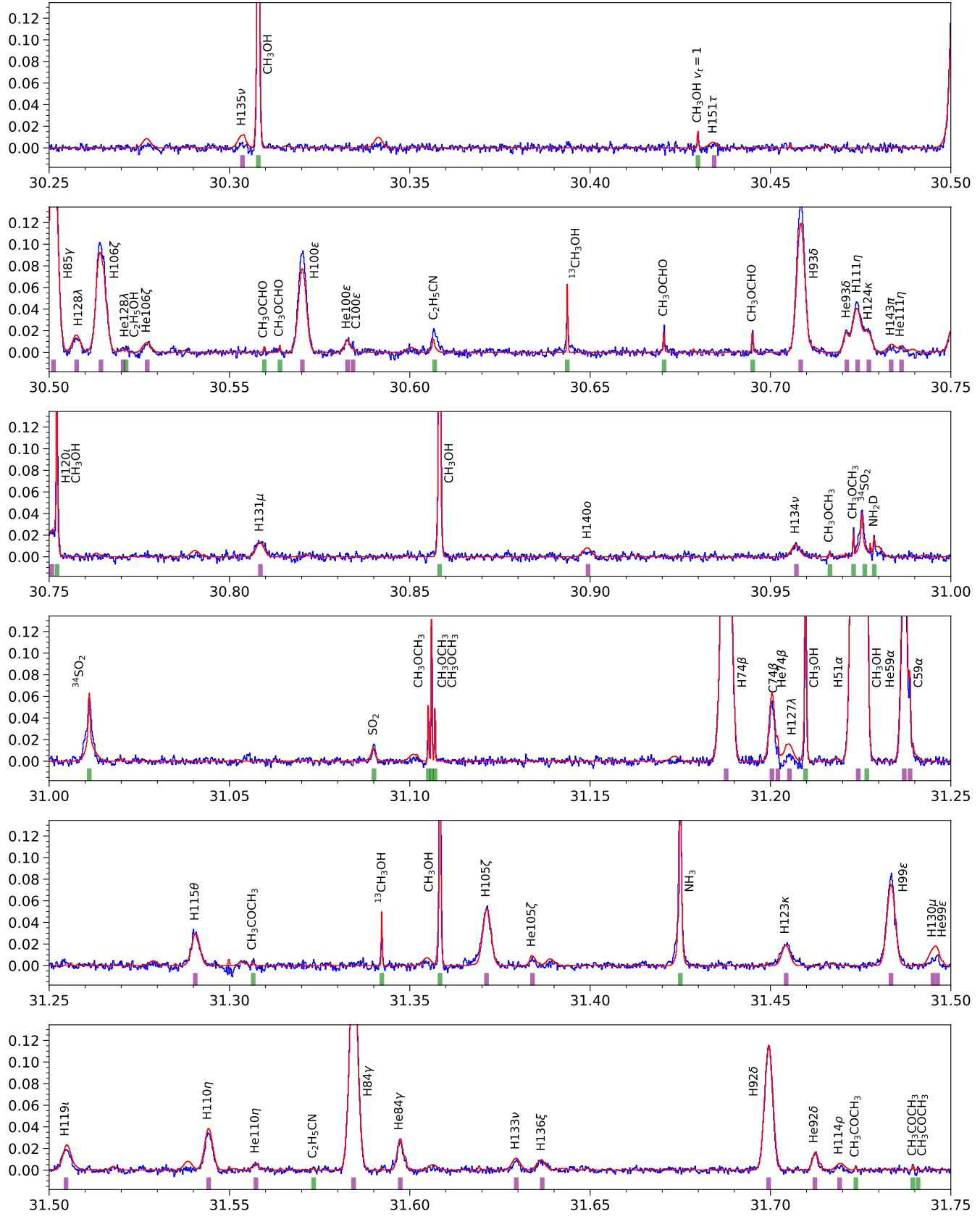
Note: The blue line is the Orion KL spectrum observed by the TMRT 65 m, which has been smoothed to have a frequency resolution of 183 kHz (\sim 1.8 km s $^{-1}$ at 30 GHz). The red line represents the modeling fitting. The purple strips denote the detected RRLs. The green strips denote the molecular lines. The gray strips mark the U lines.

Figure 16 (continued)



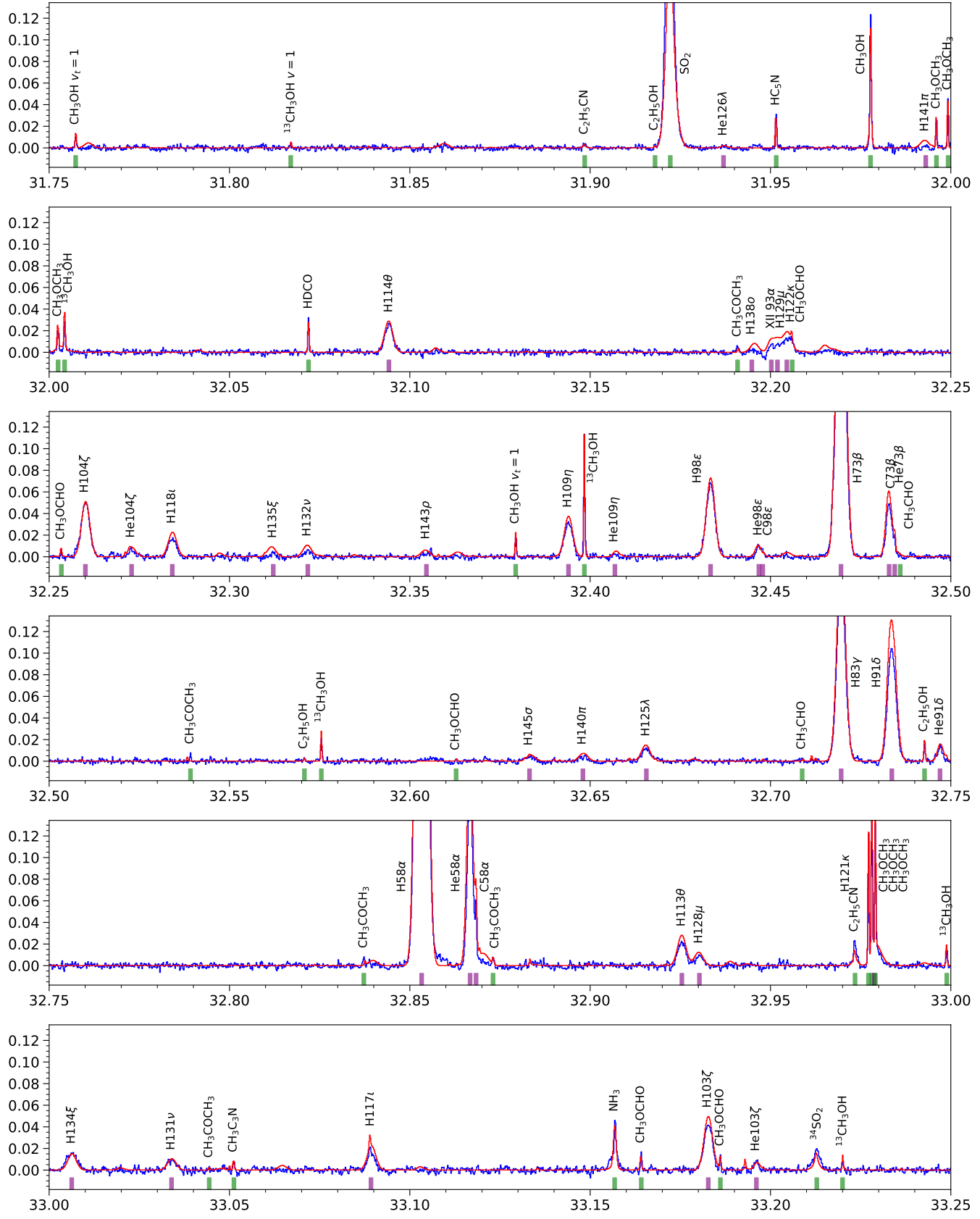
Note: The blue line is the Orion KL spectrum observed by the TMRT 65 m, which has been smoothed to have a frequency resolution of 183 kHz ($\sim 1.8 \text{ km s}^{-1}$ at 30 GHz). The red line represents the modeling fitting. The purple strips denote the detected RRLs. The green strips denote the molecular lines. The gray strips mark the U lines.

Figure 16 (continued)



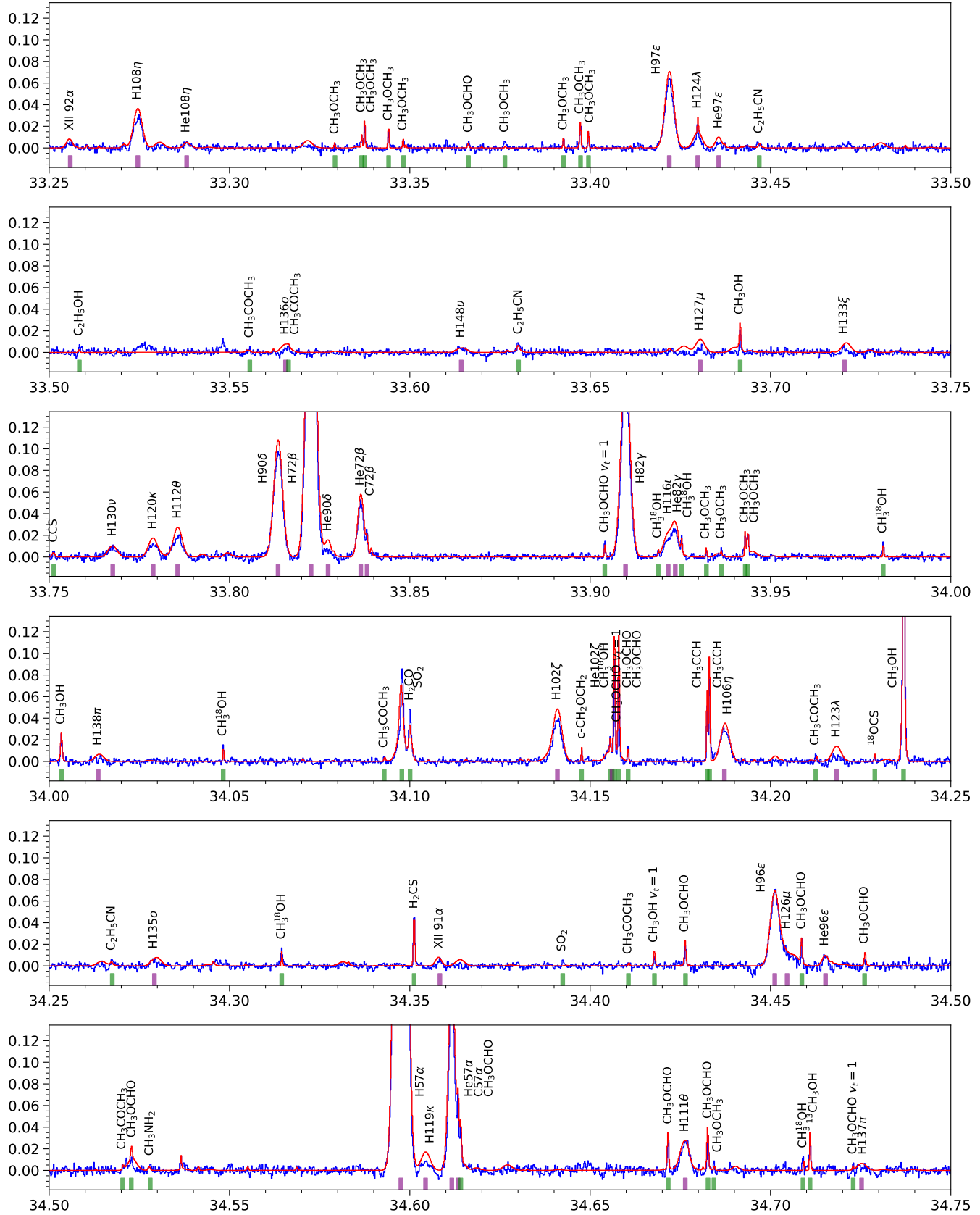
Note: The blue line is the Orion KL spectrum observed by the TMRT 65 m, which has been smoothed to have a frequency resolution of 183 kHz ($\sim 1.8 \text{ km s}^{-1}$ at 30 GHz). The red line represents the modeling fitting. The purple strips denote the detected RRLs. The green strips denote the molecular lines. The gray strips mark the U lines.

Figure 16 (continued)



Note: The blue line is the Orion KL spectrum observed by the TMRT 65 m, which has been smoothed to have a frequency resolution of 183 kHz ($\sim 1.8 \text{ km s}^{-1}$ at 30 GHz). The red line represents the modeling fitting. The purple strips denote the detected RRLs. The green strips denote the molecular lines. The gray strips mark the U lines.

Figure 16 (continued)



Note: The blue line is the Orion KL spectrum observed by the TMRT 65 m, which has been smoothed to have a frequency resolution of 183 kHz (\sim 1.8 km s $^{-1}$ at 30 GHz). The red line represents the modeling fitting. The purple strips denote the detected RRLs. The green strips denote the molecular lines. The gray strips mark the U lines.

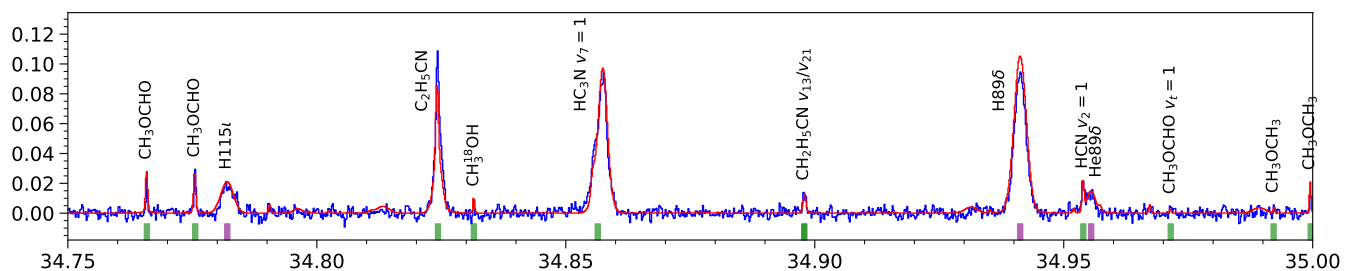
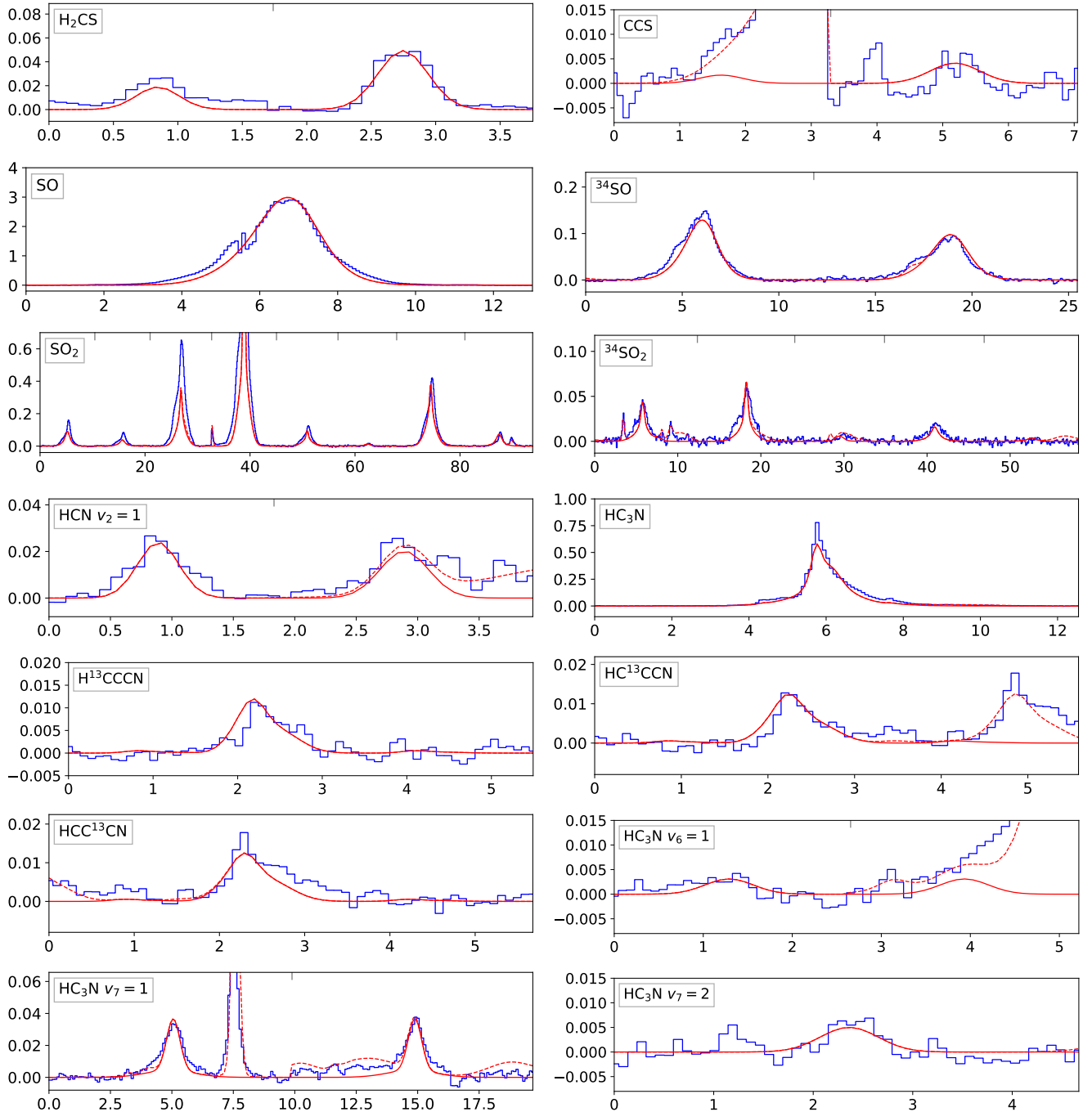
Figure 16 (continued)**Figure 16 continued**

Figure 17. Model fitting for different species.

Note: In each panel, the spectra between two neighbouring upper ticks are independent frequency segments containing transitions of the corresponding species. The x axis is in unit of MHz. The y axis is T_{MB} in unit of K. See Figure 10 for the spliced spectra of methanol.

Figure 17 continued

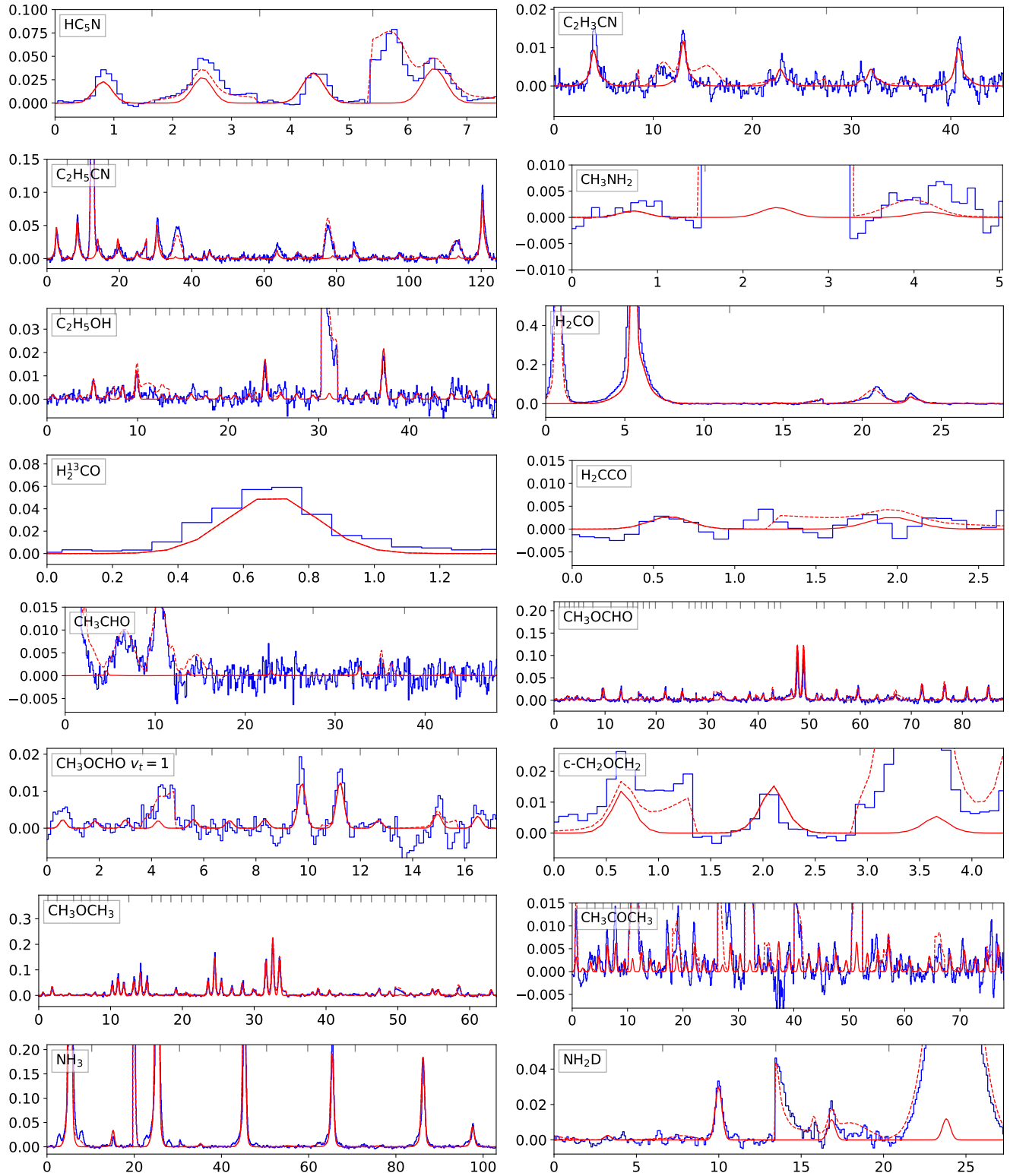
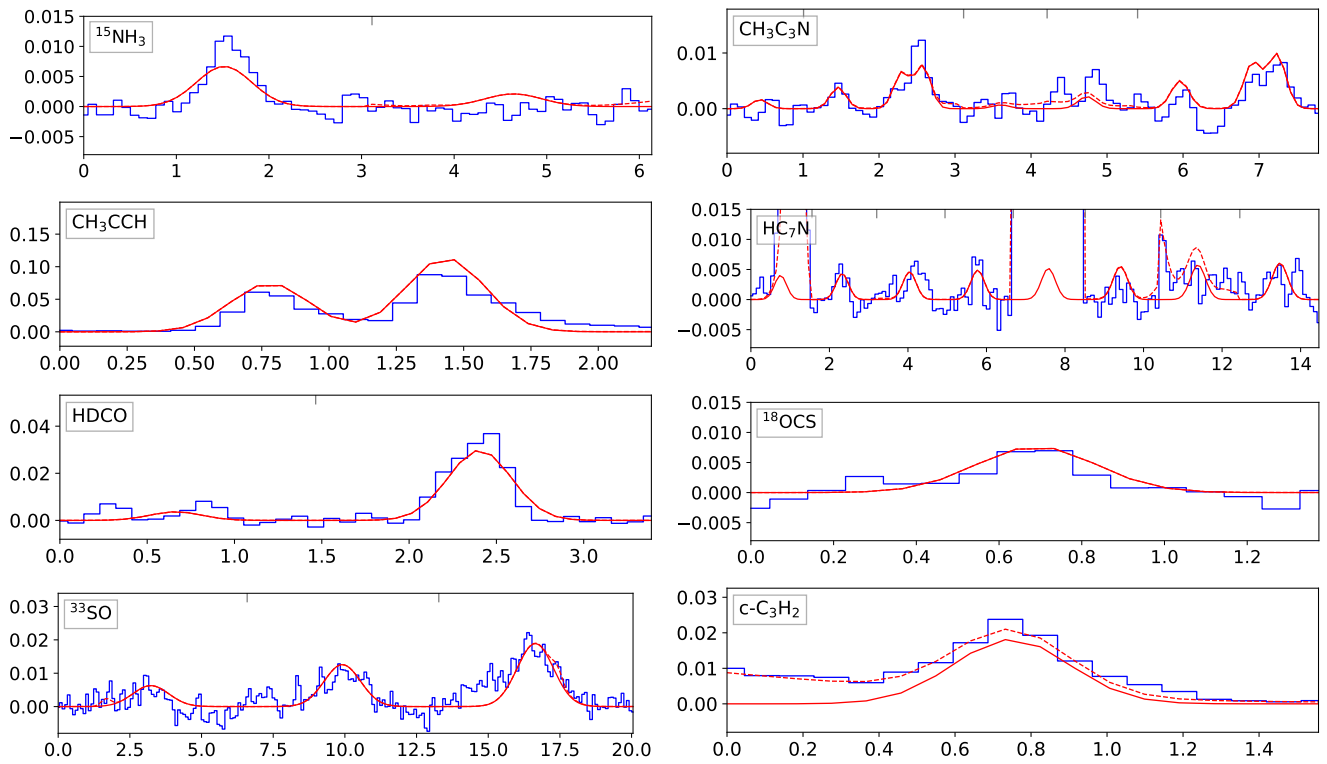
Figure 17 (continued)**Figure 17 continued**

Figure 17 (continued)**Figure 17 continued**

C. LINE LIST OF MOLECULAR LINES

Table 6 shows the results of identification and Gaussian fitting of molecular lines, including RRLs which are blended with molecular lines. The unblended RRLs are listed in Table 7.

Table Notes:

- (1) Doppler correction has been applied to f_{obs} assuming a source velocity of 6 km s⁻¹ in LSR (Sect. 3.1).
Rows with empty f_{obs} correspond to blended lines.
- (2) The emitter of ion RRL is denoted as X II, and the f_{rest} is adopted as the rest frequency of the corresponding C II RRL.
The unidentified species is denoted as U.
- (3) Rows with a same species name and transition label correspond to different emission components of a same transition.
The transition labels for HCN $v_t = 1$ are J^P with p the parity.
The transition labels for CH₃OCH₃ are J_K^s with s the symmetry substate.
The transition labels are (J, K) for NH₃ convention lines.
- (4) The numbers in brackets in the 7th and 8th columns represent the uncertainties of the **last digital** of corresponding parameters.

Table 6. Linelist

f_{obs} (MHz)	Species	f_{rest} (MHz)	Transition	E_u (K)	A_{ij} (10 ⁻⁶ s ⁻¹)	$\int T_{\text{MB}} \text{d}V$ (K km s ⁻¹)	ΔV (km s ⁻¹)	$T_{\text{MB}}^{\text{peak}}$ K	V_{LSR} km s ⁻¹
26120.55	CH ₃ OH $v_t = 1$	26120.584	10 _{1,9} – 11 _{2,9}	452.7	0.06	0.879(9)	4(1)	1.93E–01	6.4(1)
26124.84	C ₂ H ₅ CN	26124.592	3 _{1,3} – 2 _{1,2}	3.6	1.17	0.507(9)	13(1)	3.72E–02	3(1)
26149.88	HDCO	26150.160	8 _{2,6} – 8 _{2,7}	144.3	0.06	0.021(2)	2(1)	8.16E–03	9(1)
26180.75	C ₂ H ₅ CN $v13/v21$	26180.635		299.8	0.06	0.049(9)	8(1)	5.95E–03	5(1)
26242.78	¹⁵ NH ₃	26242.760	$J_K = 9_9 - 9_9$	852.5	0.4	0.078(9)	6(1)	1.18E–02	6(1)
26289.13	U					0.050(2)	8(1)	5.60E–03	
26313.06	E-CH ₃ OH	26313.192	11 _{2,10} – 11 _{1,10}	175.5	0.1	9.09(2)	6.4(1)	1.33E+00	7.5(1)
26450.51	H ¹³ CCCN	26450.596	$J = 3 - 2$	2.5	1.28	0.088(7)	8.8(9)	9.47E–03	7.0(3)
26501.59	C ₂ H ₅ OH	26501.778	4 _{1,3} – 4 _{2,3}	71.3	0.06	0.009(2)	1.3(6)	7.07E–03	8.1(1)
26516.55	NH ₃	26518.981	(8 _{8,8} , 8 ₈)	686.8	0.4	0.291(6)	10.5(2)	2.59E–02	33.5(2)
26519.11	NH ₃	26518.981	(8 _{8,8} , 8 ₈)	686.8	0.4	8.05(1)	9.1(1)	8.33E–01	4.5(1)
26521.59	NH ₃	26518.981	(8 _{8,8} , 8 ₈)	686.8	0.4	0.40(1)	12.1(3)	3.13E–02	-23.5(1)
26550.22	CH ₃ OH $v_t = 1$	26550.263	10 _{9,2} – 10 _{8,2}	811.0	0.03	0.051(5)	3.1(3)	1.56E–02	6.5(1)
26564.72	CH ₃ OCH ₃	26564.800	12 _{3,9} ⁰ – 11 _{4,8} ⁰	83.9	0.02	0.024(4)	2.2(4)	1.03E–02	6.9(1)
26568.43	CH ₃ OCH ₃	26568.544	12 _{3,9} ¹ – 11 _{4,8} ¹	83.9	0.02	0.103(5)	3.1(2)	3.14E–02	7.3(1)
26572.76	CH ₃ OCH ₃	26572.820	12 _{3,9} ¹² – 11 _{4,8} ¹²	83.9	0.02	0.035(5)	3.5(6)	9.48E–03	6.6(1)
26626.35	HC ₅ N	26626.463	$J = 10 - 9$	7.0	1.96	0.124(5)	3.7(2)	3.15E–02	7.2(1)
26652.59	AE-CH ₃ COCH ₃	26652.524	11 _{7,4} – 11 _{6,5}	54.3	0.7	0.009(2)	4(2)	2.35E–03	5(1)
26654.18	NH ₃	26654.847	(13 _{12,13} ₁₂)	1826.0	0.4	0.237(6)	31(1)	7.12E–03	14(1)
26654.93	NH ₃	26654.847	(13 _{12,13} ₁₂)	1826.0	0.4	0.094(6)	4(1)	2.01E–02	5(1)
26658.75	AA-CH ₃ COCH ₃	26658.734	11 _{7,4} – 11 _{6,5}	54.1	0.7	0.023(6)	3(1)	6.28E–03	6(1)
26661.94	EE-CH ₃ COCH ₃	26661.943	11 _{7,4} – 11 _{6,5}	54.2	0.7	0.056(5)	5.0(5)	1.06E–02	6.1(2)
26679.70	EA-CH ₃ COCH ₃	26679.716	11 _{7,4} – 11 _{6,5}	54.3	0.7	0.021(6)	4(2)	4.81E–03	6.2(8)
26756.26	C ₂ H ₅ OH	26756.342	1 _{1,0} – 1 _{0,1}	2.1	0.2	0.048(2)	4(1)	1.07E–02	7(1)
26776.61	SO ₂	26776.574	25 _{4,22} – 24 _{5,19}	339.0	0.04	2.25(1)	16.3(1)	1.30E–01	5.6(1)
26818.02	C ₂ H ₅ CN	26817.814	3 _{0,3} – 2 _{0,2}	2.6	1.43	0.68(1)	11(1)	5.57E–02	4(1)
26829.40	C ₂ H ₅ CN $v13/v21$	26829.333		307.8	1.43	0.037(8)	6(2)	5.37E–03	5.3(5)
26847.20	E-CH ₃ OH	26847.237	12 _{2,11} – 12 _{1,11}	203.4	0.1	26.6(1)	2.0(1)	1.24E+01	6.4(1)
26849.09	C ₂ H ₅ CN	26848.630	3 _{2,2} – 2 _{2,1}	7.0	0.8	0.37(2)	19(1)	1.84E–02	0.8(5)

Table 6 *continued*

Table 6 (*continued*)

f_{obs}	Species	f_{rest}	Transition	E_u	A_{ij}	$\int T_{\text{MB}} \text{d}V$	ΔV	$T_{\text{MB}}^{\text{peak}}$	V_{LSR}
(MHz)		(MHz)		(K)	(10^{-6} s^{-1})	(K km s $^{-1}$)	(km s $^{-1}$)	K	km s $^{-1}$
26860.54	C ₂ H ₅ CN $v13/v21$	26860.453		298.9	0.8	0.023(4)	2.6(5)	8.53E-03	5.0(2)
26878.65	C ₂ H ₅ CN	26878.303	3 _{2,1} – 2 _{2,0}	7.0	0.8	0.42(1)	23.4(9)	1.71E-02	2.2(4)
26880.43	U					0.036(7)	3.6(7)	9.41E-03	
26922.22	C ₂ H ₅ CN $v13/v21$	26922.076		302.9	0.8	0.014(3)	2.5(7)	5.17E-03	4.4(3)
26932.38	EE-CH ₃ COCH ₃	26932.441	12 _{8,4} – 12 _{7,5}	64.5	0.8	0.094(4)	6.2(4)	1.43E-02	6.7(2)
26975.10	AA-CH ₃ COCH ₃	26974.959	12 _{8,4} – 12 _{7,5}	64.4	0.8	0.024(6)	6(3)	3.76E-03	4(2)
26979.06	¹³ CH ₃ OH	26979.070	12 _{4,9} – 13 _{3,10}	257.4	0.03	0.019(5)	3(1)	6.29E-03	6(1)
26988.82	C ₂ H ₅ CN	26988.679	5 _{1,4} – 5 _{0,5}	7.7	0.2	0.11(3)	9(4)	1.16E-02	4(3)
26989.98	A-CH ₃ OCHO	26989.976	7 _{2,5} – 6 _{3,4}	19.7	0.006	0.033(9)	5(1)	6.25E-03	6(1)
27001.51	A-CH ₃ OCHO	27001.548	18 _{10,9} – 19 _{9,10}	167.3	0.004	0.033(9)	4(1)	8.04E-03	6(1)
27012.87	E-CH ₃ OCHO	27012.953	7 _{2,5} – 6 _{3,4}	19.7	0.005	0.016(4)	3(1)	5.10E-03	7(1)
27021.22	AA-CH ₃ COCH ₃	27021.085	9 _{7,2} – 9 _{6,3}	38.5	0.6	0.1633(2)	11.0(6)	1.40E-02	4.5(1)
27037.69	C ₂ H ₃ CN	27037.600	21 _{2,19} – 21 _{2,20}	114.9	0.03	0.04(1)	10(4)	4.20E-03	5(2)
27047.17	¹³ CH ₃ OH	27047.280	3 _{2,1} – 3 _{1,2}	35.9	0.09	0.37(1)	3(1)	1.04E-01	7(1)
27050.43	¹³ CH ₃ OH	27050.540	4 _{2,2} – 4 _{1,3}	45.0	0.1	0.47(1)	3(1)	1.40E-01	7(1)
27052.89	¹³ CH ₃ OH	27053.030	2 _{2,0} – 2 _{1,1}	29.2	0.07	0.18(1)	3(1)	5.37E-02	8(1)
27053.76	EE-CH ₃ COCH ₃	27053.621	9 _{7,2} – 9 _{6,3}	38.6	0.5	0.029(8)	5(1)	4.98E-03	4(1)
27071.87	¹³ CH ₃ OH	27071.930	5 _{2,3} – 5 _{1,4}	56.3	0.1	0.582(5)	3.4(1)	1.60E-01	6.6(1)
27084.14	c-C ₃ H ₂	27084.352	3 _{3,0} – 3 _{2,1}	19.5	1.0	0.077(8)	4.0(4)	1.82E-02	8.3(1)
27097.05	C ₂ H ₅ CN	27097.100	26 _{4,23} – 25 _{5,20}	169.0	0.03	0.015(4)	4(2)	3.44E-03	6.5(8)
27105.83	¹³ CH ₃ OH	27105.870	12 _{4,8} – 13 _{3,11}	257.4	0.03	0.042(7)	5(1)	7.32E-03	6.4(1)
27122.67	¹³ CH ₃ OH	27122.720	6 _{2,4} – 6 _{1,5}	69.9	0.1	0.554(5)	3.3(1)	1.60E-01	6.6(1)
27178.34	HC ¹³ CCN	27178.505	$J = 3 - 2$	2.6	1.39	0.056(5)	4.2(5)	1.23E-02	7.9(1)
27180.87	HCC ¹³ CN	27180.885	$J = 3 - 2$	2.6	1.17	0.031(7)	2.5(4)	1.17E-02	6.1(1)
27181.27	HCC ¹³ CN	27181.151	$J = 3 - 2$	2.6	1.23	0.11(1)	11(1)	8.92E-03	4.7(6)
27215.52	¹³ CH ₃ OH	27215.570	7 _{2,5} – 7 _{1,6}	85.8	0.1	0.537(4)	3.5(1)	1.44E-01	6.6(1)
27227.06	CH ₃ OH $v_t = 1$	27227.113	6 _{3,3} – 7 _{2,5}	466.0	0.004	0.032(5)	4.2(8)	7.15E-03	6.6(3)
27283.11	E-CH ₃ OH	27283.140	14 _{5,10} – 15 _{4,12}	367.6	0.03	0.83(4)	4.5(3)	1.73E-01	6.3(1)
27292.95	HC ₃ N	27294.289	$J = 3 - 2$	2.6	1.41	0.68(2)	11(1)	5.88E-02	21(1)
27294.20	HC ₃ N	27294.289	$J = 3 - 2$	2.6	1.41	6.08(7)	11.0(2)	5.20E-01	7.0(1)
27295.12	HC ₃ N	27294.289	$J = 3 - 2$	2.6	1.41	1.33(2)	13(1)	9.60E-02	-3(1)
27296.05	HC ₃ N	27294.289	$J = 3 - 2$	2.6	1.41	0.20(2)	6(1)	3.05E-02	-13(1)
27296.90	H140 ν	27296.730				0.30(2)	18(1)	1.59E-02	4(1)
	HC ₃ N	27296.233	$J = 3 - 2$	2.6	0.07				-1(1)
27339.00	HC ₃ N $v_6 = 1$	27339.150	$J = 3 - 2$	720.3	1.26	0.028(5)	9(1)	3.07E-03	8(1)
27349.42	EA-CH ₃ COCH ₃	27349.349	9 _{7,2} – 9 _{6,3}	38.7	0.5	0.014(3)	3(1)	4.09E-03	5(1)
27359.68	C ₂ H ₅ OH	27359.801	6 _{3,4} – 6 _{2,4}	85.3	0.06	0.009(2)	1.7(6)	4.66E-03	7.3(3)
27361.45	HC ₃ N $v_7 = 1$	27361.410	$J = 3 - 2$	323.5	1.26	0.30(2)	21(2)	1.33E-02	5.6(5)
27361.59	HC ₃ N $v_7 = 1$	27361.410	$J = 3 - 2$	323.5	1.26	0.16(2)	7.6(6)	1.97E-02	4.0(2)
27364.01	C ₂ H ₅ CN	27363.777	9 _{3,6} – 10 _{2,9}	29.4	0.03	0.541(4)	3.5(1)	1.45E-01	3.4(1)

Table 6 *continued*

Table 6 (continued)

f_{obs} (MHz)	Species	f_{rest} (MHz)	Transition J_{K_a,K_c}	E_u (K)	A_{ij} (10^{-6} s^{-1})	$\int T_{\text{MB}} \text{d}V$ (K km s $^{-1}$)	ΔV (km s $^{-1}$)	$T_{\text{MB}}^{\text{peak}}$ K	V_{LSR} km s $^{-1}$
27390.72	U					0.025(6)	6(2)	3.75E-03	
27400.78	HC ₃ N $v_7 = 1$	27400.630	$J = 3 - 2$	323.5	1.26	0.45(1)	12(1)	3.37E-02	4(1)
27467.79	HC ₃ N $v_7 = 2$	27467.677	$J = 3 - 2$	644.3	1.43	0.035(5)	5.5(9)	5.96E-03	4.7(5)
27470.95	E-CH ₃ OH	27470.972	$25_{2,24} - 25_{1,24}$	776.2	0.05	0.155(4)	3.8(1)	3.84E-02	6.2(1)
27472.50	E-CH ₃ OH	27472.534	$13_{2,12} - 13_{1,12}$	233.6	0.1	25.5(1)	1.7(1)	1.41E+01	6.4(1)
27475.58	NH ₃	27477.943	(9 ₉ ,9 ₉)	852.8	0.5	0.34(1)	13.0(7)	2.46E-02	31.7(2)
27478.06	NH ₃	27477.943	(9 ₉ ,9 ₉)	852.8	0.5	7.55(3)	9.1(1)	7.81E-01	4.7(1)
27480.65	NH ₃	27477.943	(9 ₉ ,9 ₉)	852.8	0.5	0.159(8)	9.9(6)	1.51E-02	-23.6(2)
27549.13	EA-CH ₃ COCH ₃	27549.108	$6_{5,2} - 6_{4,3}$	18.3	0.4	0.013(3)	10(7)	1.25E-03	6(4)
27555.56	H ₂ ¹³ CO	27555.673	$3_{1,2} - 3_{1,3}$	32.9	0.1	0.26(1)	4(1)	5.65E-02	7(1)
27561.85	C ₂ H ₅ CN	27561.680	$3_{1,2} - 2_{1,1}$	3.8	1.38	0.58(1)	11(1)	5.08E-02	4(1)
27562.79	C ₂ H ₅ CN	27561.680	$3_{1,2} - 2_{1,1}$	3.8	1.38	0.20(1)	14(1)	1.30E-02	-6(1)
27581.55	¹³ CH ₃ OH	27581.630	$9_{2,7} - 9_{1,8}$	124.3	0.1	0.53(1)	3(1)	1.52E-01	6.8(1)
27592.40	C ₂ H ₅ CN $v13/v21$	27592.228		300.0	0.1	0.06(1)	4.8(9)	1.23E-02	4.1(9)
27593.23	U					0.05(1)	8.1(9)	5.40E-03	
27625.55	CH ₃ OCH ₃	27625.739	$2_{2,1}^{12} - 3_{1,2}^{12}$	8.4	0.01	0.010(2)	1.8(8)	5.28E-03	8.0(4)
27627.54	CH ₃ OCH ₃	27627.573	$2_{2,1}^{11} - 3_{1,2}^{11}$	8.4	0.02	0.031(6)	5(2)	5.51E-03	6.4(6)
27629.39	CH ₃ OCH ₃	27629.487	$2_{2,1}^1 - 3_{1,2}^1$	8.4	0.01	0.036(4)	2.7(4)	1.26E-02	7.0(2)
27632.31	CH ₃ OCH ₃	27632.353	$2_{2,1}^0 - 3_{1,2}^0$	8.4	0.01	0.023(3)	1.0(9)	2.14E-02	6.5(2)
27700.15	CH ₃ OH $v_t = 1$	27700.180	$12_{2,11} - 11_{1,11}$	479.2	0.07	0.9393(4)	4.4(1)	1.99E-01	6.3(1)
27767.58	C ₂ H ₃ CN	27767.351	$3_{1,3} - 2_{1,2}$	4.8	1.38	0.142(9)	9.9(7)	1.35E-02	3.5(2)
		27767.269							2.7(2)
27772.30	NH ₃	27772.294	(14 ₁₃ ,14 ₁₃)	2090.5	0.4	0.040(6)	7(1)	5.18E-03	5.9(4)
27817.42	CH ₃ OH $v_t = 1$	27817.439	$11_{9,3} - 11_{8,3}$	836.5	0.04	0.066(8)	4.2(9)	1.48E-02	6.2(9)
27820.81	E-CH ₃ OH	27820.841	$19_{5,14} - 18_{6,13}$	576.7	0.03	0.335(8)	4.4(9)	7.09E-02	6.3(9)
27879.98	¹³ CH ₃ OH	27880.030	$10_{2,8} - 10_{1,9}$	147.0	0.1	0.462(8)	3.4(9)	1.29E-01	6.6(9)
27919.48	C ₂ H ₅ OH	27919.726	$3_{0,3} - 2_{1,2}$	5.0	0.09	0.026(7)	10(3)	2.48E-03	9(2)
27932.26	SO ₂	27932.411	$25_{2,24} - 24_{3,21}$	303.7	0.02	1.02(1)	24.4(4)	3.92E-02	7.6(2)
27932.56	SO ₂	27932.411	$25_{2,24} - 24_{3,21}$	303.7	0.02	0.31(1)	6.6(2)	4.41E-02	4.4(1)
27992.91	¹³ CH ₃ OH	27992.990	$6_{2,5} - 5_{3,2}$	85.4	0.02	0.033(4)	2.3(3)	1.32E-02	6.9(1)
28014.07	C ₂ H ₅ OH	28014.169	$2_{1,1} - 2_{0,2}$	3.9	0.3	0.046(6)	4.0(7)	1.09E-02	7.0(2)
28050.20	EE-CH ₃ COCH ₃	28050.283	$6_{5,2} - 6_{4,3}$	18.2	0.5	0.021(4)	3.1(6)	6.49E-03	6.9(3)
28069.16	E-CH ₃ OH	28069.208	$16_{0,16} - 15_{3,13}$	327.6	0.0006	0.041(3)	2.7(2)	1.43E-02	6(1)
28120.03	C ₂ H ₅ OH	28120.258	$5_{3,3} - 5_{2,3}$	80.3	0.06	0.012(3)	2.8(9)	4.06E-03	8.4(4)
28122.17	C ₂ H ₅ CN	28122.144	$19_{5,14} - 20_{4,17}$	109.5	0.03	0.019(4)	2.1(5)	8.31E-03	5.7(1)
28137.17	¹³ CH ₃ OH	28137.250	$6_{2,4} - 5_{3,3}$	85.4	0.02	0.13(1)	6.8(9)	1.80E-02	6.8(2)
28138.20	C109 ζ	28138.816				0.11(1)	12(2)	8.46E-03	12.6(9)
	SO ₂ $v_2 = 1$	28138.394	$4_{0,4} - 3_{1,3}$	754.2	0.1				8.1(9)
28143.03	CH ₃ NH ₂	28142.850	$J_K = 18_1 - 18_0$	363.8	0.3	0.012(3)	3(1)	3.75E-03	4.1(5)
28169.43	E-CH ₃ OH	28169.470	$14_{2,13} - 14_{1,13}$	266.1	0.1	13.06(3)	2.2(1)	5.66E+00	6.4(1)

Table 6 continued

Table 6 (*continued*)

f_{obs}	Species	f_{rest}	Transition	E_u	A_{ij}	$\int T_{\text{MB}} \text{d}V$	ΔV	$T_{\text{MB}}^{\text{peak}}$	V_{LSR}
(MHz)		(MHz)		(K)	(10^{-6} s^{-1})	(K km s $^{-1}$)	(km s $^{-1}$)	K	km s $^{-1}$
28173.64	C ₂ H ₅ CN	28173.414	18 _{2,16} – 18 _{2,17}	79.0	0.04	0.042(8)	7(2)	5.35E-03	3.6(7)
	SO ₂ $v_2 = 1$	28173.485	8 _{2,6} – 9 _{1,9}	788.5	0.04				4.4(7)
28199.57	HC ₇ N	28199.798	J = 25 – 24	17.6	2.97	0.019(4)	3.4(7)	5.28E-03	8.4(4)
28239.53	A-CH ₃ OCHO	28239.630	9 _{2,8} – 8 _{3,5}	28.8	0.005	0.023(6)	2.5(8)	8.44E-03	7.1(3)
28261.46	E-CH ₃ OCHO	28261.511	9 _{2,8} – 8 _{3,5}	28.8	0.005	0.020(5)	3(1)	6.56E-03	6.6(3)
28267.70	¹³ CH ₃ OH	28267.770	11 _{2,9} – 11 _{1,10}	171.9	0.1	0.449(5)	3.5(1)	1.20E-01	6.7(1)
28315.98	E-CH ₃ OH	28316.067	4 _{0,4} – 3 _{1,2}	36.3	0.04	5.96(1)	4.4(1)	1.28E+00	6.9(1)
28329.43	AA-CH ₃ COCH ₃	28329.300	6 _{5,2} – 6 _{4,3}	18.2	0.5	0.025(6)	7(2)	3.55E-03	4.7(9)
28338.41	EE-CH ₃ COCH ₃	28338.466	11 _{8,3} – 11 _{7,4}	55.5	0.8	0.062(6)	5.1(6)	1.15E-02	6.6(2)
28344.05	U					0.018(5)	3(1)	5.58E-03	
28407.67	AA-CH ₃ COCH ₃	28407.350	11 _{8,3} – 11 _{7,4}	55.5	0.8	0.047(7)	3.8(6)	1.16E-02	2.7(2)
28406.53	A-CH ₃ OCHO	28406.628	21 _{8,14} – 20 _{9,11}	179.2	0.005	0.008(2)	1.7(6)	4.36E-03	7.0(3)
28441.12	C ₂ H ₃ CN	28441.026	3 _{0,3} – 2 _{0,2}	2.7	1.67	0.163(8)	10.5(7)	1.45E-02	5.1(1)
28456.12	C ₂ H ₃ CN	28455.983	3 _{2,2} – 2 _{2,1}	11.4	0.8	0.028(7)	8(2)	3.15E-03	5(1)
28457.31	C ₂ H ₃ CN	28457.201	3 _{2,2} – 2 _{2,1}	11.4	0.9	0.046(6)	5.4(9)	8.11E-03	4.9(3)
28543.11	H152 σ	28541.838				0.041(7)	9(2)	4.36E-03	-7.4(8)
	C ₂ H ₅ OH	28543.098	4 _{3,2} – 4 _{2,2}	76.2	0.06				5.9(8)
28596.85	AA-CH ₃ COCH ₃	28596.855	10 _{6,4} – 10 _{5,5}	44.7	0.8	0.023(5)	4(1)	4.99E-03	6.1(5)
28602.30	NH ₃	28604.737	(10 ₁₀ ,10 ₁₀)	1036.4	0.5	0.070(7)	8(1)	8.36E-03	31.5(4)
28604.85	NH ₃	28604.737	(10 ₁₀ ,10 ₁₀)	1036.4	0.5	3.04(2)	7.2(1)	3.99E-01	4.9(1)
28607.45	NH ₃	28604.737	(10 ₁₀ ,10 ₁₀)	1036.4	0.5	0.093(7)	13(1)	6.92E-03	-22.4(5)
28616.08	A-CH ₃ OCHO $v_t = 1$	28616.175	5 _{1,4} – 5 _{0,5}	197.8	0.04	0.037(8)	6.2(9)	5.67E-03	7.0(9)
28620.92	EE-CH ₃ COCH ₃	28620.971	10 _{6,4} – 10 _{5,5}	44.8	0.8	0.060(8)	5.1(9)	1.10E-02	6.5(9)
28622.50	C ₂ H ₅ CN	28622.275	6 _{1,5} – 6 _{0,6}	10.4	0.2	0.114(8)	8.7(9)	1.23E-02	3.6(9)
28629.96	AE-CH ₃ COCH ₃	28629.885	5 _{2,3} – 5 _{1,4}	11.6	0.5	0.014(3)	3.8(9)	3.43E-03	5.2(9)
28636.53	A-CH ₃ OCHO $v_t = 1$	28636.634	9 _{2,7} – 9 _{2,8}	217.8	0.03	0.009(2)	5(3)	1.78E-03	7(1)
28660.21	EA-CH ₃ COCH ₃	28660.137	10 _{6,4} – 10 _{5,5}	44.9	0.8	0.010(2)	1.8(7)	4.90E-03	5.3(3)
28671.15	EE-CH ₃ COCH ₃	28671.065	5 _{2,3} – 5 _{1,4}	11.5	0.5	0.018(5)	5(2)	3.49E-03	5.1(9)
28692.57	A-CH ₃ OCHO $v_t = 1$	28692.722	25 _{6,19} – 25 _{6,20}	405.0	0.03	0.007(2)	1.7(6)	4.16E-03	7.6(4)
28705.65	AA-CH ₃ COCH ₃	28705.700	5 _{2,3} – 5 _{1,4}	11.4	0.5	0.022(5)	3.7(9)	5.57E-03	6.5(9)
28747.66	¹³ CH ₃ OH	28747.750	12 _{2,10} – 12 _{1,11}	199.1	0.1	0.366(5)	3.4(9)	1.00E-01	7.0(9)
28857.98	SO ₂	28858.037	17 _{2,16} – 16 _{3,13}	149.2	0.04	12.64(2)	21.6(1)	5.50E-01	6.6(1)
28874.37	E-CH ₃ OH	28874.394	24 _{2,23} – 24 _{1,23}	718.4	0.07	0.33(1)	4.0(9)	7.78E-02	6.2(9)
28905.76	E-CH ₃ OH	28905.812	15 _{2,14} – 15 _{1,14}	301.0	0.1	10.23(2)	2.9(1)	3.31E+00	6.6(1)
28919.86	CH ₃ C ₃ N	28919.927	J _K = 7 ₁ – 6 ₁	13.0	2.90	0.037(5)	2.9(6)	1.18E-02	6.7(2)
28969.90	A-CH ₃ OH	28969.959	8 _{2,7} – 9 _{1,8}	121.3	0.05	6.13(7)	5.0(1)	1.16E+00	6.6(1)
28974.67	H ₂ CO	28974.805	3 _{1,2} – 3 _{1,3}	33.4	0.1	13.08(7)	4.4(1)	2.82E+00	7.4(1)
29091.20	CH ₃ OCH ₃	29091.288	3 _{0,3} ⁰ – 2 _{1,2} ⁰	5.4	0.08	0.170(7)	2.9(9)	5.59E-02	6.9(9)
29092.01	CH ₃ OCH ₃	29092.090	3 _{0,3} ¹ – 2 _{1,2} ¹	5.4	0.08	0.270(7)	3.0(9)	8.34E-02	6.9(9)
29092.81	CH ₃ OCH ₃	29092.895	3 _{0,3} ¹² – 2 _{1,2} ¹²	5.4	0.08	0.180(7)	3.3(9)	5.06E-02	6.9(9)

Table 6 *continued*

Table 6 (continued)

f_{obs} (MHz)	Species	f_{rest} (MHz)	Transition	E_u (K)	A_{ij} (10^{-6} s^{-1})	$\int T_{\text{MB}} \text{d}V$ (K km s $^{-1}$)	ΔV (km s $^{-1}$)	$T_{\text{MB}}^{\text{peak}}$ K	V_{LSR} km s $^{-1}$
29113.83	CH ₃ OH $v_t = 1$	29113.793	12 _{9,4} – 12 _{8,4}	864.3	0.05	0.083(8)	4.5(9)	1.72E–02	5.7(9)
29139.34	C ₂ H ₃ CN	29139.199	3 _{1,2} – 2 _{1,1}	5.0	1.34	0.084(8)	5.8(9)	1.35E–02	4.6(9)
29187.74	NH ₂ D	29187.763	7 _{2,6} – 7 _{1,6}	460.5	0.3	0.186(8)	5.4(9)	3.21E–02	6.2(9)
29255.89	C ₂ H ₅ OH	29255.814	5 _{1,4} – 5 _{2,4}	75.6	0.08	0.032(9)	6(3)	5.29E–03	5.2(7)
29266.84	C ₂ H ₅ OH	29266.907	5 _{1,4} – 6 _{0,6}	75.6	0.06	0.015(4)	4(1)	3.79E–03	6.7(6)
29288.97	HC ₅ N	29289.152	$J = 11 - 10$	8.4	2.62	0.29(1)	6.2(3)	4.50E–02	7.9(1)
	X II96 α		29287.782						-6.1(1)
29293.01	H ₂ CS	29293.210	7 _{1,6} – 7 _{1,7}	60.0	0.01	0.088(7)	3.8(3)	2.14E–02	8.0(1)
29315.14	¹³ CH ₃ OH	29315.200	13 _{2,11} – 13 _{1,12}	228.6	0.2	0.335(9)	3.5(1)	8.99E–02	6.6(1)
29321.20	SO ₂	29321.330	4 _{0,4} – 3 _{1,3}	9.2	0.1	27.25(2)	22.7(1)	1.13E+00	7.3(1)
29327.71	HC ₇ N	29327.768	$J = 26 - 25$	19.0	3.35	0.031(7)	5(1)	6.19E–03	6.6(6)
29401.45	E-CH ₃ OCHO	29401.796	5 _{1,4} – 5 _{0,5}	10.0	0.04	0.082(6)	2.9(3)	2.69E–02	9.5(1)
29417.40	A-CH ₃ OCHO	29417.462	5 _{1,4} – 5 _{0,5}	10.0	0.04	0.089(5)	2.7(2)	3.07E–02	6.7(1)
29429.90	H ₂ CCO	29430.020	12 _{1,11} – 12 _{1,12}	89.4	0.004	0.014(4)	2.9(8)	4.65E–03	7.2(4)
29460.48	C ₂ H ₅ CN	29460.274	15 _{2,13} – 14 _{3,12}	56.6	0.04	0.032(6)	6(1)	5.43E–03	3.9(6)
29584.77	HCN $v_2 = 1$	29584.660	11 ⁺ – 11 ⁻	1306.4	0.02	0.137(6)	5.5(3)	2.33E–02	4.9(1)
29625.17	A-CH ₃ OCHO	29625.340	12 _{4,8} – 11 _{5,7}	57.0	0.007	0.024(4)	4.5(8)	4.93E–03	7.7(4)
29636.89	E-CH ₃ OH	29636.942	16 _{2,15} – 16 _{1,15}	338.1	0.2	5.99(1)	4.4(1)	1.29E+00	6.5(1)
29678.73	³⁴ SO	29678.980	$N_J = 0_1 - 1_0$	1.4	0.2	3.34(1)	23.5(1)	1.33E–01	8.5(1)
29686.97	c-CH ₂ OCH ₂	29687.030	5 _{4,1} – 5 _{3,2}	33.0	0.4	0.047(4)	2.4(2)	1.83E–02	6.6(1)
29741.51	E-CH ₃ OCHO	29741.570	12 _{4,8} – 11 _{5,7}	57.0	0.004	0.010(2)	1.9(8)	4.73E–03	6.6(4)
29819.85	³³ SO	29819.833	$N_J = 0_1 - 1_0$	1.4	0.2	0.20(1)	19(2)	9.97E–03	5.8(8)
29857.34	³³ SO	29857.602	$N_J = 0_1 - 1_0$	1.4	0.2	0.44(2)	25(2)	1.62E–02	8.6(6)
29900.40	CH ₃ OCH ₃	29900.479	1 _{1,0} ¹¹ – 1 _{0,1} ¹¹	2.3	0.3	0.24(1)	3.3(9)	6.80E–02	6.8(9)
29901.30	CH ₃ OCH ₃	29901.394	1 _{1,0} ¹ – 1 _{0,1} ¹	2.3	0.3	0.35(1)	2.8(9)	1.19E–01	6.9(9)
29902.20	CH ₃ OCH ₃	29902.300	1 _{1,0} ⁰ – 1 _{0,1} ⁰	2.3	0.3	0.21(1)	2.8(9)	7.19E–02	7.0(9)
29914.02	NH ₃	29914.486	(11 ₁₁ ,11 ₁₁)	1237.6	0.6	0.99(2)	34(1)	2.70E–02	10.6(6)
29914.57	NH ₃	29914.486	(11 ₁₁ ,11 ₁₁)	1237.6	0.6	1.37(1)	5.8(1)	2.22E–01	5.1(1)
29955.64	¹³ CH ₃ OH	29955.700	14 _{2,12} – 14 _{1,13}	260.3	0.2	0.275(8)	3.7(1)	6.91E–02	6.6(1)
29979.28	C ₂ H ₅ OH	29979.381	3 _{1,2} – 3 _{0,3}	6.5	0.3	0.057(7)	4.0(5)	1.34E–02	7.0(1)
30001.38	SO	30001.580	$N_J = 0_1 - 1_0$	1.4	0.2	69.67(5)	24.0(1)	2.73E+00	8.0(1)
30005.99	EE-CH ₃ COCH ₃	30006.173	13 _{9,4} – 13 _{8,5}	75.8	1.0	0.14(1)	8.6(9)	1.57E–02	7.8(3)
30010.43	A-CH ₃ OH	30010.511	8 _{1,7} – 8 _{1,8}	98.8	0.003	0.854(8)	3.7(1)	2.14E–01	6.8(1)
30205.52	SO ₂	30205.549	16 _{2,14} – 17 _{1,17}	137.5	0.01	2.11(1)	19.2(2)	1.04E–01	6.2(1)
30218.76	X II95 α	30217.519				0.18(1)	15(2)	1.14E–02	-6.3(6)
	SO ₂	30218.740	56 _{10,46} – 55 _{11,45}	1714.7	0.07				5.8(6)
30307.99	E-CH ₃ OH	30308.033	17 _{2,16} – 17 _{1,16}	377.6	0.2	4.423(4)	4.2(1)	9.89E–01	6.5(1)
30429.89	CH ₃ OH $v_t = 1$	30429.883	13 _{9,5} – 13 _{8,5}	894.4	0.06	0.056(7)	4.1(6)	1.28E–02	6.0(3)
30521.34	C ₂ H ₅ OH	30521.578	7 _{3,4} – 7 _{2,6}	91.1	0.08	0.012(3)	3(2)	3.58E–03	8.3(9)
30559.66	A-CH ₃ OCHO	30559.815	5 _{1,4} – 4 _{2,3}	10.0	0.01	0.013(3)	1.2(9)	1.02E–02	7.5(9)

Table 6 continued

Table 6 (*continued*)

f_{obs}	Species	f_{rest}	Transition	E_u	A_{ij}	$\int T_{\text{MB}} \text{d}V$	ΔV	$T_{\text{MB}}^{\text{peak}}$	V_{LSR}
(MHz)		(MHz)	J_{K_a,K_c}	(K)	(10^{-6} s^{-1})	(K km s^{-1})	(km s^{-1})	K	km s^{-1}
30564.01	E-CH ₃ OCHO	30564.097	5 _{1,4} – 4 _{2,3}	10.0	0.01	0.019(5)	2.4(9)	7.65E-03	6.9(9)
30606.89	C ₂ H ₅ CN	30606.460	7 _{1,6} – 7 _{0,7}	13.4	0.2	0.37(1)	18(1)	1.92E-02	1.8(4)
30643.66	¹³ CH ₃ OH	30643.720	15 _{2,13} – 15 _{1,14}	294.3	0.2	0.251(8)	4.4(2)	5.42E-02	6.6(1)
30670.51	E-CH ₃ OCHO	30670.582	9 _{2,7} – 9 _{2,8}	30.2	0.03	0.087(7)	2.7(3)	3.04E-02	6.7(1)
30695.08	A-CH ₃ OCHO	30695.155	9 _{2,7} – 9 _{2,8}	30.2	0.03	0.071(6)	2.9(3)	2.27E-02	6.7(1)
30752.19	E-CH ₃ OH	30752.222	22 _{2,21} – 22 _{1,21}	609.6	0.1	0.80(2)	4.3(8)	1.74E-01	6.3(8)
30858.25	E-CH ₃ OH	30858.301	18 _{2,17} – 18 _{1,17}	419.4	0.2	3.419(8)	4.6(1)	6.96E-01	6.5(1)
30966.48	CH ₃ OCH ₃	30966.551	5 _{3,3} ¹² – 6 _{2,4} ¹²	26.3	0.02	0.027(7)	5(2)	4.94E-03	6.7(8)
30973.04	CH ₃ OCH ₃	30973.137	5 _{3,3} ¹ – 6 _{2,4} ¹	26.3	0.03	0.084(6)	2.7(2)	2.89E-02	6.9(1)
30975.31	³⁴ SO ₂	30975.450	8 _{1,7} – 7 _{2,6}	36.6	0.09	0.60(1)	15.7(5)	3.60E-02	7.4(2)
30977.00	³⁴ SO ₂	30975.450	8 _{1,7} – 7 _{2,6}	36.6	0.09	0.244(7)	76(8)	3.03E-03	-9(6)
30978.77	NH ₂ D	30978.726	6 _{2,5} – 6 _{1,5}	353.4	0.4	0.072(7)	3.7(4)	1.80E-02	5.6(2)
31011.01	³⁴ SO ₂	31011.180	4 _{0,4} – 3 _{1,3}	9.1	0.2	0.93(2)	24.8(7)	3.51E-02	7.6(3)
31011.23	³⁴ SO ₂	31011.180	4 _{0,4} – 3 _{1,3}	9.1	0.2	0.18(2)	6.8(5)	2.44E-02	5.5(2)
31090.06	SO ₂	31089.928	28 _{3,25} – 29 _{2,28}	403.0	0.01	0.16(1)	9.4(7)	1.60E-02	4.7(3)
31105.14	CH ₃ OCH ₃	31105.220	2 _{1,1} ¹¹ – 2 _{0,2} ¹¹	4.2	0.3	0.171(6)	2.4(1)	6.61E-02	6.8(1)
31106.05	CH ₃ OCH ₃	31106.150	2 _{1,1} ¹ – 2 _{0,2} ¹	4.2	0.3	0.442(7)	2.5(1)	1.63E-01	6.9(1)
31106.98	CH ₃ OCH ₃	31107.077	2 _{1,1} ⁰ – 2 _{0,2} ⁰	4.2	0.3	0.168(6)	2.4(1)	6.50E-02	7.0(1)
31209.74	E-CH ₃ OH	31209.778	21 _{2,20} – 21 _{1,20}	558.6	0.1	1.107(9)	4.2(1)	2.48E-01	6.3(1)
31226.70	E-CH ₃ OH	31226.750	19 _{2,18} – 19 _{1,18}	463.5	0.2	2.51(1)	4.5(1)	5.22E-01	6.5(1)
31306.58	AA-CH ₃ COCH ₃	31306.546	14 _{9,5} – 14 _{8,6}	86.2	1.19	0.06(1)	8(2)	7.61E-03	5.7(8)
31342.24	¹³ CH ₃ OH	31342.280	16 _{2,14} – 16 _{1,15}	330.6	0.2	0.141(8)	3.7(3)	3.61E-02	6.4(1)
31358.37	E-CH ₃ OH	31358.415	20 _{2,19} – 20 _{1,19}	509.9	0.1	1.729(9)	4.5(1)	3.61E-01	6.4(1)
31365.36	U					0.054(9)	7(1)	7.13E-03	
31425.02	NH ₃	31424.943	(12 _{12,12} 12 ₁₂)	1456.4	0.7	1.42(1)	8.0(1)	1.68E-01	5.3(1)
31573.34	C ₂ H ₅ CN	31573.070	34 _{8,26} – 35 _{7,29}	327.0	0.04	0.021(5)	6(2)	3.39E-03	3(1)
31723.66	AA-CH ₃ COCH ₃	31723.622	9 _{5,4} – 9 _{4,5}	36.1	0.9	0.019(2)	4.3(8)	4.29E-03	5.6(8)
31739.47	EE-CH ₃ COCH ₃	31739.498	9 _{5,4} – 9 _{4,5}	36.2	0.9	0.021(2)	2.7(8)	7.48E-03	6.3(8)
31740.92	AE-CH ₃ COCH ₃	31740.723	9 _{5,4} – 9 _{4,5}	36.3	0.9	0.011(2)	2.4(8)	4.35E-03	4.1(8)
31757.35	CH ₃ OH $v_t = 1$	31757.390	14 _{9,5} – 14 _{8,7}	926.8	0.07	0.049(2)	4.6(8)	9.89E-03	6.4(8)
31816.99	¹³ CH ₃ OH $v_t = 1$	31817.070	10 _{1,10} – 11 _{2,9}	449.5	0.1	0.013(3)	2.0(5)	5.83E-03	6.8(3)
31898.49	C ₂ H ₅ CN	31898.305	1 _{1,1} – 0 _{0,0}	1.5	0.2	0.035(7)	9(2)	3.69E-03	4(1)
31918.00	C ₂ H ₅ OH	31917.978	11 _{1,10} – 10 _{2,8}	114.2	0.06	0.021(4)	4.6(9)	4.23E-03	5.8(5)
31922.19	SO ₂	31922.210	16 _{4,12} – 17 _{3,15}	164.5	0.08	6.25(2)	25.6(1)	2.29E-01	6.1(1)
31922.25	SO ₂	31922.210	16 _{4,12} – 17 _{3,15}	164.5	0.08	1.47(2)	8.1(1)	1.69E-01	5.6(1)
31951.59	HC ₅ N	31951.772	$J = 12 - 11$	10.0	3.42	0.139(4)	3.7(1)	3.55E-02	7.7(1)
31977.74	E-CH ₃ OH	31977.791	19 _{4,15} – 20 _{3,18}	536.7	0.06	0.593(5)	4.1(1)	1.36E-01	6.5(1)
31996.01	CH ₃ OCH ₃	31996.105	9 _{2,7} ⁰ – 8 _{3,6} ⁰	47.0	0.04	0.099(5)	2.6(2)	3.55E-02	6.8(1)
31999.27	CH ₃ OCH ₃	31999.357	9 _{2,7} ¹ – 8 _{3,6} ¹	47.0	0.04	0.151(5)	2.5(1)	5.75E-02	6.8(1)
32002.48	CH ₃ OCH ₃	32002.458	9 _{2,7} ¹¹ – 8 _{3,6} ¹¹	47.0	0.04	0.117(7)	5.0(3)	2.19E-02	5.8(1)

Table 6 *continued*

Table 6 (continued)

f_{obs}	Species	f_{rest}	Transition	E_u	A_{ij}	$\int T_{\text{MB}} \text{d}V$	ΔV	$T_{\text{MB}}^{\text{peak}}$	V_{LSR}
(MHz)		(MHz)	J_{K_a,K_c}	(K)	(10^{-6} s^{-1})	(K km s $^{-1}$)	(km s $^{-1}$)	K	km s $^{-1}$
32004.29	$^{13}\text{CH}_3\text{OH}$	32004.340	$17_{2,15} - 17_{1,16}$	369.1	0.2	0.131(6)	3.9(2)	3.15E-02	6.4(1)
32071.92	HDCO	32072.200	$3_{1,2} - 3_{1,3}$	27.3	0.2	0.136(4)	3.5(1)	3.61E-02	8.6(1)
32190.88	EE- CH_3COCH_3	32190.958	$7_{5,3} - 7_{4,4}$	23.1	0.8	0.044(8)	7(2)	5.88E-03	6.7(6)
32206.02	E- CH_3OCHO	32206.029	$29_{7,22} - 29_{7,23}$	293.6	0.04	0.060(3)	10.3(8)	5.51E-03	6.1(8)
32253.38	A- CH_3OCHO	32253.467	$29_{7,22} - 29_{7,23}$	293.6	0.04	0.016(3)	1.8(4)	8.26E-03	6.8(2)
32272.86	$\text{He}104\zeta$	32272.195				0.12(1)	17(2)	6.45E-03	-0.2(8)
	$^{34}\text{SO}_2$	32272.340	$25_{6,20} - 26_{5,21}$	383.8	0.08				1.2(8)
32355.87	U					0.028(5)	3.0(5)	8.65E-03	
32379.35	$\text{CH}_3\text{OH } v_t = 1$	32379.386	$21_{5,17} - 20_{6,15}$	954.7	0.09	0.068(4)	3.0(2)	2.10E-02	6.3(1)
32398.40	$^{13}\text{CH}_3\text{OH}$	32398.480	$4_{1,4} - 3_{0,3}$	28.3	0.1	0.410(4)	3.1(1)	1.22E-01	6.7(1)
32454.46	U					0.015(3)	2.1(6)	6.71E-03	
32485.99	E- CH_3CHO	32486.053	$8_{1,7} - 7_{2,6}$	36.5	0.03	0.008(2)	1.4(7)	5.70E-03	6.6(2)
32539.19	AA- CH_3COCH_3	32538.241	$15_{10,5} - 15_{9,6}$	99.1	1.34	0.027(4)	2.9(5)	8.81E-03	-2.8(2)
32570.78	$\text{C}_2\text{H}_5\text{OH}$	32570.883	$6_{1,5} - 6_{2,5}$	80.7	0.1	0.015(4)	4(1)	3.44E-03	7.0(6)
32575.47	$^{13}\text{CH}_3\text{OH}$	32575.520	$18_{2,16} - 18_{1,17}$	409.9	0.2	0.074(3)	3.1(2)	2.27E-02	6.5(1)
32612.83	E- CH_3OCHO	32613.143	$42_{10,32} - 42_{10,33}$	607.1	0.04	0.010(2)	3.7(8)	2.57E-03	8.9(8)
32708.79	A- CH_3CHO	32709.214	$4_{0,4} - 3_{1,3}$	9.2	0.08	0.018(5)	5(2)	3.33E-03	9.9(8)
32742.71	$\text{C}_2\text{H}_5\text{OH}$	32742.830	$4_{1,3} - 4_{0,4}$	9.9	0.4	0.077(5)	4.4(4)	1.67E-02	7.1(1)
32837.25	AA- CH_3COCH_3	32837.510	$13_{8,5} - 13_{7,6}$	74.2	1.26	0.047(7)	5(1)	8.50E-03	8.4(4)
32873.07	EE- CH_3COCH_3	32873.058	$13_{8,5} - 13_{7,6}$	74.3	1.26	0.053(8)	6(1)	7.81E-03	5.9(5)
32973.45	$\text{C}_2\text{H}_5\text{CN}$	32973.250	$8_{1,7} - 8_{0,8}$	17.0	0.3	0.22(1)	9.9(5)	2.12E-02	4.2(2)
32977.18	CH_3OCH_3	32977.277	$3_{1,2}^{12} - 3_{0,3}^{12}$	7.0	0.3	0.348(6)	2.4(1)	1.35E-01	6.9(1)
32978.13	CH_3OCH_3	32978.232	$3_{1,2}^1 - 3_{0,3}^1$	7.0	0.3	0.523(6)	2.5(1)	2.00E-01	7.0(1)
32979.08	CH_3OCH_3	32979.187	$3_{1,2}^0 - 3_{0,3}^0$	7.0	0.3	0.330(6)	2.4(1)	1.29E-01	7.0(1)
32998.89	$^{13}\text{CH}_3\text{OH}$	32998.850	$19_{2,17} - 19_{1,18}$	452.9	0.2	0.074(5)	3.9(3)	1.77E-02	5.7(1)
33044.38	EE- CH_3COCH_3	33044.425	$8_{7,1} - 8_{6,2}$	32.1	0.5	0.008(2)	1.6(8)	5.00E-03	6.4(8)
33051.23	$\text{CH}_3\text{C}_3\text{N}$	33051.619	$J_K = 8_0 - 7_0$	7.1	4.46	0.039(6)	4.8(7)	7.72E-03	9.5(4)
33156.63	NH_3	33156.849	($13_{13}, 13_{13}$)	1692.7	0.8	0.37(1)	24(1)	1.47E-02	8.0(5)
33156.94	NH_3	33156.849	($13_{13}, 13_{13}$)	1692.7	0.8	0.17(1)	4.4(2)	3.56E-02	5.2(1)
33164.19	E- CH_3OCHO	33164.204	$6_{1,5} - 6_{1,6}$	13.7	0.03	0.057(5)	2.9(3)	1.88E-02	6.1(1)
33186.11	A- CH_3OCHO	33186.266	$6_{1,5} - 6_{1,6}$	13.7	0.03	0.046(5)	2.8(3)	1.54E-02	7.4(1)
33212.83	$^{34}\text{SO}_2$	33212.810	$17_{2,16} - 16_{3,13}$	148.5	0.06	0.394(4)	21.2(8)	1.75E-02	5.8(8)
33219.98	$^{13}\text{CH}_3\text{OH}$	33220.080	$20_{2,18} - 20_{1,19}$	498.2	0.2	0.036(4)	4.3(8)	7.83E-03	6.9(8)
33329.26	CH_3OCH_3	33329.338	$8_{4,5}^{12} - 9_{3,6}^{12}$	55.3	0.02	0.013(3)	1.7(8)	6.85E-03	6.7(8)
33336.63	CH_3OCH_3	33336.805	$8_{4,5}^{11} - 9_{3,6}^{11}$	55.3	0.04	0.071(3)	7.5(8)	8.84E-03	7.6(8)
33337.53	CH_3OCH_3	33337.611	$8_{4,5}^1 - 9_{3,6}^1$	55.3	0.03	0.070(3)	2.6(8)	2.50E-02	6.7(8)
33344.13	CH_3OCH_3	33344.224	$8_{4,5}^0 - 9_{3,6}^0$	55.3	0.04	0.050(3)	2.6(8)	1.79E-02	6.9(8)
33348.25	CH_3OCH_3	33348.357	$8_{4,4}^1 - 9_{3,6}^1$	55.3	0.010	0.027(3)	3.1(8)	8.28E-03	6.9(8)
33366.26	E- CH_3OCHO	33366.394	$10_{2,9} - 9_{3,6}$	34.5	0.007	0.034(3)	5.8(8)	5.48E-03	7.2(8)
33376.37	CH_3OCH_3	33376.636	$5_{3,3}^1 - 6_{2,5}^1$	26.3	0.002	0.053(3)	7.4(8)	6.68E-03	8.4(8)

Table 6 continued

Table 6 (*continued*)

f_{obs}	Species	f_{rest}	Transition	E_u	A_{ij}	$\int T_{\text{MB}} \text{d}V$	ΔV	$T_{\text{MB}}^{\text{peak}}$	V_{LSR}
(MHz)		(MHz)	J_{K_a,K_c}	(K)	(10^{-6} s^{-1})	(K km s^{-1})	(km s^{-1})	K	km s^{-1}
33386.70	U					0.018(4)	2.1(5)	7.80E-03	
33392.62	CH_3OCH_3	33392.739	$5_{3,2}^{11} - 6_{2,5}^{11}$	26.3	0.03	0.028(2)	2.3(8)	1.13E-02	7.0(8)
33397.33	CH_3OCH_3	33397.481	$5_{3,2}^1 - 6_{2,5}^1$	26.3	0.03	0.098(2)	3.7(8)	2.47E-02	7.3(8)
33399.54	CH_3OCH_3	33399.668	$5_{3,2}^0 - 6_{2,5}^0$	26.3	0.03	0.051(2)	2.8(8)	1.70E-02	7.2(8)
33446.89	$\text{C}_2\text{H}_5\text{CN}$	33446.898	$19_{2,17} - 19_{2,18}$	87.3	0.06	0.068(8)	12.6(8)	5.06E-03	6.1(8)
33508.38	$\text{C}_2\text{H}_5\text{OH}$	33508.434	$2_{1,2} - 1_{1,1}$	65.2	0.2	0.007(2)	0.9(4)	7.20E-03	6.5(2)
33555.64	$\text{AE-CH}_3\text{COCH}_3$	33555.523	$3_{0,3} - 2_{1,2}$	3.7	1.26	0.015(4)	2.1(7)	6.72E-03	5.0(3)
33566.38	$\text{AA-CH}_3\text{COCH}_3$	33566.289	$3_{0,3} - 2_{1,2}$	3.5	1.26	0.031(8)	5(1)	6.29E-03	5.2(1)
33630.14	$\text{C}_2\text{H}_5\text{CN}$	33629.960	$6_{0,6} - 5_{1,5}$	9.0	0.1	0.102(2)	11.9(8)	8.04E-03	4.4(8)
33691.60	$\text{A-CH}_3\text{OH}$	33691.663	$23_{5,19} - 24_{4,20}$	777.9	0.07	0.079(2)	3.0(8)	2.47E-02	6.6(8)
33751.28	CCS	33751.370	$N_J = 2_3 - 1_2$	3.2	1.58	0.027(4)	4.8(8)	5.27E-03	6.8(8)
33904.06	$\text{A-CH}_3\text{OCHO}$ $v_t = 1$	33904.211	$3_{1,3} - 2_{1,2}$	191.8	0.5	0.054(6)	2.7(8)	1.85E-02	7.4(8)
33918.87	$\text{CH}_3^{18}\text{OH}$	33919.030	$2_{2,0} - 2_{1,1}$	29.1	0.04	0.031(6)	4(1)	6.80E-03	7.4(3)
33925.37	$\text{CH}_3^{18}\text{OH}$	33925.510	$3_{2,1} - 3_{1,2}$	35.7	0.04	0.083(6)	4.2(8)	1.88E-02	7.2(8)
33932.24	CH_3OCH_3	33932.378	$8_{4,5}^1 - 9_{3,7}^1$	55.3	0.01	0.022(6)	2.7(8)	7.62E-03	7.3(8)
33936.41	CH_3OCH_3	33936.516	$8_{4,4}^{11} - 9_{3,7}^{11}$	55.3	0.04	0.032(6)	3.0(8)	1.02E-02	6.9(8)
33943.00	CH_3OCH_3	33943.123	$8_{4,4}^1 - 9_{3,7}^1$	55.3	0.03	0.080(6)	3.6(8)	2.10E-02	7.1(8)
33943.74	CH_3OCH_3	33943.924	$8_{4,4}^0 - 9_{3,7}^0$	55.3	0.04	0.125(6)	5.6(8)	2.08E-02	7.6(8)
33981.26	$\text{CH}_3^{18}\text{OH}$	33981.400	$5_{2,3} - 5_{1,4}$	55.8	0.05	0.054(5)	3.5(5)	1.45E-02	7.2(1)
34003.42	$\text{A-CH}_3\text{OH}$	34003.457	$23_{5,18} - 24_{4,21}$	777.9	0.07	0.123(7)	4.5(3)	2.57E-02	6.3(1)
34048.26	$\text{CH}_3^{18}\text{OH}$	34048.422	$6_{2,4} - 6_{1,5}$	69.1	0.05	0.048(5)	2.7(3)	1.67E-02	7.4(1)
34092.91	$\text{EE-CH}_3\text{COCH}_3$	34092.973	$3_{1,3} - 2_{0,2}$	3.6	1.35	0.025(5)	3.2(6)	7.40E-03	6.6(3)
34097.71	SO_2	34097.720	$26_{6,20} - 27_{5,23}$	411.4	0.09	0.656(7)	21.2(8)	2.90E-02	6.1(8)
34097.87	SO_2	34097.720	$26_{6,20} - 27_{5,23}$	411.4	0.09	0.360(7)	5.6(8)	6.00E-02	4.7(8)
34100.07	H_2CO	34100.050	$10_{2,8} - 10_{2,9}$	240.7	0.09	0.349(7)	7.3(8)	4.51E-02	5.8(8)
34147.62	$\text{c-CH}_2\text{OCH}_2$	34147.720	$4_{4,0} - 4_{3,1}$	23.3	0.4	0.028(7)	1.6(8)	1.60E-02	6.8(8)
34155.55	$\text{CH}_3^{18}\text{OH}$	34155.634	$7_{2,5} - 7_{1,6}$	84.7	0.05	0.026(4)	1.9(4)	1.29E-02	6.8(1)
34156.78	$\text{E-CH}_3\text{OCHO}$	34156.884	$3_{1,3} - 2_{1,2}$	4.0	0.5	0.27(2)	2.6(3)	9.66E-02	6.9(1)
34157.96	$\text{A-CH}_3\text{OCHO}$	34158.119	$3_{1,3} - 2_{1,2}$	3.9	0.5	0.28(3)	2.8(3)	9.33E-02	7.4(1)
34160.53	$\text{E-CH}_3\text{OCHO}$ $v_t = 1$	34160.654	$3_{1,3} - 2_{1,2}$	191.0	0.5	0.05(1)	3(2)	1.48E-02	7.1(9)
34182.43	CH_3CCH	34182.760	$J_K = 2_1 - 1_1$	9.7	0.09	0.156(4)	2.6(1)	5.67E-02	8.9(1)
34183.11	CH_3CCH	34183.414	$J_K = 2_0 - 1_0$	2.5	0.1	0.332(7)	4.0(1)	7.75E-02	8.7(1)
34212.56	$\text{EE-CH}_3\text{COCH}_3$	34212.823	$8_{6,3} - 8_{5,4}$	30.3	1.0	0.031(5)	3.6(7)	7.89E-03	8.3(3)
34228.92	^{18}OCS	34229.045	$J = 3 - 2$	3.3	0.1	0.019(5)	2.4(9)	7.28E-03	7.1(3)
34236.90	$\text{E-CH}_3\text{OH}$	34236.946	$14_{3,11} - 15_{2,13}$	306.4	0.08	1.820(7)	5.0(1)	3.40E-01	6.4(1)
34267.50	$\text{C}_2\text{H}_5\text{CN}$	34267.229	$18_{2,17} - 17_{3,14}$	77.6	0.05	0.044(9)	7(2)	5.80E-03	3.6(8)
34314.48	$\text{CH}_3^{18}\text{OH}$	34314.613	$8_{2,6} - 8_{1,7}$	102.5	0.06	0.080(7)	4.6(5)	1.64E-02	7.1(2)
34351.20	H_2CS	34351.430	$1_{0,1} - 0_{0,0}$	1.6	0.4	0.219(5)	4.1(1)	5.02E-02	8.0(1)
34392.39	SO_2	34393.562	$51_{9,43} - 50_{10,40}$	1420.1	0.10	0.032(5)	3.6(6)	8.39E-03	16.2(3)
34410.61	$\text{AA-CH}_3\text{COCH}_3$	34410.715	$8_{6,3} - 8_{5,4}$	30.2	1.02	0.013(2)	3.6(8)	3.43E-03	6.9(8)

Table 6 *continued*

Table 6 (continued)

f_{obs} (MHz)	Species	f_{rest} (MHz)	Transition	E_u (K)	A_{ij} (10^{-6} s^{-1})	$\int T_{\text{MB}} \text{d}V$ (K km s $^{-1}$)	ΔV (km s $^{-1}$)	$T_{\text{MB}}^{\text{peak}}$ K	V_{LSR} km s $^{-1}$
34417.82	CH ₃ OH $v_t = 1$	34417.849	16 _{9,8} – 16 _{8,8}	998.5	0.08	0.030(2)	3.0(8)	9.53E-03	6.2(8)
34426.44	E-CH ₃ OCHO	34426.510	13 _{3,10} – 13 _{3,11}	61.3	0.04	0.077(2)	3.5(8)	2.08E-02	6.6(8)
34458.70	A-CH ₃ OCHO	34458.782	13 _{3,10} – 13 _{3,11}	61.3	0.04	0.090(8)	2.8(3)	3.08E-02	6.7(1)
34476.09	E-CH ₃ OCHO	34476.397	25 _{6,19} – 25 _{6,20}	219.3	0.05	0.022(6)	3(1)	6.76E-03	8.6(5)
34520.38	EE-CH ₃ COCH ₃	34520.498	10 _{8,2} – 10 _{7,3}	47.6	0.9	0.018(5)	3(2)	6.14E-03	7.1(6)
34521.36	U				0.06(1)	5(2)	1.12E-02		
34522.77	A-CH ₃ OCHO	34522.996	25 _{6,19} – 25 _{6,20}	219.3	0.05	0.09(1)	8(2)	1.05E-02	8.0(4)
34528.04	CH ₃ NH ₂	34527.842	$J_K = 17_1 - 17_0$	326.2	0.5	0.04(1)	7(2)	5.67E-03	4.3(9)
34614.14	A-CH ₃ OCHO	34614.138	46 _{19,28} – 45 _{20,25}	877.7	0.009	0.23(2)	5.4(7)	4.08E-02	6.0(7)
34671.65	E-CH ₃ OCHO	34671.760	6 _{2,4} – 6 _{1,5}	15.4	0.09	0.11(1)	3.3(4)	3.19E-02	6.9(1)
34682.67	A-CH ₃ OCHO	34682.805	6 _{2,4} – 6 _{1,5}	15.3	0.09	0.14(1)	3.9(4)	3.44E-02	7.1(2)
34684.32	CH ₃ OCH ₃	34684.606	2 _{2,0} ⁰ – 3 _{1,3} ⁰	8.4	0.03	0.027(7)	2(1)	1.04E-02	8.5(4)
34709.00	CH ₃ ¹⁸ OH	34709.349	4 _{1,4} – 3 _{0,3}	27.9	0.03	0.056(7)	3.7(4)	1.41E-02	9.0(2)
34710.96	¹³ CH ₃ OH	34711.060	12 _{2,10} – 11 _{3,8}	199.1	0.07	0.137(9)	4.4(4)	2.95E-02	6.8(1)
34722.93	A-CH ₃ OCHO $v_t = 1$	34722.975	6 _{2,4} – 6 _{1,5}	203.1	0.09	0.022(5)	2.2(6)	9.20E-03	6.4(3)
34765.87	E-CH ₃ OCHO	34765.995	5 _{2,3} – 5 _{1,4}	11.7	0.08	0.069(4)	2.2(7)	2.94E-02	7.1(7)
34775.57	A-CH ₃ OCHO	34775.651	5 _{2,3} – 5 _{1,4}	11.7	0.08	0.107(4)	3.2(7)	3.11E-02	6.7(7)
34824.33	C ₂ H ₅ CN	34824.070	4 _{1,4} – 3 _{1,3}	5.3	3.04	1.15(1)	12.0(2)	9.05E-02	3.8(1)
34831.54	CH ₃ ¹⁸ OH	34831.596	10 _{2,8} – 10 _{1,9}	144.8	0.06	0.022(5)	1.8(4)	1.14E-02	6.5(2)
34855.42	HC ₃ N $v_7 = 1$	34855.467	$J = 73 - 73$	1504.0	0.001	0.38(2)	13.4(8)	2.69E-02	6.4(4)
34857.42	HC ₃ N $v_7 = 1$	34855.467	$J = 73 - 73$	1504.0	0.001	1.82(2)	19.0(3)	8.99E-02	-10.8(1)
34897.89	C ₂ H ₅ CN $v13/v21$	34897.722		301.5	0.001	0.093(9)	6.3(7)	1.39E-02	4.5(2)
34953.93	HCN $v_2 = 1$	34953.760	12 ⁻ – 12 ⁺	1357.7	0.03	0.16(1)	7.5(7)	1.99E-02	4.6(7)
34971.48	A-CH ₃ OCHO $v_t = 1$	34971.533	5 _{2,3} – 5 _{1,4}	199.5	0.09	0.024(6)	4.0(7)	5.70E-03	6.4(7)
34992.15	CH ₃ OCH ₃	34992.444	11 _{5,7} ¹² – 12 _{4,8} ¹²	95.2	0.02	0.010(2)	1.4(7)	6.70E-03	8.5(7)
34999.60	CH ₃ OCH ₃	34999.655	11 _{5,7} ¹¹ – 12 _{4,8} ¹¹	95.2	0.04	0.04(1)	2.6(7)	1.61E-02	6.5(7)

D. LINE LIST OF RRLS UNBLENDED WITH MOLECULAR LINES

Table 7 shows the results of identification and Gaussian fitting of RRLs. The RRLs blended with molecular lines are not included (see Table 6).

Table Notes:

- (1) Doppler correction has been applied to f_{obs} assuming a source velocity of 6 km s $^{-1}$ in LSR (Sect. 3.1). f_{obs} with a superscript of ‘*’ means it is only marginally detected.
- Rows with empty f_{obs} correspond to blended lines.
- (2) The emitter of ion RRL is denoted as X II, and the f_{rest} is adopted as the rest frequency of the corresponding C II RRL. The unidentified species is denoted as U.
- (3) The numbers in brackets in the 4th and 5th columns represent the uncertainties of the **last digital** of corresponding parameters.

Table 7. Linelist

f_{obs} (MHz)	Species	f_{rest} (MHz)	$\int T_{\text{MB}} dV$ (K km s $^{-1}$)	ΔV (km s $^{-1}$)	$T_{\text{MB}}^{\text{peak}}$ K	V_{LSR} km s $^{-1}$
26162.51	H135 λ	26161.602	0.21(1)	17(1)	1.16E-02	-4.4(6)
26197.28	H154 ρ	26196.134	0.073(9)	20(1)	3.48E-03	-7(1)
26206.55	H142 ν	26205.853	0.313(9)	30(1)	9.93E-03	-2(1)
26214.56	H131 κ	26213.600	0.439(9)	25(1)	1.62E-02	-5(1)
26284.90	H159 τ	26283.781	0.12(1)	21(3)	5.08E-03	-7(2)
26309.59	H151 π	26308.667	0.028(8)	9(4)	2.81E-03	-5(2)
26316.70	X II125 β	26315.897	0.04(1)	12(3)	3.13E-03	-3(2)
26326.36	H98 δ	26325.466	4.27(2)	25(1)	1.60E-01	-4(1)
	H145 ξ	26327.520				19(1)
26337.13	He98 δ	26336.194	0.26(2)	16(1)	1.51E-02	-5(1)
26354.04	H117 η	26353.516	1.71(2)	26(1)	6.29E-02	0(1)
	H122 θ	26352.556				-11(1)
26357.79	H148 σ	26356.734	0.029(8)	6(1)	4.24E-03	-6(1)
26365.04	He117 η	26364.255	0.23(2)	24(1)	9.11E-03	-3(1)
	He122 θ	26363.295				-14(1)
26497.08	H105 ϵ	26496.169	2.02(1)	22.3(1)	8.52E-02	-4.3(1)
26507.92	H156 σ	26508.023	0.19(1)	15.3(9)	1.19E-02	7.2(4)
	He105 ϵ	26506.966				-4.8(4)
26509.32	C105 ϵ	26509.389	0.017(4)	3(1)	4.67E-03	6.8(6)
26631.60	H89 γ	26630.710	7.08(1)	24.7(1)	2.69E-01	-4.0(1)
26642.53	He89 γ	26641.562	0.626(6)	18(1)	3.34E-02	-5(1)
26643.81	C89 γ	26643.997	0.064(6)	5(1)	1.25E-02	8(1)
26669.93	H111 ζ	26669.016	1.83(1)	25.3(2)	6.80E-02	-4.3(1)
26680.55	He111 ζ	26679.884	0.06(1)	9(3)	6.44E-03	-1(1)
26685.24	H78 β	26684.341	14.85(1)	24.1(1)	5.79E-01	-4.1(1)
26694.51	H126 ι	26693.958	0.52(6)	21(2)	2.26E-02	0(1)
26696.10	He78 β	26695.215	1.54(6)	17.3(4)	8.36E-02	-3.9(2)
26697.48	C78 β	26697.656	0.09(1)	3.4(3)	2.39E-02	8.0(1)
26718.82	X II99 α	26717.622	0.19(1)	15(1)	1.18E-02	-7.4(4)
26730.42	H134 λ	26729.441	0.37(1)	25(1)	1.42E-02	-5.0(4)
26744.59	H141 ν	26743.872	0.19(1)	25(3)	7.28E-03	-2.0(9)

Table 7 *continued*

Table 7 (continued)

f_{obs} (MHz)	Species	f_{rest} (MHz)	$\int T_{\text{MB}} \text{d}V$ (K km s $^{-1}$)	ΔV (km s $^{-1}$)	$T_{\text{MB}}^{\text{peak}}$ K	V_{LSR} km s $^{-1}$
26802.42	H130 κ	26801.529	0.53(1)	26(1)	1.91E-02	-4(1)
26814.06	H150 π	26813.095	0.17(1)	25(1)	6.40E-03	-5(1)
26856.36	H114 ξ	26855.572	0.18(1)	19(1)	9.07E-03	-2.8(6)
26867.14	He114 ξ	26866.516	0.022(6)	11(3)	1.87E-03	-1(3)
26874.90	H147 σ	26873.462	0.16(1)	22(2)	6.71E-03	-10(1)
26885.57	He147 σ	26884.413	0.04(1)	10(5)	3.42E-03	-7(2)
26940.07	H62 α	26939.164	55.45(1)	24.0(1)	2.17E+00	-4.0(1)
26951.06	He62 α	26950.142	4.82(1)	16.5(1)	2.75E-01	-4(1)
26952.44	C62 α	26952.606	0.396(8)	4.2(1)	8.86E-02	7.8(1)
26957.27	H160 ν	26956.439	0.08(2)	14(3)	4.97E-03	-3(2)
26991.88	H121 θ	26990.965	0.7(2)	22(1)	3.20E-02	-4.2(1)
27022.47	H116 η	27021.430	1.17(1)	22.7(2)	4.86E-02	-5.6(1)
27033.47	He116 η	27032.441	0.025(7)	12(5)	2.06E-03	-5(2)
27082.34	H137 μ	27081.467	0.35(1)	27(2)	1.23E-02	-3.7(6)
27132.64	H97 δ	27131.734	4.06(1)	24.8(1)	1.54E-01	-4.1(1)
27143.68	He97 δ	27142.790	0.33(1)	16.0(5)	1.95E-02	-3.8(1)
27145.05	C97 δ	27145.271	0.029(5)	3.7(7)	7.29E-03	8.4(3)
27192.59	H152 ρ	27191.424	0.09(1)	26(4)	3.39E-03	-7(2)
27251.06	H104 ϵ	27250.126	2.10(1)	24.1(1)	8.19E-02	-4.2(1)
27262.36	He104 ϵ	27261.231	0.24(1)	21(1)	1.05E-02	-6.4(4)
27314.69	H133 λ	27313.841	0.439(5)	30(1)	1.37E-02	-3(1)
27319.03	H125 ι	27318.147	0.629(5)	26(1)	2.30E-02	-4(1)
27331.31	H149 π	27330.513	0.155(5)	23(1)	6.39E-03	-3(1)
	He125 ι	27329.279				-16(1)
27384.97	H110 ζ	27384.002	1.70(1)	25(1)	6.32E-02	-5(1)
27396.83	He110 ζ	27395.161	0.11(1)	22(1)	4.53E-03	-12(1)
27398.81	H143 ξ	27397.851	0.21(1)	22(1)	9.15E-03	-4(1)
27408.14	H129 κ	27407.180	0.75(1)	33(1)	2.15E-02	-4(1)
27500.42	H154 σ	27499.852	0.031(8)	13(6)	2.34E-03	0(3)
27534.62	H88 γ	27533.710	7.84(1)	23.9(1)	3.08E-01	-3.9(1)
27540.91	X II98 α	27539.674	0.202(6)	15(1)	1.26E-02	-7(1)
27545.87	He88 γ	27544.930	0.664(6)	17(1)	3.77E-02	-4(1)
27547.24	C88 γ	27547.448	0.057(6)	4(1)	1.50E-02	8(1)
27651.10	H120 θ	27650.171	1.28(1)	26.1(3)	4.59E-02	-4.0(1)
27660.04	H136 μ	27659.029	0.25(1)	23(1)	9.83E-03	-5.0(7)
	He120 θ	27661.438				21.2(7)
27671.11	He136 μ	27670.300	0.08(1)	30(8)	2.47E-03	-3(1)
27708.51	H151 ρ	27708.035	0.19(1)	30(2)	5.96E-03	1(3)
27713.08	H115 η	27712.112	1.43(1)	25.1(3)	5.36E-02	-4.4(1)
27725.02	H77 β	27724.106	18.06(1)	24.4(1)	6.95E-01	-3.8(1)

Table 7 continued

Table 7 (*continued*)

f_{obs}	Species	f_{rest}	$\int T_{\text{MB}} dV$	ΔV	$T_{\text{MB}}^{\text{peak}}$	V_{LSR}
(MHz)		(MHz)	(K km s $^{-1}$)	(km s $^{-1}$)	K	km s $^{-1}$
27736.36	He77 β	27735.403	1.95(2)	18.6(9)	9.88E-02	-4.3(9)
27737.82	C77 β	27737.939	0.16(2)	5.1(9)	2.96E-02	7.3(9)
27862.06	H148 π	27861.342	0.07(1)	19(2)	3.58E-03	-2(2)
27866.50	H139 ν	27864.942	0.065(8)	15.2(9)	4.02E-03	-10.7(9)
27916.44	H132 λ	27915.411	0.29(1)	21(1)	1.29E-02	-5.1(4)
27949.40	H145 σ	27948.192	0.16(1)	23(2)	6.38E-03	-7.0(9)
27956.33	H142 ξ	27954.839	0.09(1)	15(3)	5.88E-03	-10(1)
27963.21	H124 ι	27961.957	0.32(1)	25(1)	1.22E-02	-7.5(6)
27972.16	H96 δ	27971.270	6.10(1)	26.6(1)	2.15E-01	-3.6(1)
27983.74	He96 δ	27982.668	0.45(1)	18.7(5)	2.27E-02	-5.5(2)
28032.69	H128 κ	28031.227	0.86(1)	28(1)	2.89E-02	-9.7(4)
28033.98	H103 ϵ	28032.968	2.002(1)	22.9(2)	8.21E-02	-4.8(1)
28045.09	He103 ϵ	28044.392	0.13(1)	14(1)	8.84E-03	-1.4(5)
28125.74	H109 ζ	28124.783	1.82(1)	24.1(2)	7.10E-02	-4.2(1)
28137.25	He109 ζ	28136.244	0.26(1)	20(1)	1.22E-02	-4.7(1)
28238.77	H150 ρ	28237.829	0.07(1)	19(5)	3.49E-03	-4.0(3)
28254.33	H135 μ	28253.141	0.167(9)	19(1)	8.09E-03	-6.7(6)
28275.81	H61 α	28274.872	61.31(1)	24.1(1)	2.39E+00	-4.0(1)
28287.37	He61 α	28286.394	5.16(8)	15.9(9)	3.04E-01	-4.4(1)
28288.80	C61 α	28288.980	0.41(8)	4.2(9)	9.23E-02	7.9(9)
28332.03	H119 θ	28331.027	1.07(1)	25.4(3)	3.96E-02	-5(1)
28343.49	He119 θ	28342.572	0.04(1)	18(6)	2.23E-03	-4(4)
28345.00*	C119 θ	28345.162	0.009(2)	2.4(9)	3.40E-03	7.8(5)
28397.23	X II97 α	28395.800	0.24(1)	17(1)	1.31E-02	-9.1(4)
28407.19	H147 π	28406.019	0.19(1)	27(2)	6.66E-03	-6(1)
28427.52	H114 η	28426.543	1.35(1)	25.6(2)	4.96E-02	-4.3(1)
28439.10	He114 η	28438.126	0.110(9)	17(2)	5.98E-03	-4.2(8)
28449.97	H138 ν	28449.046	0.296(9)	26.2(9)	1.06E-02	-3.7(4)
28478.97	H87 γ	28478.006	7.47(1)	24.2(1)	2.90E-01	-4.1(1)
28490.64	He87 γ	28489.611	0.628(8)	16.4(3)	3.60E-02	-4.8(1)
28492.02	C87 γ	28492.215	0.054(5)	4.0(4)	1.27E-02	8.1(1)
28527.88	H141 ξ	28527.040	0.27(1)	28(1)	8.87E-03	-2.8(7)
28535.65	H131 λ	28534.787	0.67(1)	31.4(7)	2.00E-02	-3.0(3)
28627.09	H123 ι	28626.166	0.699(8)	24.8(9)	2.65E-02	-3.6(9)
28638.95	He123 ι	28637.831	0.04(1)	16(10)	2.56E-03	-6(2)
28675.37	H127 κ	28674.373	0.96(1)	33.8(7)	2.66E-02	-4.4(3)
28687.21	He127 κ	28686.058	0.06(1)	16(5)	3.73E-03	-6(2)
28688.41*	C127 κ	28688.680	0.028(8)	4(2)	6.06E-03	8.8(6)
28782.48	H149 ρ	28781.230	0.041(5)	12.0(9)	3.21E-03	-7.1(9)
28819.56	H76 β	28818.602	15.73(1)	24.2(1)	6.10E-01	-4.0(1)

Table 7 *continued*

Table 7 (continued)

f_{obs} (MHz)	Species	f_{rest} (MHz)	$\int T_{\text{MB}} \text{d}V$ (K km s $^{-1}$)	ΔV (km s $^{-1}$)	$T_{\text{MB}}^{\text{peak}}$ K	V_{LSR} km s $^{-1}$
28831.35	He76 β	28830.346	1.32(1)	15.6(2)	7.94E-02	-4.4(1)
28832.82	C76 β	28832.981	0.132(8)	5.3(4)	2.33E-02	7.6(1)
28846.88	H95 δ	28845.808	6.85(1)	24.8(1)	2.59E-01	-5.1(1)
	H102 ϵ	28846.091				-2.2(1)
28865.45	H134 μ	28864.401	0.52(1)	28.8(9)	1.71E-02	-4.9(9)
28893.53	H108 ζ	28892.531	1.81(1)	25.4(9)	6.68E-02	-4.3(9)
29035.43	H118 θ	29034.429	1.074(7)	26.3(9)	3.83E-02	-4.4(9)
29047.39	He118 θ	29046.261	0.160(7)	18.7(9)	8.01E-03	-5.6(9)
29050.23	H137 ν	29049.602	0.158(7)	20.7(9)	7.15E-03	-0.5(9)
29082.51	H143 σ	29081.050	0.148(7)	26.9(9)	5.18E-03	-9.1(9)
29116.09	H140 ξ	29114.976	0.039(8)	12.7(9)	2.92E-03	-5.4(9)
29166.75	H113 η	29165.751	1.608(8)	27.8(9)	5.43E-02	-4.3(9)
29173.67	H130 λ	29172.633	0.424(8)	25.9(9)	1.54E-02	-4.6(9)
29312.81	H122 ι	29311.589	1.57(3)	45(1)	3.28E-02	-6.5(7)
29338.39	H126 κ	29337.356	0.80(2)	30.9(9)	2.42E-02	-4.6(4)
29466.96	H86 γ	29465.985	6.68(3)	24.3(9)	2.59E-01	-3.9(9)
29479.09	He86 γ	29477.993	0.80(3)	22.5(9)	3.36E-02	-5.2(9)
29480.50	C86 γ	29480.688	0.022(4)	2.2(4)	9.36E-03	7.9(2)
29494.68	H133 μ	29493.434	0.54(3)	36.2(9)	1.41E-02	-6.7(9)
29540.14	H145 π	29538.758	0.07(1)	16(3)	4.39E-03	-8(1)
29668.04	H136 ν	29667.192	0.12(1)	21(2)	5.59E-03	-3(1)
29671.33	H142 σ	29670.512	0.033(7)	10(2)	3.06E-03	-2(1)
29689.44	H107 ζ	29688.487	1.93(8)	26.7(7)	6.79E-02	-3.6(4)
29692.00	H101 ϵ	29690.975	2.73(7)	25.9(4)	9.93E-02	-4.3(3)
29701.35	H60 α	29700.365	51.01(1)	24.1(1)	1.99E+00	-3.9(1)
29713.48	He60 α	29712.468	4.36(1)	16.3(1)	2.52E-01	-4.2(1)
29714.99	C60 α	29715.184	0.295(9)	3.6(1)	7.62E-02	8.0(1)
29720.28	H139 ξ	29719.193	0.24(1)	27(2)	8.42E-03	-5(1)
29758.18	H94 δ	29757.192	4.20(1)	25.4(1)	1.56E-01	-4.0(1)
29762.27	H117 θ	29761.320	1.07(1)	26.6(5)	3.80E-02	-3.6(2)
29770.33	He94 δ	29769.318	0.30(1)	15.8(8)	1.81E-02	-4.2(3)
29830.69	H129 λ	29829.643	0.53(2)	31(2)	1.59E-02	-4.5(6)
29931.82	H112 η	29930.821	1.39(1)	27.4(4)	4.76E-02	-4.0(2)
29972.51	H75 β	29971.480	15.83(1)	23.7(1)	6.28E-01	-4.3(1)
29984.74	He75 β	29983.694	1.29(1)	16.2(2)	7.48E-02	-4.4(1)
29986.22	C75 β	29986.434	0.085(9)	3.4(4)	2.33E-02	8.2(1)
30020.89	H121 ι	30019.079	1.55(2)	39.7(8)	3.68E-02	-12.1(3)
	H125 κ	30020.946				6.5(3)
30032.97	He121 ι	30031.312	0.05(1)	13(3)	3.68E-03	-11(2)
	He125 κ	30033.179				8(2)

Table 7 continued

Table 7 (*continued*)

f_{obs}	Species	f_{rest}	$\int T_{\text{MB}} \text{d}V$	ΔV	$T_{\text{MB}}^{\text{peak}}$	V_{LSR}
(MHz)		(MHz)	(K km s $^{-1}$)	(km s $^{-1}$)	K	km s $^{-1}$
30142.08	H132 μ	30140.890	0.27(2)	28(3)	8.83E-03	-6(1)
30303.59	H135 ν	30302.426	0.07(1)	14(3)	4.86E-03	-5(2)
30434.39	H151 τ	30433.050	0.04(1)	11(4)	3.54E-03	-7(2)
30501.19	H85 γ	30500.204	6.38(3)	24.4(9)	2.45E-01	-3.7(9)
30507.62	H128 λ	30506.542	0.32(3)	25.6(9)	1.19E-02	-4.6(9)
30514.36	H106 ζ	30513.959	3.12(3)	28.3(9)	1.04E-01	2.1(9)
	He85 γ	30512.633				-11.0(9)
30520.52	He128 λ	30518.974	0.09(2)	21(5)	3.89E-03	-9(3)
30527.20	He106 ζ	30526.393	0.18(3)	22.1(9)	7.66E-03	-1.9(9)
	He116 θ	30525.122				-14.4(9)
30570.21	H100 ϵ	30569.184	2.50(1)	25.2(9)	9.34E-02	-4.0(9)
30582.73	He100 ϵ	30581.641	0.22(1)	17.4(9)	1.19E-02	-4.7(9)
30584.24	C100 ϵ	30584.437	0.04(1)	4.2(9)	9.95E-03	7.9(9)
30708.39	H93 δ	30707.383	3.64(2)	24.5(8)	1.40E-01	-3.8(8)
30721.18	He93 δ	30719.897	0.40(2)	20.6(8)	1.83E-02	-6.5(8)
30724.17	H111 η	30722.895	1.28(2)	26.4(8)	4.54E-02	-6.4(8)
30727.28	H124 κ	30725.950	0.43(2)	19.1(8)	2.13E-02	-7.0(8)
30733.46	H143 π	30732.592	0.08(1)	16(3)	4.81E-03	-2(1)
30736.33	He111 η	30735.414	0.07(1)	12(3)	5.41E-03	-3(1)
30750.71	H120 ι	30749.533	0.57(2)	22.8(8)	2.36E-02	-5.5(8)
30808.57	H131 μ	30807.448	0.43(2)	30(2)	1.38E-02	-4.9(7)
30899.41	H140 σ	30898.144	0.16(1)	29(3)	4.99E-03	-6(2)
30957.19	H134 ν	30955.940	0.32(2)	31(2)	9.54E-03	-6.1(9)
31187.71	H74 β	31186.685	12.09(1)	24.5(1)	4.63E-01	-3.8(1)
31200.40	He74 β	31199.394	0.91(1)	15.8(8)	5.40E-02	-3.6(8)
31202.05	C74 β	31202.246	0.035(9)	2.4(8)	1.38E-02	7.9(8)
31205.27	H127 λ	31204.090	0.09(1)	13.6(8)	6.49E-03	-5.3(8)
31224.33	H51 α	31223.316	40.99(2)	24.0(1)	1.60E+00	-3.8(1)
31237.10	He59 α	31236.039	3.56(2)	16.3(1)	2.06E-01	-4.1(1)
31238.69	C59 α	31238.895	0.29(1)	4.1(2)	6.79E-02	7.9(1)
31290.51	H115 θ	31289.572	0.72(2)	23.9(9)	2.85E-02	-3.0(3)
31371.25	H105 ζ	31370.326	1.54(2)	28.1(5)	5.16E-02	-2.8(2)
31384.03	He105 ζ	31383.109	0.10(1)	14(2)	6.48E-03	-3(1)
31454.35	H123 κ	31453.215	0.72(2)	36(2)	1.90E-02	-4.8(6)
31483.41	H99 ϵ	31482.380	2.23(1)	25.9(2)	8.08E-02	-3.8(1)
31495.05	H130 μ	31493.820	0.12(3)	20(5)	5.67E-03	-6(2)
31496.34	He99 ϵ	31495.209	0.07(2)	7(1)	9.03E-03	-4.8(5)
31504.68	H119 ι	31503.890	0.53(2)	26.4(8)	1.89E-02	-1.5(8)
31544.23	H110 η	31543.174	0.87(2)	23.7(8)	3.43E-02	-4.1(8)
31557.33	He110 η	31556.028	0.13(2)	25.7(8)	4.73E-03	-6.3(8)

Table 7 *continued*

Table 7 (continued)

f_{obs}	Species	f_{rest}	$\int T_{\text{MB}} dV$	ΔV	$T_{\text{MB}}^{\text{peak}}$	V_{LSR}
(MHz)		(MHz)	(K km s $^{-1}$)	(km s $^{-1}$)	K	km s $^{-1}$
31584.43	H84 γ	31583.399	5.46(2)	24.5(8)	2.09E-01	-3.8(8)
31597.35	He84 γ	31596.270	0.56(2)	20.7(8)	2.56E-02	-4.3(8)
31629.50	H133 ν	31628.394	0.15(1)	16(1)	9.15E-03	-4.5(6)
31636.71	H136 ξ	31635.326	0.23(1)	27(2)	7.97E-03	-7.1(1)
31699.49	H92 δ	31698.470	2.93(1)	23.9(1)	1.15E-01	-3.7(1)
31712.32	He92 δ	31711.387	0.284(2)	16.4(8)	1.62E-02	-2.8(8)
31719.17	H114 ρ	31718.352	0.069(2)	17.6(8)	3.66E-03	-1.7(8)
31936.98	He126 λ	31936.089	0.029(8)	17(9)	1.66E-03	-2(4)
31993.05	H141 π	31991.699	0.020(5)	10(4)	1.96E-03	-7(2)
32094.20	H114 θ	32093.066	0.65(1)	23.8(5)	2.58E-02	-4.6(2)
32195.24	H138 σ	32194.508	0.04(1)	19(6)	1.97E-03	-1(3)
32200.23	X II93 α	32198.461	0.097(3)	11.7(8)	7.78E-03	-10.5(8)
	H129 μ	32200.747				10.8(8)
32201.94	H129 μ	32200.747	0.091(3)	13.0(8)	6.58E-03	-5.1(8)
32204.53	H122 κ	32203.626	0.363(3)	26.3(8)	1.30E-02	-2.5(8)
32260.05	H104 ζ	32259.049	1.36(1)	25.8(3)	4.96E-02	-3.3(1)
32284.14	H118 ι	32283.136	0.42(1)	23.2(7)	1.69E-02	-3.3(3)
32312.14	H135 ξ	32310.590	0.048(9)	10(2)	4.40E-03	-8.4(9)
32321.72	H132 ν	32320.483	0.11(1)	19(2)	5.80E-03	-5.5(9)
32354.60	H143 ρ	32353.263	0.06(1)	21(3)	2.93E-03	-6(2)
32394.00	H109 η	32392.925	0.82(1)	24.0(3)	3.20E-02	-3.9(1)
32406.86	He109 η	32406.125	0.028(7)	10(3)	2.57E-03	-1(2)
32433.39	H98 ϵ	32432.322	1.86(1)	26.0(8)	6.72E-02	-3.9(8)
32446.78	He98 ϵ	32445.538	0.16(1)	14.7(8)	1.02E-02	-5.5(8)
32447.86	C98 ϵ	32448.504	0.022(6)	5.7(8)	3.57E-03	12.0(8)
32469.55	H73 β	32468.487	10.29(1)	24.5(1)	3.95E-01	-3.8(1)
32482.90	He73 β	32481.718	0.93(1)	17.8(3)	4.90E-02	-4.9(1)
32484.45	C73 β	32484.687	0.044(6)	2.9(4)	1.45E-02	8.2(1)
32633.30	H145 σ	32632.518	0.148(2)	29.5(8)	4.73E-03	-1.2(8)
32647.99	H140 π	32647.130	0.112(2)	24.8(8)	4.24E-03	-1.9(8)
32665.59	H125 λ	32664.343	0.340(2)	27.9(8)	1.14E-02	-5.4(8)
32719.60	H83 γ	32718.505	4.56(1)	24.7(1)	1.74E-01	-4.0(1)
32733.65	H91 δ	32732.677	2.73(1)	24.4(1)	1.05E-01	-2.9(1)
32747.00	He91 δ	32746.016	0.23(1)	17(1)	1.29E-02	-3.0(1)
32853.28	H58 α	32852.198	33.17(1)	24.1(1)	1.29E+00	-3.9(1)
32866.72	He58 α	32865.586	2.76(1)	15.9(1)	1.63E-01	-4.3(1)
32868.37	C58 α	32868.590	0.213(7)	3.6(1)	5.53E-02	8.0(1)
32925.43	H113 θ	32924.319	0.54(1)	22.8(7)	2.20E-02	-4.1(3)
32930.29	H128 μ	32929.005	0.22(1)	23(2)	9.05E-03	-5.7(7)
32979.09	H121 κ	32978.112	0.53(3)	26(1)	1.93E-02	-2.9(8)

Table 7 continued

Table 7 (*continued*)

f_{obs}	Species	f_{rest}	$\int T_{\text{MB}} dV$	ΔV	$T_{\text{MB}}^{\text{peak}}$	V_{LSR}
(MHz)		(MHz)	(K km s $^{-1}$)	(km s $^{-1}$)	K	km s $^{-1}$
33006.26	H134 ξ	33005.225	0.540(3)	32.6(8)	1.55E-02	-3.4(8)
	H142 ρ	33005.253				-3.1(8)
33033.93	H131 ν	33032.927	0.266(3)	26.6(8)	9.40E-03	-3.1(8)
33089.23	H117 ι	33088.307	0.385(3)	19.9(8)	1.82E-02	-2.4(8)
33182.75	H103 ζ	33181.671	1.11(1)	24.3(4)	4.30E-02	-3.8(1)
33196.09	He103 ζ	33195.192	0.11(1)	12(1)	8.95E-03	-2.1(5)
33255.85	X II92 α	33254.107	0.07(1)	18(3)	3.75E-03	-10(2)
33274.58	H108 η	33273.485	0.686(4)	23.5(8)	2.74E-02	-3.9(8)
33288.12	He108 η	33287.044	0.052(4)	12.8(8)	3.81E-03	-3.7(8)
33421.94	H97 ϵ	33420.878	1.587(8)	24.5(8)	6.08E-02	-3.6(8)
33429.83	H124 λ	33428.749	0.313(8)	16.8(8)	1.75E-02	-3.7(8)
33435.65	He97 ϵ	33434.497	0.029(8)	10.8(8)	2.54E-03	-4.3(8)
33565.53	H136 σ	33564.488	0.030(8)	7(3)	3.71E-03	-3(1)
33614.58	H148 ν	33613.495	0.13(1)	27(4)	4.59E-03	-4(2)
33680.52	H127 μ	33679.406	0.064(2)	13.3(8)	4.50E-03	-3.9(8)
33720.52	H133 ξ	33719.933	0.10(1)	15(3)	6.19E-03	1(1)
33767.63	H130 ν	33766.481	0.296(4)	35.5(8)	7.84E-03	-4.2(8)
33778.84	H120 κ	33777.647	0.330(4)	25.6(8)	1.21E-02	-4.6(8)
33785.64	H112 θ	33784.541	0.550(4)	27.9(8)	1.85E-02	-3.7(8)
33813.47	H90 δ	33812.374	2.72(4)	26.7(8)	9.59E-02	-3.7(8)
33822.61	H72 β	33821.511	9.21(4)	24.0(8)	3.61E-01	-3.8(8)
33827.34	He90 δ	33826.153	0.12(1)	16(2)	7.16E-03	-4.5(9)
33836.40	He72 β	33835.293	1.06(4)	19.7(8)	5.08E-02	-3.8(8)
33838.14	C72 β	33838.386	0.059(6)	3.2(3)	1.76E-02	8.2(2)
33909.81	H82 γ	33908.670	4.17(1)	23.5(1)	1.67E-01	-4.1(1)
33921.65	H116 ι	33920.491	0.400(6)	24.2(8)	1.55E-02	-4.2(8)
33923.61	He82 γ	33922.488	0.375(6)	16.4(8)	2.14E-02	-3.9(8)
34013.60	H138 π	34012.754	0.09(1)	25(3)	3.42E-03	-1(2)
34140.92	H102 ζ	34139.824	0.945(7)	23.7(8)	3.74E-02	-3.6(8)
34156.08	He102 ζ	34153.736	0.42(9)	32(7)	1.24E-02	-15(4)
34187.22	H106 η	34186.264	0.81(1)	25.9(6)	2.92E-02	-2.4(3)
34218.35	H123 λ	34217.208	0.10(1)	22(2)	4.34E-03	-4(1)
34279.18	H135 σ	34278.724	0.11(1)	19(2)	5.40E-03	2(1)
34358.20	X II91 α	34356.409	0.061(8)	9(1)	6.38E-03	-9.6(6)
34451.18	H96 ϵ	34450.030	1.68(8)	23.9(6)	6.62E-02	-4.0(3)
34454.60	H126 μ	34452.798	0.46(9)	39(6)	1.09E-02	-10(4)
	H132 ξ	34455.443				13(4)
34465.26	He96 ϵ	34464.068	0.12(1)	11(1)	1.01E-02	-4.4(5)
34597.51	H57 α	34596.385	34.15(2)	23.9(1)	1.34E+00	-3.8(1)
34604.36	H119 κ	34603.252	0.15(1)	20(2)	7.37E-03	-4(1)

Table 7 *continued*

Table 7 (*continued*)

f_{obs}	Species	f_{rest}	$\int T_{\text{MB}} \text{d}V$	ΔV	$T_{\text{MB}}^{\text{peak}}$	V_{LSR}
(MHz)		(MHz)	(K km s $^{-1}$)	(km s $^{-1}$)	K	km s $^{-1}$
34611.64	He57 α	34610.483	2.84(2)	15.7(7)	1.70E-01	-4.0(7)
34613.40	C57 α	34613.647	0.25(2)	3.9(7)	6.14E-02	8.2(7)
34676.37	H111 θ	34675.004	0.63(3)	22(1)	2.67E-02	-5.8(5)
34725.26	H137 π	34724.226	0.10(2)	15(3)	6.41E-03	-3(1)
34782.01	H115 ι	34780.830	0.423(4)	20.4(7)	1.94E-02	-4.2(7)
34941.26	H89 δ	34940.093	2.35(1)	23.7(7)	9.32E-02	-4.0(7)
34955.51	He89 δ	34954.331	0.19(1)	12.5(7)	1.41E-02	-4.1(7)